ABSTRACT

EFFECT OF CURRENT DENSITY RAMPING ON THE ANODIC REACTION AND MORPHOLOGY OF AEROSPACE ALUMINUM ALLOYS

by
Peter Totaro

Aluminum anodizing has been experimented with and studied over the last century because of its ability to form uniform, well ordered cellular coatings on aluminum alloys. Anodizing aerospace alloys has been problematic, due to the alloying elements used to add strength and resistance to stress cracking corrosion. These intermetallic compounds, i.e., copper and zinc, promote oxygen evolution and stress as they accumulate in and on the surface of the forming aluminum oxide. These inclusions lead to increased electrical resistance that forms porous and flawed coating, which can lead to industrial and field failures. The amount of voltage placed on the electrochemical system is shown to alter the current density and has positive and negative effects on coating growth and quality. The magnitude of this variable has been manipulated to control the amount of coating formed and enhance film properties. Changing current density can reduce the amount of overall voltage on the system and reduce the amount of intermetallic contamination in the coating.

In this work, the investigation of the influence of time variation of current density is applied to AA7075-T6 and AA2024-T3 in the course of anodization, on the ramping stage and overall process. These two alloys are chosen because they represent the most used alloys in the aerospace industry and exhibit distinct and unique electrochemical behavior. The experimental work includes monitoring process kinetics and rates of formation of anodic aluminum oxides. Changes in pore structure of anodic coatings, including size, shape and distribution are observed under high scanning electron magnification. Utilizing energy dispersive X-ray spectroscopy and X-ray Diffraction, changes in the alloy intermetallic composition and microstructure are analyzed.

Lastly, surface characteristic experiments which measure anodic aluminum oxide compactness, hardness, thickness, and corrosion resistance are conducted.

Utilizing low voltage at the onset of anodizing and gradually raising current density allows for a more aluminum rich oxide and allows time for nonaluminum ions to leave the forming coating or become oxidized. It is expected that using low voltages during the ramp phase of the process will lead to changes in industrial processing as it allows for larger loads to be processed faster with less defective coating.

EFFECT OF CURRENT DENSITY RAMPING ON THE ANODIC REACTION AND MORPHOLOGY OF AEROSPACE ALUMINUM ALLOYS

by
Peter Totaro

A Dissertation
Submitted to the Faculty of
New Jersey Institute of Technology
in Partial Fulfillment of the Requirements for the Degree of
Doctor of Philosophy in Chemical Engineering

Otto H. York Department of
Chemical and Materials Engineering

August 2022

APPROVAL PAGE

EFFECT OF CURRENT DENSITY RAMPING ON THE ANODIC REACTION AND MORPHOLOGY OF AEROSPACE ALUMINUM ALLOYS

Peter Totaro

Dr. Boris Khusid, Dissertation Advisor Professor of Chemical and Materials Engineering, NJIT	Date
Dr. Zafar Iqbal, Committee Member Professor Emeritus of Chemistry and Environmental Science, NJIT	Date
Dr. Reginald P.T. Tomkins, Committee Member Professor Emeritus of Chemical and Materials Engineering, NJIT	Date
Dr. Kamalesh K. Sirkar, Committee Member Distinguished Professor of Chemical and Materials Engineering, NJIT	Date
Dr. David C. Venerus, Committee Member Professor of Chemical and Materials Engineering, NJIT	Date
Dr. Dibakar Datta, Committee Member Assistant Professor of Mechanical & Industrial Engineering, NJIT	Date

BIOGRAPHICAL SKETCH

Author: Peter Totaro Jr.

Degree: Doctor of Philosophy

Date: August 2022

Undergraduate and Graduate Education:

- Doctor of Philosophy in Chemical Engineering,
  New Jersey Institute of Technology, Newark, NJ, 2022

- Master of Science in Chemical Engineering,
  New Jersey Institute of Technology, Newark, NJ, 2016

- Bachelor of Science in Biochemistry and Molecular Cell Biology,
  The Richard Stockton College of New Jersey, Galloway Township, NJ, 2010

Major: Chemical Engineering

Presentations and Publications:

P. Totaro, & B. Khusid, Multistep anodization of 7075 – T6 aluminum alloy, Surf. Coat. Technol. *421* (2021) 127407–.https://doi.org/10.1016/j.surfcoat.2021.127407

P. Totaro & B. Khusid, Effect of Current Density Ramping on the Growth Rate and Structure of AA2024-T3. Materials *15* (2022) 3258. https://doi.org/10.3390/ma15093258

Presentations:

P. Totaro, Engineering Considerations for Difficult Alloy Anodizing, presented at the 18th Technical Symposium of the International Hard Anodizing Association, Copenhagen, Denmark, September 2022 (Presentation & Paper).

P. Totaro, New Aluminum Extrusion Technologies and Their Challenges for Extruders and Anodizers: A Panel Q & A, AAC (Aluminum Anodizers Council) Fall Conference & Exposition, Nashville, Tennessee, September 2021 (Speaker Q&A).

P. Totaro, Deoxidizing Aluminum and its Effectiveness as a Pre-Treatment for Anodizing Aluminum Alloys, presented at the AAC (Aluminum Anodizers Council) Fall Conference & Exposition, Denver, Colorado, (Presentation & Paper).

I dedicate my dissertation work to my family, employer, and many friends. A special feeling of gratitude to my grandparents, who always challenged me and made me utilize my talents to maximize my potential. They are the reason I am the man I am today. The greatest dedication to my wife Megan, without her constant motivation and enthusiasm, this PhD would not be possible.

ACKNOWLEDGEMENT

I would like to express my most genuine appreciation and gratitude to my Dissertation Advisor, Dr. Boris Khusid, for his invaluable guidance and great support throughout every stage of my graduate studies.

It has been a great pleasure to work and interact with the committee members: Dr. Zafar Iqbal, Dr. Reginald P.T. Tomkins, Dr. Kamalesh K. Sirkar, Dr. David C. Venerus, and Dr. Dibakar Datta. I appreciate all the guidance and time you put forth in aiding my studies.

It has been a great pleasure to work and interact with all the staff and students in New Jersey Institute of Technology's Chemical and Materials Department. I would like to express my gratitude to Dr. Xueyan Zhang and Dr. Jeong S. Shim. Without their training and guidance, the materials characterization portion of the study would not be possible. I would like to express my gratitude to Dr. Mirko Schoenitz, who also aided my studies with valuable data. I would like to express my gratitude to Dr. Sagnik Basuray and Zhenglong Li for help in conducting EIS measurements and interpretation of data.

I would like to also express my sincerest thanks to Jeffrey Almeyda. His mentorship and support throughout my career made all of these achievements possible. I would like to thank the staff at Aerotech Processing Solutions. Without their support, use of their equipment, and most importantly, their confidence, these studies would not be possible.

I would like to express my dearest gratitude to my parents and grandparents for their love and encouragement, and for supporting me in many ways throughout my study. Finally, a very special thanks is given to my wife, Megan Totaro, my two beautiful daughters, Juliette and Sienna Totaro, and my son, Peter Totaro III, who have been with me every step of the way, with their love and support.

TABLE OF CONTENTS

TABLE OF CONTENTS
(Continued)

Chapter **Page**

LIST OF TABLES

LIST OF TABLES
(Continued)

LIST OF TABLES
(Continued)

LIST OF FIGURES

LIST OF FIGURES
(Continued)

LIST OF FIGURES
(Continued)

LIST OF FIGURES
(Continued)

LIST OF FIGURES
(Continued)

LIST OF FIGURES
(Continued)

Figure **Page**

LIST OF FIGURES
(Continued)

Figure **Page**

LIST OF FIGURES
(Continued)

Figure **Page**

CHAPTER 1

ANODIZING ALUMINUM ALLOYS

1.1 Introduction into Anodizing Aluminum Alloys

Aluminum and its alloys have a great tendency to form an oxide layer on its surface when exposed to a favorable atmosphere. When exposed to air at room temperature, or any other gas containing oxygen, pure aluminum self-passivates by forming a surface layer of amorphous aluminum oxide 2 to 3 nm thick [1]. Although this layer has a minimal thickness, it can cause a natural increase in corrosion resistance of the aluminum alloy [2]. Pure aluminum, 1000 series or >99.0% purity, does not have enough tensile strength, 90 MPa, to withstand the static and dynamic movements needed for the aerospace industry [3]. The alloy is coupled with copper or zinc to create a new series of aluminum (i.e., 7000 series) with higher tensile strength, 572 MPa [3]. However, aluminum alloys containing copper and other alloying elements exhibit low corrosion resistance and are susceptible to localized corrosion [4-6]. Thus, these alloys are anodized to improve their corrosion resistance [7].

Anodization is an electrochemical process that is performed to form a protective oxide layer on the surface of a metal. Thicknesses can range from 1 - 130 μm, depending on the type of anodizing. The purpose of the non-conductive layer is to give enhanced corrosion and wear resistance to aluminum. Anodizing can be described as forced oxidation of the anode.

Table 1.1 Bath Associated Variables in the Anodizing Process

Anodizing Type	Electrolyte Composition (%wt)	Temperature (°C)	Voltage (V)	Current Density (A/m^2)	Time (Minutes)	Thickness (μm)
I	Chromic Acid 5%	32 to 38	22, 40	22-32	30 to 60	1.2 to 2.2
II	Sulfuric Acid 8-14%	18 to 24	16 to 18	108-129	30 to 50	7.5 to 25.4
III	Sulfuric + Organic Acid 15-20% Total	(-4) to 4	10 to 70	215-431	30 to 120	25 to 127

Note: Each type of processing has parameters which give coating properties unique to the anodizing type.

During a closed-circuit anodizing reaction, the current flows through the anode and into the electrolyte, which the infinite feed of reactant is the aluminum anode. The occurring redox reaction consumes the bare aluminum alloy and transforms it into a ceramic aluminum oxide. This oxide film will grow from the substrate outward as thickness increases. The result of anodic oxidation depends on several factors, particularly the type, concentration, and temperature of the electrolyte and the electrolytic operating conditions such as voltage and agitation [8]. Under the applied electric field, the Al^{+3} ions escape from the metal lattice and transport to anodic oxide layers throughout the metal/oxide interface and then continue to move outwards [9]. Meanwhile, the O_2^- that formed at the position of electrolyte/oxide interface is moving inwards with the opposite direction, until they meet at the interface to form aluminum oxide, Al_2O_3 [9]. The natural reaction of forming aluminum oxide is an equilibrium process; however, the aluminum oxide formed during anodizing is not. It is not an equilibrium process because the energy source needed to drive the chemical reaction comes externally. The reactants in the reaction, aluminum Al^{+3} ions, migrate to the electrolyte/metallic interface by way of concentration gradients and current transforming aluminum into aluminum oxide in the presence of water [9].

The anodizing process can only begin once the open circuit is closed. The circuit is closed by suspending the anode into the electrolyte, which in contact by wires to the external power source. Anodic oxide film growth is only possible when immersed in an electrolyte. When immersed, applied current flows from the power source to the anode. At the anode, current flows through the electrolyte to the cathode and back to the power source. The cathodes also have their bussing or wires attached to the power source. The applied current drives the flow of electrons through the substrate and produces diffusion by way of electrochemical transport of aluminum ions toward the interface with the electrolyte, where the oxide is produced [10].

When aluminum polarizes as the anode, the basic oxidation reaction that occurs at the interface with the electrolyte can be summarized as follows [11]:

$$2Al + 3H_2O \rightarrow Al_2O_3 + 6H^+ + 6e^- \quad (1.1)$$

AAO is an amorphous solid composed of hydrated aluminum oxide present as $Al_2O_3 \cdot H_2O$ and $Al(OH)_3$. Being an amorphous structure means that as formed, AAO does not have a crystalline structure, but it does have a chemical structure [11].

For anodizing in sulfuric acid electrolyte, the reaction proceeds as follows:

$$4Al + 6(H_2SO_4) \rightarrow 2(Al_2O_3) + 6(SO_3) + 3(H_2)_g + 6H^+ + 6e^- \quad (1.2)$$

For the oxidation of aluminum to take place, the sulfuric acid electrolyte needs to be broken down at the interface. The chemical absorption of water, outgassing of hydrogen gas, and mild uptake of sulfite ions, all take place simultaneously while the film begins to grow [11]. Because the primary reaction produces exclusively aluminum oxide, adsorbate from the electrolyte counterion becomes

part of the oxide, which is on contact with the electrolyte and is significant enough to be detected [11]. Porous aluminum oxides grow in acidic environments with typical electrolytes of sulfuric, oxalic, and chromic acids. Porous aluminum oxides consist of cellular pores that grow deep into the metal in the shape of a tube [12]. The dimensions of each cell are uniform. The wall thickness and pore diameter are proportional to the anodizing process parameter of applied current density and potential response, or conversely, the applied "formation" voltage and the current response [11]. The structure exhibits minimal x-ray diffraction contrast and is therefore designated amorphous but has been shown to exhibit short-range crystalline order [13]. The anodic oxide structure is comprised of aluminum and oxygen ions coordinated as AlO4 – tetrahedra, which form a network of self-assembled, highly ordered nanoscale columns [14].

As anodic coating grows, the resistance becomes higher. The resistance increases because aluminum oxide is non-conductive. Higher quality films are achievable when minimizing resistances in the reaction. Cathodic and power supply resistances can be minimized by having compatible materials and tight, clean contact points. Cathode materials that do not dissolve into the tank during the reaction are optimal. Any corrosion or faulty contacts in an area that transfers current will increase resistance and generate heat. This heat generation at the anode can result in powdery coatings and defective hardware.

The electrolyte, by far the most significant conductor in the anodizing circuit, may be comprised of a variety of protonic acids, as a single or mixed acid electrolyte, and may contain additives to chemically aid in reducing electrolyte resistance and interfacial heating of the anodizing reaction [10]. Solute anions within the electrolyte carry the current from the anode to the cathode and, depending on the temperature of the electrolyte, can aid in thermally conducting heat resistance away from the anode surface during oxidation [10]. Acidic electrolytes like sulfuric acid, become more conductive at higher concentrations. Increasing the conductivity of the solution

causes the resistance of the solution to decrease and the circuit voltage, or potential, as a response to a specific current density to decrease [10].

In aluminum anodizing, it is often thought that the larger amount of fixed potential applied to the system will result in thicker coatings that occur faster. This is true for a period, until the coating thickness grows to a level rendering that potential insignificant for film growth, due to the increased resistance. Oxidation potential is a characteristic of the anode, and if the potential response of the anodizing process exceeds the characteristic potential of the aluminum, oxidation occurs if current flows [10]. Conversely, if the potential response is below the characteristic potential of the formed coating, oxidation will cease.

1.2 Aerospace Aluminum Alloys

2000 and 7000 series alloys are of interest for the aerospace industry due to their low density, high strength to weight ratio, excellent fatigue properties [1,15-17] and their resistance to stress cracking corrosion [17-20]. Aluminum-copper (2000 series) alloys are the primary alloys used in airframe structural applications where the main design criterion is damage tolerance [21]. The 2024-T3 alloy has been one of the most widely used alloys in fuselage construction, with having moderate yield strength, excellent resistance to fatigue crack, and good toughness [21]. Microstructural effects on fatigue properties have been investigated extensively over time, with inclusions of Cu and Mg to increase strength; however, they have adverse effects on crack propagation and corrosion resistance [21].

The 7000 series of aluminum alloys show higher strength when compared to other classes of aluminum alloys, and they're machined into upper wing skins, stringers, and horizontal/vertical stabilizers [21]. The popularity of 7075-T6 heat-treated alloys is due to its high strength-to-weight ratio, machinability, and relatively low cost [21]. However, due to its composition, Cu, Fe, Mg,

and Zn, these alloys are susceptible to corrosion. Corrosion reduces the life of aircraft structures considerably.

2000 and 7000 series aluminum alloys undergo precipitation hardening, **Figure 1.1**, as a strengthening mechanism, as alloying elements form clusters called S-phase precipitates having the composition of Al_2CuMg and other conglomerations [22,23]. In these alloys, the presence of precipitated intermetallic phases induces localized micro-galvanic couplings since their electrochemical behavior differs significantly from the surrounding aluminum-rich matrix [21,24-27]. These galvanic reactions can happen before, during, or after electrochemical processing, all with detrimental effects. Galvanic reactions between the intermetallics and the matrix cause selective corrosion at the interface. The formation of new compounds, or defects at the interface, creates fissures and pathways for corrosion to enter inside the aluminum [28]. These secondary and tertiary reactions are detrimental to the anodic oxidation of aluminum.

These areas around the intermetallic groups cause semi-coherent phases, which ultimately cause dislocations and strain in the aluminum matrix [29].

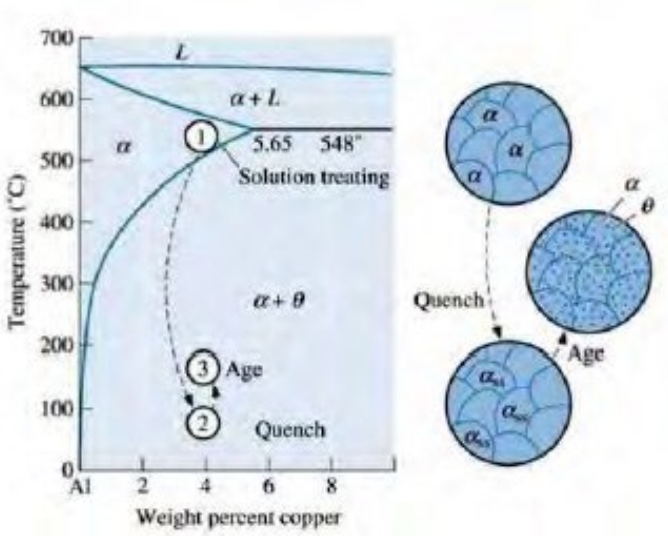

Figure 1.1 Three steps in the age-hardening heat treatment for the Al-Cu alloy. *Source: [22].*

For example, the copper-rich precipitate zone along the grain boundary is more noble/cathodic, which creates a difference of potential between the aluminum matrix and the formed precipitates, which leads to intergranular corrosion [30], see **Figure 1.2**. However, even though precipitation hardening is beneficial to strengthening the alloy, the formation of precipitates is determinantal to anodizing.

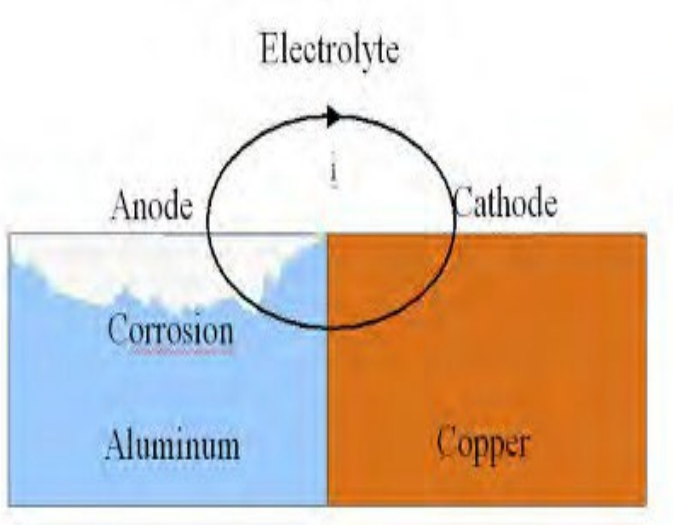

Figure 1.2 Example of galvanic corrosion between a more noble element in a conductive environment.
Source: [31].

The inclusion of particles trapped in the anodized film has a significant effect on the formation of corrosion pits, which accelerates fatigue crack initiation [32,33], see **Figure 1.3**. The mechanism behind the corrosion process are oxidation and reduction reactions. These reactions can happen between multiple elements at multiple locations on the surface. For these reactions to occur, the surface must be metallic, the standard potential needs to be significant, and there needs to be moisture (present or adsorbed) [11]. The moisture allows electrons to flow through metal from anodic to cathodic regions [11].

The introduction of intermetallics significantly impacts the corrosion resistance of the material by forming electrochemical cells within the aluminum matrix, in which, almost of the

alloying elements are more noble than aluminum [11,35-37]. Phases on the surface of aluminum substrate tend to be cathodically protected in the redox reaction while the aluminum matrix has a net anodic reaction, which provokes the dissolution of the aluminum matrix [35]. The presence of copper and zinc greatly reduce the anodic efficiency, thereby leading to a higher resistance. This can also lead to overheating or runaway dissolution of the aluminum matrix.

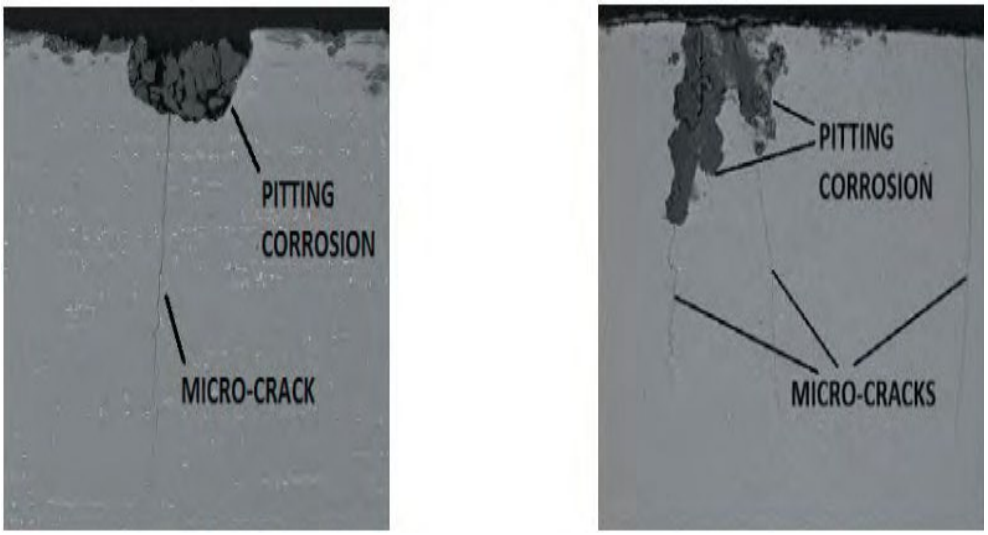

Figure 1.3: Examples of pitting corrosion. The visible cracks, located at the bottom of the corrosion pit, can lead to the final fracture of the material.
Source: [34].

The presence of intermetallic particles accelerates corrosion of 2000 and 7000 series alloys, see **Figure 1.4**. Particles containing Al, Cu, Fe, and Mn act as cathodes and promote matrix dissolution at their periphery [38-41], while particles containing Al, Cu, and Mg, (i.e., Al_2CuMg, S-phase) show anodic behavior and dissolve with preferential dealloying of Mg and Al [39,42-44]. The S-phase is a more complicated reaction. Initially, the matrix is anodic and then being transformed to a net cathode after dealloying or leaching out of magnesium and aluminum, resulting in the enrichment of a spongy-like copper remnant [45-46]. The cathodic properties of

the copper-rich phase led to dissolution and depletion of the matrix surrounding the elementary particle [45-46].

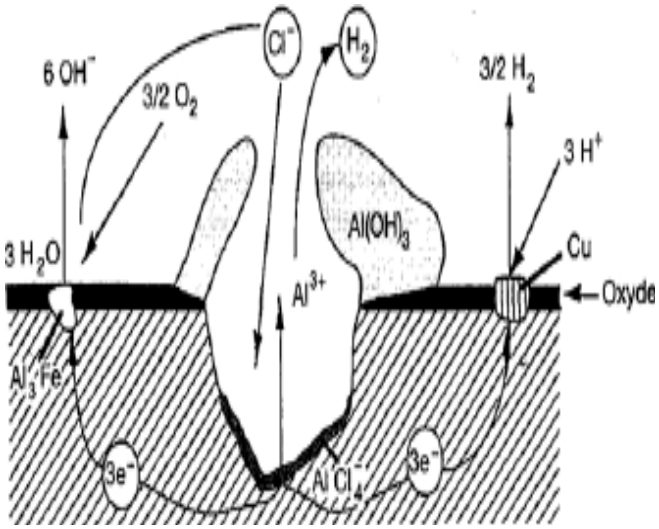

Figure 1.4 Simple illustration of mechanism of pitting corrosion of aluminum.
Source: [47].

Copper tends to precipitate at grain boundaries, making the metal very susceptible to stress cracking corrosion [48-50]. This "attacking" of the grain boundary can be attributed to the higher stored energy at the grain boundary between two grains [46]. Trenching of the matrix surrounding intermetallic particles is galvanic corrosion between the matrix and the particle [46].

Aluminum alloys have a naturally active thin oxide layer on the surface, i.e., protecting from pitting initiation. If this oxide layer is damaged, aluminum alloy itself recovers and generates this passive film. In 2000 and 7000 alloys, this film breaks down, allowing pitting and crevice corrosion of the underlying substrate [11]. An increase in the reinforcement phase further leads in discontinuities in the film, increasing the number of sites for corrosion initiation and burrowing [51].

Pitting corrosion is a localized accelerated dissolution of metal that breakdown the passive protective film on the surface [51]. Due to various methods of corrosion resistance breakdown, effective surface modification methods are needed to enhance corrosion resistance. Of all known methods, anodizing has the best potential to protect 2000 and 7000 series alloys from corrosion [51].

1.3 Problems with Anodizing Aerospace Aluminum Alloys

Deformable alloys, which are known as 2000 and 7000 series alloys, have specific applications in aerospace, military, and structural industries due to their superior mechanical properties and low density [30,52-53]. Depending on the application needed in aerospace, the anodizing layer will be subjected to multiple environments and will have to pass rigorous testing. **Table 1.2** shows a brief outline of the performance criteria set by the aerospace industry for 2000 and 7000 series alloys.

Table 1.2 Performance Criteria for Anodized Aerospace Alloys 2024-T3 & 7075-T6

Alloy Type	Hardness Bare (MPa)	Abrasion Resistance (Mg loss)	Coefficient of Friction (μ)	Surface Roughness (μm)	Corrosion Resistance (Hours)
2024-T3	400-430	35 max	0.4 max	0.420 - 0.575	336 min
7075-T6	500	15 max	0.35 max	0.420 - 0.575	336 min

Unfortunately, alloying elements and precipitates which contribute to age hardening in heat treatable aluminum alloys [1], introduce critical issues during anodization making the obtainment of a hard, compact, low-defected, and well-adherent oxide difficult [2-6]. Some of the defects associated with the above are burning, which is a localized spike of current density resulting

in uneven growth of oxide layer and runaway dissolution, whereas temperatures in these areas are extraordinarily higher than the surrounding system [7,9]. Correlations between the percentage of intermetallic elements alloyed into the aluminum and the difficultly the alloy is to anodize is known [54]. Performance characteristics such as surface roughness or wear resistance are compromised to give a better property such as corrosion resistance. The composition between AA2024 – T3 is dramatically different than AA7075-T6 and it is well established that a difference in a composition between these alloys drastically changes the alloy electrochemical behavior and therefore the formation of anodic layers [11,55-57]. This change in anodizing behavior requires unique methods for each alloy for successful processing.

There are several mismatches in the electrochemical reaction, which lead to intermetallic contamination and reduce the quality of the coating. The structure of the forming oxide and the thermodynamic differences between metals and oxides, in which diffusion occurs faster in metals, complicate the reaction and process effectiveness [56].

The short-range order throughout the aluminum oxide layer will limit the diffusion of alloy ions, whereas, at the interface, the interstitial volume is larger, allowing the ions to migrate through [56]. The ionic radii specific to the primary alloying elements, specifically zinc, copper, and magnesium are 88, 87 and 86 pm respectively: 22-23% greater than the aluminum ion [58]. During the anodizing reaction, the diffusivity of the ions increases. However, when they reach the free surface at which oxidation takes place, diffusivity for all atoms is decreased with aluminum continuing as the fastest due to its size compared with the rest of the ions, 67.5 pm [56]. As these ions accumulate at the interface, they inhibit oxidation of the underlying aluminum and can oxidize themselves [56]. As the reaction proceeds, two reactions occur: first, areas around accumulated nonaluminum ions will continue to be anodized, while the accumulation of nonaluminum ions can similarly oxidize, or create localized stress risers across the interface [56]. Second, would be if the

ions accumulate at the local interface and oxidation of the adjacent aluminum is inhibited, which forms a discontinuity with the substrate [56]. The anodic oxide will replicate exactly to any imperfection on the substrate or void during coating formation [56]. These voids and accumulation areas of intermetallic ions are where the burning of the anodic oxide begins to take place. For 7075-T6 zinc continues to migrate as the reaction proceeds through the defect area with some resistance heating, leaving a hole in the anodic aluminum oxide, or at the interface of the substrate [56]. This causes stresses in the formed coating and leads to delamination and other crazing like rejects. These types of defects are unique to 7000 series alloys.

For 2024 – T3, copper also migrates when excited by current, although does not only pile at the interface, but throughout the entirety of the film and coating surface. Many authors consider to the presence of copper enhances parasitic local anodic reactions that reduce the faradaic efficiency of anodization and facilitates the growth of a highly flawed porous oxide layer [17, 59-61]. This causes an increase in the electrical resistivity of the film immediately above the copper-rich areas [62]. Current oscillations during the first stages of oxidation are a hint of oxygen evolution taking place [62]. Once sufficient pressure is reached, the oxygen bubbles burst and rupture the anodic oxide. The electrolyte can then reach the metal underneath the oxide film, which is subsequently anodized. This leads to the filling of the voids by the formation of a new anodic oxide, but with an altered local morphology [62]. Since the oxygen evolution reaction consumes part of the current but does not contribute to the oxide film formation, the anodizing efficiency of copper-rich aluminum alloys decreases [17]. The rapid migration of copper compared to Al^{3+} cations would populate the oxide film of copper compared with the alloy composition [59] and contributes as a gas forming species in the anodic reaction.

In summary, the major difficulty in anodizing these alloys is related the presence several intermetallic precipitates. However, each precipitate poses a different anodic oxidation challenge

and can cause the reaction to go awry. This presents the challenge of understanding how each wrought aluminum alloy behaves in the anodic reaction separately from one another to drastically reduce the problematic nature of processing these alloys. The presence of intermetallic compounds facilitates the appearance of defects which differ from alloy to alloy and dramatically change the electrochemical behavior of AA7075 – T6 and AA2024 – T3. As the electrochemical behaviors change, each alloy requires different anodizing regimes for successful processing [54,55,57,63-65].

1.4 Research Objectives and Stepped Ramp Anodizing

1.4.1 Stepped ramp anodizing

Different types of processes are used depending on the type of coating performance required. Generalized specifications such as Mil-PRF-8625 and Engineering handbooks such as ASM, will give only overviews on the requirements the of coating performance. Most aerospace OEM's do not make proprietary data public due to ITAR regulations and other business purposes. Almost all OEMs use Mil-PRF-8625 as the genesis for their standards and of coating performance requirements. The specification Mil-PRF-8625 gives generalized information on what the typical requirements and acceptable coating should be, however do not specify procedures on how to obtain these performance standards.

Most anodizing professionals either use industry literature or hire industry consultants to help meet these requirements Validation processes require monthly characterization testing of AA2024 and AA7075 to be certified to anodize. Since the composition of the alloys makes successful anodization problematic, passing the validation process is difficult. For example, to pass abrasion resistance of 7000 series low copper alloys, i.e., AA7075-T6, the maximum amount of coating loss is 15 mg per 10,000 revolutions on the taber abraser. For context, there are less

than 30 companies in the USA (40 worldwide) that can meet this Boeing standard for 7000 series aluminum [66,67]. One of the reasons is that most specifications and standards do not give insight on how to process, but only performance criteria. This issue is becoming more and more prevalent in today's aerospace industry. OEMs are having a hard time meeting assembly completion dates and finding reliable suppliers who can consistently meet the rigorous quality standards.

Type II coatings specialize in corrosion resistance. Typical processing of Type II would be a ramp stage of 30 seconds to 2 minutes at a potential of 10 V, and then finishing the process at 16-18 V. In fact, in the literature, gives some insight on how to process [68], say that ramping is not needed at all, and a constant voltage of 16-20 V is sufficient. Ramps are typically found in Type III anodizing, where it is important to build enough pore structure and gradually increase current density into the process so burning (powdering) of films does not occur. Typical ramps in Type II anodizing do not employ a series of steps in the ramp, usually one step is used and then adjusted to the final current density. A step can be defined as a low-level current density stage applied as a gradual increase or "steppingstone" into the final current density.

Ramping or the ramp phase of the process, is a period within the first 5 to 10 minutes of the process where 1-5 V or 11-54 A/m^2 increments are added to the system to promote or enhance the growth of anodic film. A depiction of a ramp is in **Figure 1.5**. It is during that period where a thin layer of anodic oxide is formed, and the initial pore formation begins. A stepped ramp approach aims for application of lower amounts of current to aid in the reduction in heat and dissolution. A step ramp approach has not been thoroughly explored in literature or in industry, and it can be theorized that ramps with a longer step at low current densities (32 - 129 A/m^2) during ramping will be more beneficial.

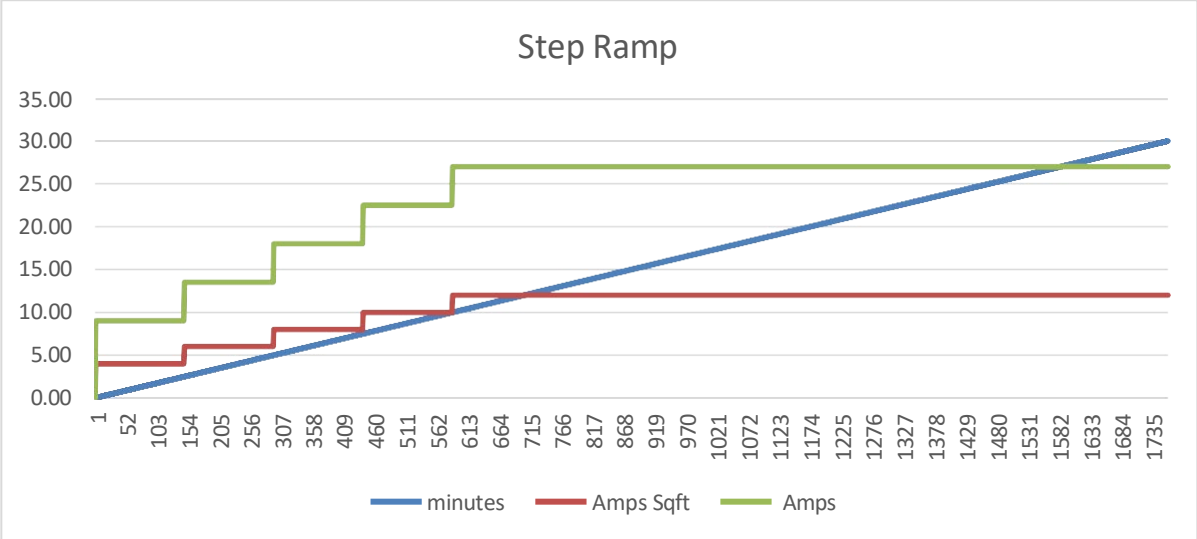

Figure 1.5 Example of a stepped ramp process

The total amount of potential will be less at the onset of the reaction (<5 V), which will slow coating formation, dissolution and heat buildup. The reason why multiple steps were chosen compared to one step, is because when there are positive changes of potential, the equilibrium of the reaction is surpassed and becomes more efficient. This is beneficial because adjustments in current allow for better heat dissipation and oxygen removal from the surface [17,18]. This will also allow the interfacial heat to dissipate, and allow for accumulated non-aluminum ions, especially zinc, to migrate forward. This is because the AAO only allows for current to flow in the direction of the bias and that momentum will continue even when the current is briefly reduced or enhanced [56].

By using multiple steps, 4x or more, within the ramping portion of the process, higher current densities can be used at the end of the process without the risk of burning and other coating deformations. Studies have shown that higher potential values and current densities have been used to increase pore diameter and interpore spacing [10,69], and lower amounts of potential can mitigate burning and powdery films [70,71]. Manipulation of potential and current density by varying

potential is used in some applications like creating nanopores and carbon nanotubes or coating for abrasion resistance. Studies on varying current throughout the process and specifically at the onset of the process are limited.

1.4.2 Research objectives

The novelty of this work would be to use nontraditional methods of anodizing by varying the voltage and current density during the ramping stage of the process. By using multiple steps, 4x or more, within the ramping portion of the process, higher current densities can be used at the end of the process without the risk of burning and other coating deformations. Manipulation of potential and current density is used in some applications like creating nanopores and carbon nanotubes or a coating for abrasion resistance. Studies on varying current throughout the process and specifically at the onset of the process are limited. Most studies vary voltage throughout the entire process or anodize in specialty additives which are not allowed in the aerospace industry for Type II anodizing.

The main goal of the proposed research is to investigate the influence of variation of current density applied to AA7075-T6 and AA2024-T3 during anodization, on the ramping stage and overall process. These two alloys were chosen because they represent the most used alloys in the aerospace industry [72,73] and are also some of the most difficult alloys to anodize [74]. These two alloys are the two representative alloys used for all characterization testing in the aerospace industry. They also exhibit vast differences in electrochemical behavior which suggests multiple anodizing methods are needed.

Experiments are carried out on AA7075-T6 and AA2024-T3 in a controlled sulfuric acid electrolyte anodizing bath. The main research results are presented in two papers, each with their

own chapter: **Chapter 3, Multistep Anodization of 7075 – T6 Aluminum Alloy,** published in *Surface and Coatings Technology***,** and **Chapter 4, Effect of Current Density Ramping on the Growth Rate and Structure of AA2024-T3**, published in *Materials.* These studies give results on the impact of changing current density during the ramping stage of the process on morphology and surface characteristics. Corrosion resistance, wear resistance, microhardness, XRD, SEM/EDS on morphology and composition, dissolution resistance, pore size and distribution and electrical processing parameters were all analyzed during this study. The presented results clearly demonstrate that starting anodizing processes at a low voltage and then slowly ramping current density will form more aluminum rich coatings with enhanced properties in a shorter period. It would be recommended that applications needing higher wear resistance and thicker coatings for dielectric properties, use AA7075-T6. Multistep anodization processes were successful in reducing the processing time, energy consumed and providing defect free coatings which shows large scale industrial anodization of AA2024-T3 and AA7075-T6 can be obtained utilizing these methods.

1.5 Summary and Future Work

Anodizing is used to improve corrosion and wear resistance of aluminum alloys because the natural layer formed does not give adequate application properties. Due to complex intermetallic phases in the matrix, AA7075-T6 & AA2024-T3 do not anodize well [17,18,73,75]. The major difficulty in anodizing these alloys is related to the compositional heterogeneity by the presence of intermetallic compounds. The presence of intermetallic compounds facilitates the appearance of defects during anodization by generating a spatially non-uniform distribution of electric current in the alloy matrix. It leads to uneven growth of anodic oxide and surface burning, especially when higher voltages and current densities are applied [1,11,75-77]. The burning of film is caused by a runaway dissolution at the oxide surface that occurs when the current density is locally spiked.

Spikes in the current density, loose powdery coating, insufficient micro adhesion, and evolution of oxygen gas bubbles at the oxide surface are all common issues that decrease the anodization efficiency and are exacerbated by anodizing at higher voltages [1,11,17,18,52,54,60,61,75-79].

Several recent studies demonstrated that the use of "stepwise anodization," a process by raising the magnitude of an applied voltage or an electric current during anodization [18,80] can improve surface properties of heat-treatable aluminum alloys, but the outcome was found to strongly depend on various factors, such as the alloy composition, bath type and temperature [81,82]. In stepwise anodizing, the voltage is incrementally increased overtime until the final current or voltage is reached, thereby allowing the use of a lower initial voltage to start the process. It is believed that the use of lower initial voltages and current densities allows for a more aluminum rich coating to form and for nonaluminum ions to dissolve in the electrolyte when an electric current is applied [83]. This allows for formation of more dense anodic coating which has higher performance characteristics and allows for a more efficient process.

The work aimed at refining and developing new processes for anodizing these difficult alloys is expected to continue and focus on how to further manipulate the current density to get a desired application. It is further expected to eventually have "designer processes" in which certain processes will designed to proliferate a certain characteristic such as abrasion resistance.

CHAPTER 2

ELECTROCHEMICAL CELL SET-UP, PROCESS AND CHARACTERIZATION TESTING

2.1 Electrochemical Tank Set-Up

Anodizing treatment was performed at a lab at Aerotech Processing Solutions, LLC. in Paterson, New Jersey. Aerotech is a special processing facility which specializes in providing corrosion resistant coatings on various metallic substrates. Schematics of the anodizing process tank can be found in **Figure 2.1** through **Figure 2.3**. **Figure 2.1** represents a front view of the processing tank. **Figure 2.2** represents the computer module. **Figure 2.3** represents a top view of an empty processing tank.

As shown in **Figure 2.1** the electrolytic tank is a rectangular polyvinylchloride chemical resistant tank (Almax Industries, New York). Tank volume is 511 L, and the dimensions are 0.61 x 0.91 x 0.91 m. All bussing, flight bar, and electrical connections on the outside of the tank are made of 5.1 x 1.27 cm 99.9% purity copper (Tilton Rack Corp, New Jersey). The cathodes and spline/hook, which submerges the anode into the electrolyte, are made of two 8.8 x 2.75 x 40.0 cm 6063 aluminum extruded bar (Tilton Rack Corp, New Jersey).

The cathode to anode ratio of the experiments will be a 1:1 ratio based off square meters. There is one cathode on each side of the tank for even distribution of current. The power supply used is DC power supply (American Plating Power, LLC, Fort Myers, Florida). This device can supply 18 V of direct current and up to 1000 A. With this power supply, anodizing rates up to 857 A/m^2 could be achieved.

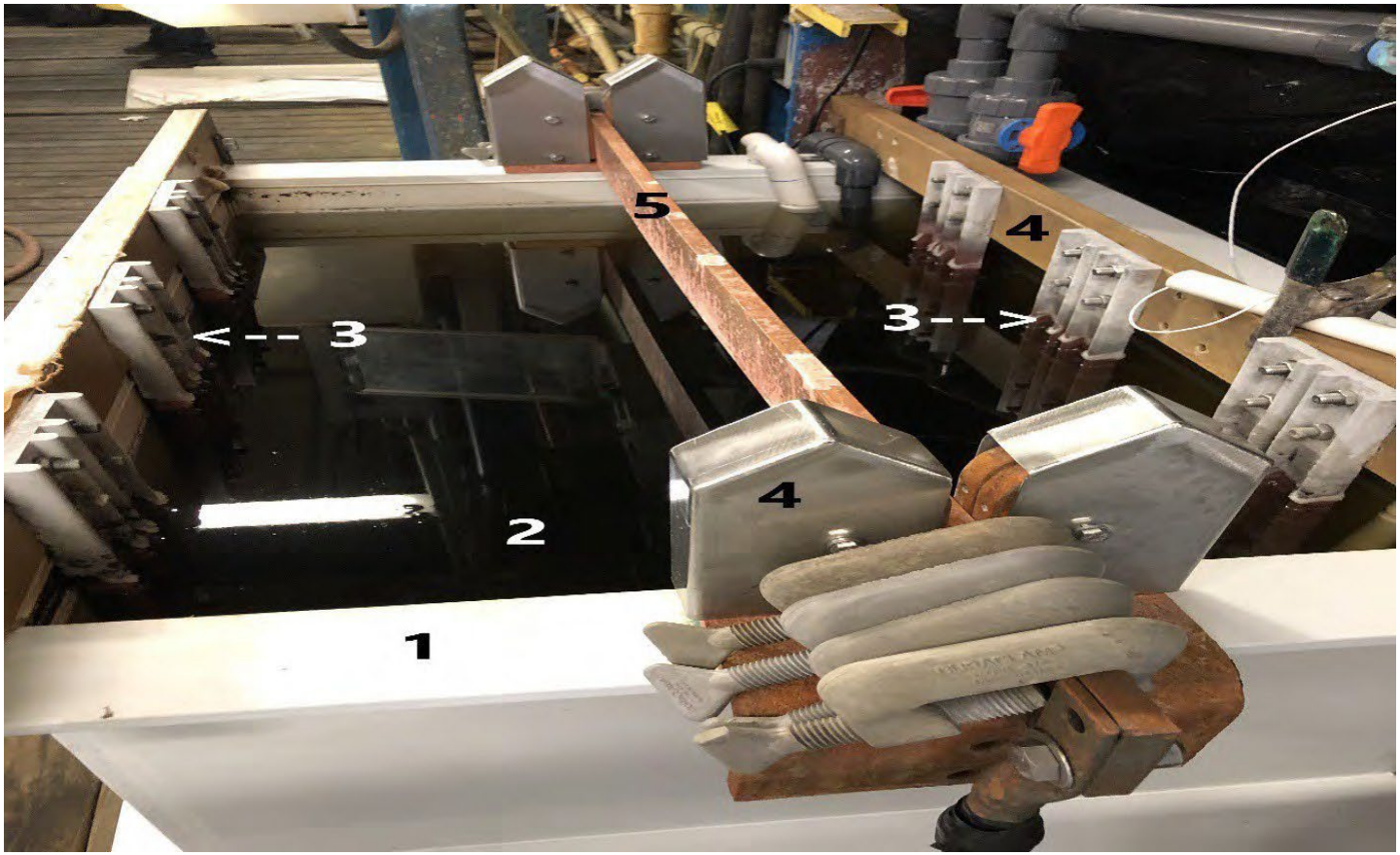

Figure 2.1 Anodizing tank overview. (1) 5.1 cm thick by 0.61 m long. PVC side wall. (2) Sulfuric acid electrolyte. (3) Cathodes (4) Copper bussing (5). Flight bar.

The concentration and temperature of the electrolyte are 180 g/L and 20 °C. Current is flowed in from an external power source, DC rectifier, through cables (4) into the bussing holding the flight bar (5). The bussing, flight bar and cables bringing current to the system are all made from 99% purity copper. The dimensions of the bussing are all the same at 5.1 cm x 1.27 cm thick. From the flight bar, the current flows through the anode and into the electrolyte. From there current flows to the cathodes (3) into the bussing (4) and then back to the power supply to complete the circuit. The cathodes are made from 6063 aluminum and are 8.8 x 2.75 by 40.0 cm. The four corner cathodes are masked in the electrolyte for this experiment.

Voltage, amperage, and amp/hours are controlled on a module (Model: UPC 5000 RC-2 D P18/1000-24VN-C0, American Plating Power LLC, Florida) and are calibrated to NIST (+/- 0.1V, 0.1A). UPC 5000 module, **Figure 2.2**, is connected by a 50-mA shunt to the DC rectifier. All processing parameters are data logged and exported to CSV.file on Microsoft Excel 2013.

Temperature is regulated by a two output/input controller (Model: CNi16D33 +/- 0.05 °C stability, Omega Engineering, Connecticut.) and calibrated to NIST (+/- 0.05°C). Heating and cooling of the tank are controlled externally. Chilling solution (Propylene Glycol @ - 2.39 °C (+/-0.25 °C)) is flowed into exchangers at the bottom of tank. Exchanger material is made of 316 stainless steel 2.54 cm diameter piping. The exchanger is u-shaped with the bottom of the u running along the bottom of the tank and the exit running on the opposite side of the entry point.

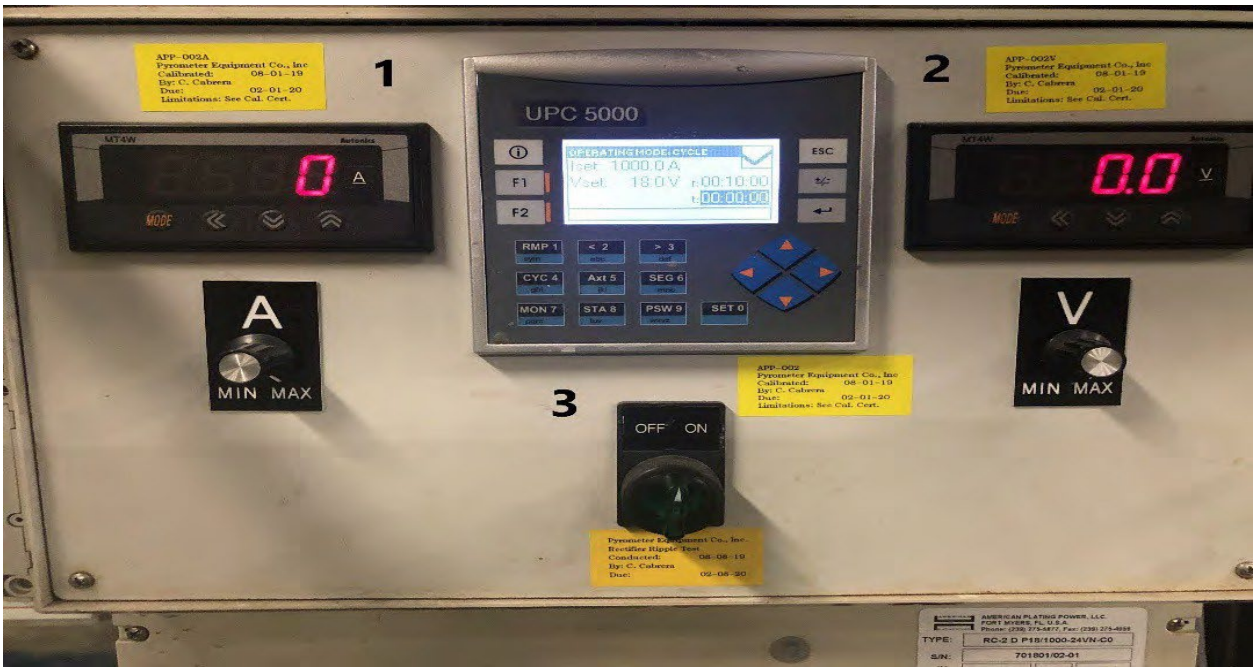

Figure 2.2 UPC 5000 computer module. (1) monitors the amperage on the system and (2) monitors the voltage on the system. To set the ramping process, the number of steps and current density levels were set in the touch screen (3).

The heating element is made of 316 stainless steel pipe containing low pressure steam @ 121 °C (+/- 1.5 °C). The heating exchanger is a typical steam coil. The 2.54 cm diameter feed pipe splits into 20, 1.27 cm diameter 316 stainless steel pipes which pass the heat through the back side of the tank. A 2.54 cm diameter pipe brings the condensate from the coil out to a wastewater stream. Heating and or cooling of electrolyte is done prior to processing of specimens. Temperature is monitored continuously and any fluctuations of (+/- 0.2 °C) lead to rejected samples.

Air agitation, **Figure 2.3**, is brought in via external low-pressure blower system (Preeva, Reznor, Missouri). Air agitation is regulated using a pressure gauge (4" liquid filled, SPAN, Wisconsin) calibrated to NIST (+/- 690 pa). Air agitation is regulated to $1.7e^5$ pa and brought into the tank using Schedule 80, 2.54 cm diameter piping. That pipe is then fed into a 3.81 cm diameter header pipe made from the same material. The head pipe feeds into four 1.27 cm diameter pipes spreading out along the bottom of the tank evenly. On these four pipes, holes measuring 0.16 cm.

Figure 2.3 (1) Air agitation. (2) Chilling solution. (3) Heating exchanger. (4) Cathode.

Note: Inside look at processing tank. (1) Air agitation is brought into the tank using Schedule 80, 2.54 cm diameter piping. That pipe is then fed into a 3.81 cm diameter header pipe made from the same material. The head pipe feeds into four 1.27 cm diameter pipes spreading out along the bottom of the tank evenly. On these four pipes, holes measuring 0.16 cm diameter spaced at 2.54 cm intervals are used to introduce air into the tank. Chilling solution (Propylene Glycol @ - 2.39 °C (+/- 0.25 °C)) is flowed into exchangers at bottom of tank. Exchanger material is made of 316 stainless steel 2.54 cm diameter piping. The exchanger is u-shaped with the bottom of the u running along the bottom of the tank and the exit running on the opposite side of the entry point. The heating element is made of 316 stainless steel pipe containing low pressure steam @ 121 °C (+/- 1.5 °C). The heating exchanger is a typical steam coil. The 2.54 cm diameter feed pipe splits into 20 1.27 cm diameter 316 stainless steel pipes which pass the heat through the back side of the tank. A 2.54 cm diameter pipe brings the condensate from the coil out to a wastewater stream. A 6063 aluminum 8.8 by 2.75 by 40.0 cm cathode (4) is placed in front of the heater to prevent shielding during processing.

diameter spaced at 2.54 cm intervals are used to introduce air into the tank. Electrolyte concentration is measured at the beginning, middle and end of the process for process consistency (0, 15, 30 mins of process time (+/- 5s)). Concentration of sulfuric acid (g/L) and aluminum content (g/L) are monitored by wet chemistry methods found in Appendix A, Sulfuric Electrolyte Concentration Procedure. Sulfuric acid and aluminum concentrations are maintained by adding reagent grade 66° Be sulfuric acid (Sulfuric66be, Independent Chemical, New Jersey) or decanting electrolyte and adding back deionized water (ASTM D1193 Reagent Grade IV, 0.2 MΩ·cm, 5.0 to 8.0 pH).. All chemicals used in analyzing of electrolyte are reagent grade.

2.2 Anodization Process including Pre-Treatment

2.2.1 Aerospace aluminum alloy samples

Aluminum alloys 7075-T6 and 2024- T3 were chosen for experimentation. **Tables 2.1 and 2.2** show compositional analysis of the alloys. These two alloys were chosen because of the difficult nature of anodizing these alloys and the importance they have on the aerospace industry.

Table 2.1 Material Composition of AA7075 – T6

Material (%)	Aluminum	Zinc	Magnesium	Copper	Iron	Silicon	Chromium	Other
AA7075	Balance	5.2	1.95	1.22	0.25	0.23	0.17	0.08

Table 2.2 Material Composition of AA2024 – T3

Material (%)	Aluminum	Magnesium	Silicon	Iron	Copper	Chromium	Manganese
AA2024	Balance	1.2	0.5	0.5	3.8	0.1	0.3

2.2.2 Sample preparation and process

Samples were bought from Anacon 1st Choice, California, and each process specimen came with a plastic wrapping. All specimens were purchased as 10 x 10 x 0.16 cm squares with a 0.64 cm diameter in hole in the middle. Samples were then further cut to 2.54 x 2.54 x 0.16 cm squares using a diamond blade and portable bandsaw. Specimens were then deburred to reduce sharp edges. All samples were cleaned with reagent grade acetone (A1020, Spectrum Chemical, New Jersey) prior to racking. Samples were racked on a custom built 6063 aluminum rack. Rack configuration can be seen in **Figure 2.4**. The rack was built at Aerotech.

Figure 2.4 Rack used for chemical processing of test specimens in Chapter 3.

Note: The total surface area of the rack is 0.097 m^2. The spline, which is the area that holds the clips and attaches to the flight bar at the top, is 3.81 wide by 66.04 cm long. The two clips at the top and at the bottom and the same pieces of material, just cut on the bottom to be taller. The clips are used to hold larger test specimens for taber abrasion. The dimensions of the clips are 12.7 cm long by 5.08 cm around. The center racking clips are used to hold the smaller specimens used for XRD, SEM and hardness. The center of the clip is 3.81 cm wide by 25.4 cm long. There are 16 fingers which hold the specimens by compression. The dimensions of the fingers are 0.635 cm around by 20.32 cm long. the total area of the rack is 968 $cm^2 \approx 0.097 m^2$. The rack area varies depending on the experiment.

Chemical processing methods and solution variables are described in **Table 2.3**. The chemical processing order of operations can be found in **Figure 2.5**. Surface preparation chemicals and processing was done in lab prior to anodization. All specimens were rinsed with deionized water in between processing steps. Multiple methods of anodizing were applied to samples and compared. Example processing voltage and times are explained in **Table 2.4**. The standard conditions for anodizing take place in a 180 g/L sulfuric acid bath set up with heating and cooling with air agitation. The temperature was kept at 20 °C during anodization.

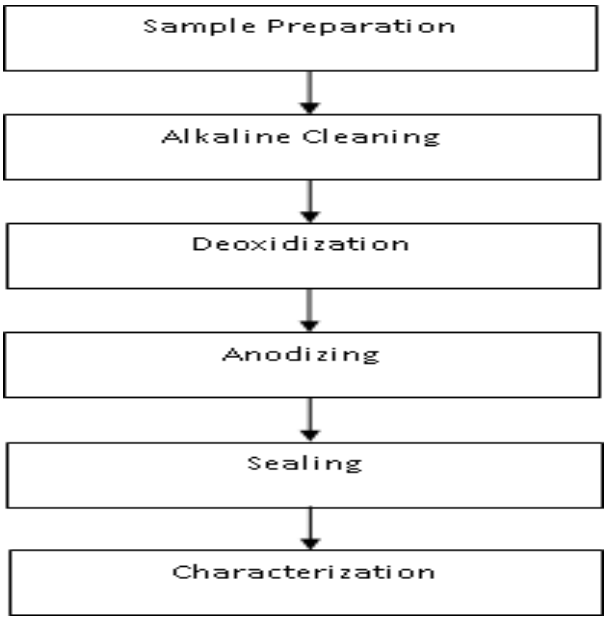

Figure 2.5 Process flow chart from sample preparation to characterization testing.

After the samples left the deoxidization step, they were rinsed in deionized water for 2 minutes and put into the anodize tank. Upon immersion into the tank, current was applied to the samples. Each ramp will be 10 minutes long and the remainder of the run will be 20 minutes. The baseline or standard process does not have a ramping period. This in total will be a 30-minute process. Each ramp will have a different starting and ending current density. The differences in current densities are done by design to see what impact the current density has on the process. The total amount of current passing through the system is measured in coulombs, C. C is kept consistent in each process or parts of a process to ensure process similarity. After anodization, the parts were removed from the electrolyte within 1 minute and rinsed thoroughly with deionized water for 2 minutes.

Table 2.3 Processing Parameters for all Chemical Processing

Process Method	Chemical	Time (Minutes)	Concentration (g/L)	Temperature (°C)
Cleaning	Bonderite C-AK 4215 NCLT	10	50	50
Deoxidizing	Deoxidizer LNC	5	40	20
Anodizing	66° be Sulfuric Acid	30	180	20
Rinsing	Deionized Water	2	0	20
Sealing	Anodal Ms-1 New	20	20	90

Note: Parts are immersed in alkaline cleaner (785191, Henkel AG & Co., Germany) for 10 minutes (+/- 0.25 mins) to remove all oil, grease and FOD from the test specimens. Test specimens were then rinsed for 2 minutes in room temperature deionized water. Specimens were then deoxidized (Oakite Deoxidizer LNC, BASF, Germany) to chemically activate the surface and remove any natural oxide that may haveformed. Test specimens were then rinsed for 2 minutes in room temperature deionized water. Anodizing of specimens was performed immediately after rinsing. Test specimens were then rinsed for 2 minutes in room temperature deionized water. Test specimens that are being used for corrosion resistance were then sealed (Anodal MS-1, Clariant, Switzerland) and rinsed for 2 minutes at room temperature. Parts were air dried at room temperature after chemical processing.

Amperes used in processing were calculated using Equation (2.1):

$$A = XJ \tag{2.1}$$

Where: A is ampere, X is area in m^2, J is current density in A/m^2.

Coulombs were calculated using Equation (2.2):

$$C = 60AM \tag{2.2}$$

Where: C is Coulombs in A x sec, A is ampere, and M is minutes. Minutes are a designated number for time in which a certain current density level is used in the process; 60 is the conversion factor from minutes to seconds. Current densities were chosen based off literature review and industry knowledge of typical anodizing practices. **Table 2.4** is an example of the process outline used in **Chapter 3, Multistep Anodization of 7075-T6 Aluminum Alloy**.

Table 2.4 Four Ramps Chosen for Analysis

Ramp 1 (R1)			
Mins	Current Density (A/m2)	Coulombs (C)	Amps (A)
30	111.2	38840	22
Ramp 2 (R2)			
Mins	Current Density (A/m2)	Coulombs (C)	Amps (A)
5	64.6	3759	13
5	86.1	5011	17
20	129.2	30070	25
Ramp 3 (R3)			
Mins	Current Density (A/m2)	Coulombs (C)	Amps (A)
2.5	43.1	1253	8
2.5	64.6	1879	13
2.5	86.1	2506	17
2.5	107.6	3132	21
20	129.2	30070	25
Ramp 4 (R4)			
Mins	Current Density (A/m2)	Coulombs (C)	Amps (A)
1.25	32.3	470	6
1.25	43.1	626	8
1.25	53.8	783	10
1.25	64.6	940	13
1.25	86.1	1253	17
1.25	96.9	1410	19
1.25	107.6	1566	21
1.25	118.4	1723	23
20	129.2	30070	25

Note: Ramp 1, R1, is a common processing method in industry. Ramp 2, R2, is a stepped ramp with two steps. Ramp 3, R3, is a stepped ramp with four steps. Ramp 4, R4, is a stepped ramp with eight steps. Each ramp will have different starting and stopping voltages as the current density is being varied in the study.

CHAPTER 3

MULTISTEP ANODIZATION OF 7075 – T6 ALUMINUM ALLOY

3.1 Introduction

Anodizing is an electrochemical method used to transform aluminum to aluminum oxide in the coating layer. Although being thin, this layer can substantially increase the abrasion and corrosion resistance of aluminum [2,4,11]. Aluminum alloys are complexed with zinc, copper and other alloying elements to provide high mechanical strength have relatively low abrasion and corrosion resistance [5,6,11,84]. Thus, they are usually anodized to improve abrasion and corrosion resistance [7]. The major difficulty in anodizing these alloys is related to the compositional heterogeneity that is even more accentuated in heat-treatable alloys in which an increase in mechanical strength is achieved by forming several intermetallic precipitates [11,18,85]. The presence of intermetallic compounds facilitates the appearance of defects during anodization by generating a spatially non-uniform distribution of electric current in the alloy matrix. It leads to uneven growth of anodic oxides and surface burning, especially when higher voltages and current densities are applied [1,11,75-77]. The burning of film is caused by a runaway dissolution at the oxide surface that occurs when the current density is locally spiked. Spikes in the current density, loose powdery coating, insufficient micro adhesion, and evolution of oxygen gas bubbles at the oxide surface are all common issues that decrease the anodization efficiency and are exacerbated by anodizing at higher voltages and currents [1,11,17,18,52,54,60,61,75-79].

While surface electro-chemical reactions forming the oxide layer are governed by the current density, application of a voltage is required to run the anodization process [11,18,73]. Since

the electric resistance of aluminum oxides is much higher than that of aluminum alloys, the anodizing current drastically decreases with time at a constant applied voltage [1,77,84,86]. However, the use of a high voltage for the entire process would significantly raise chances of burning the oxide surface. A compensation approach is to run the entire process at median voltages [73]. However, this strategy does not allow for a large surface area load, increases the energy usage by requiring a larger tank time needed per load, and still brings a higher rate of forming processing defects, especially in anodization of heat-treatable aluminum alloys. This approach is therefore problematic as the appearance of processing defects typically would cause scraping of a metal part, which can be exceedingly costly due to the lead time, machining labor and material cost put into it. Accordingly, these anodizing regimes are of limited use in an industry where profit margins are typically low.

Several recent studies demonstrated that the use of "stepwise anodization," a process by raising the magnitude of an applied voltage or an electric current during anodization [18,80] can improve surface properties of heat- treatable aluminum alloys, but the outcome was found to strongly depend on various factors, such as the alloy composition, bath type and temperature [81-82]. In stepwise anodizing, the voltage is incrementally increased overtime until the final current or voltage is reached, thereby allowing the use of a lower initial voltage to start the process. It is believed that the use of lower initial voltages and current densities allows non-aluminum ions to migrate out of the forming aluminum oxide [56] and/or dissolve in an electrolyte when an electric current is applied [83]. In these studies, anodization was controlled by voltage or by current accompanied with voltage pulses. While pulsing can improve mechanical properties of anodized coatings [77,87-90], the cost of required equipment is too expensive on a large industrial scale. Other studies on improvement of anodization of heat-treatable aluminum alloys rely on adding chemical compounds into an anodizing electrolyte and/or changing the temperature to influence

the coating formation. Due to the cost and industry restrictions, some of these options are however of limited use in large scale industrial applications.

While stepwise variation of an applied electric current was shown to have the potential to improve the microstructure and mechanical properties of anodized coatings, it remains unclear how often we need to ramp the current density to improve the properties of anodized coatings on heat treatable aluminum alloys. The present study explores the influence of ramping the electric current in two, four, and eight steps while anodizing on the microstructure, thickness, micro-hardness, corrosion, and abrasion resistance of coatings formed on a heat-treated wrought aluminum alloy AA 7075-T6 with zinc as the primary alloying element [20]. This alloy is extensively used in aerospace, automotive, and fracture-critical applications because of its unique combination of high mechanical properties, great strength to weight ratio and resistance to fatigue. However, it does not anodize well in conventional processing at a constant current due to the presence of complex intermetallic phases [17,18,73,75]. AA 7075-T6 was therefore selected for our studies to demonstrate that compared to a constant current regime multi-step anodization substantially improves the overall process efficiency.

3.2 Materials and Experimental Procedures

3.2.1 Anodizing process

The anodizing process was performed in an electrochemical cell, **Figure 3.1**, in which voltage, amperage, and transferred charge (current multiplied by time) are controlled with the module UPC 5000 RC-2 D P18/1000-24VN-C0, American Plating Power LLC, Florida. The UPC 5000 module was connected by a 50-*mA* shunt to the DC rectifier (American Plating Power LLC, Florida) (1). Measurements from units 2-4 were data logged and exported to CSV.file on Microsoft Excel 2013 (5). The tank walls were made of chemical resistant polyvinylchloride. The electrolyte temperature

was regulated by a two-output/input controller (CNi16D33 +/- 0.05 °*C* stability, Omega Engineering, Connecticut) calibrated to NIST (+/- 0.05°*C*). Heating and cooling of the tank were controlled externally. Chilling solution (Propylene Glycol @ - 2.39 °*C* +/- 0.25 °*C*) was flowed into exchangers at the tank bottom (C – 9). The heating element was made of 316 stainless steel pipe containing low pressure steam at 121 °*C* +/- 1.5 °*C* (H-10). The solution was agitated using constant low-pressure air (8). The cathodes (7) and the spline/hook (6) that submerged the anode into the electrolyte were made of two 8.8 x 2.75 x 40.0 *cm* 6063 aluminum extruded bars provided by Tilton Rack Corp, New Jersey. The cathode to anode ratio for all experiments was at 1:1 ratio based on square meters. There was one cathode on each side of the tank for even distribution of an electric current.

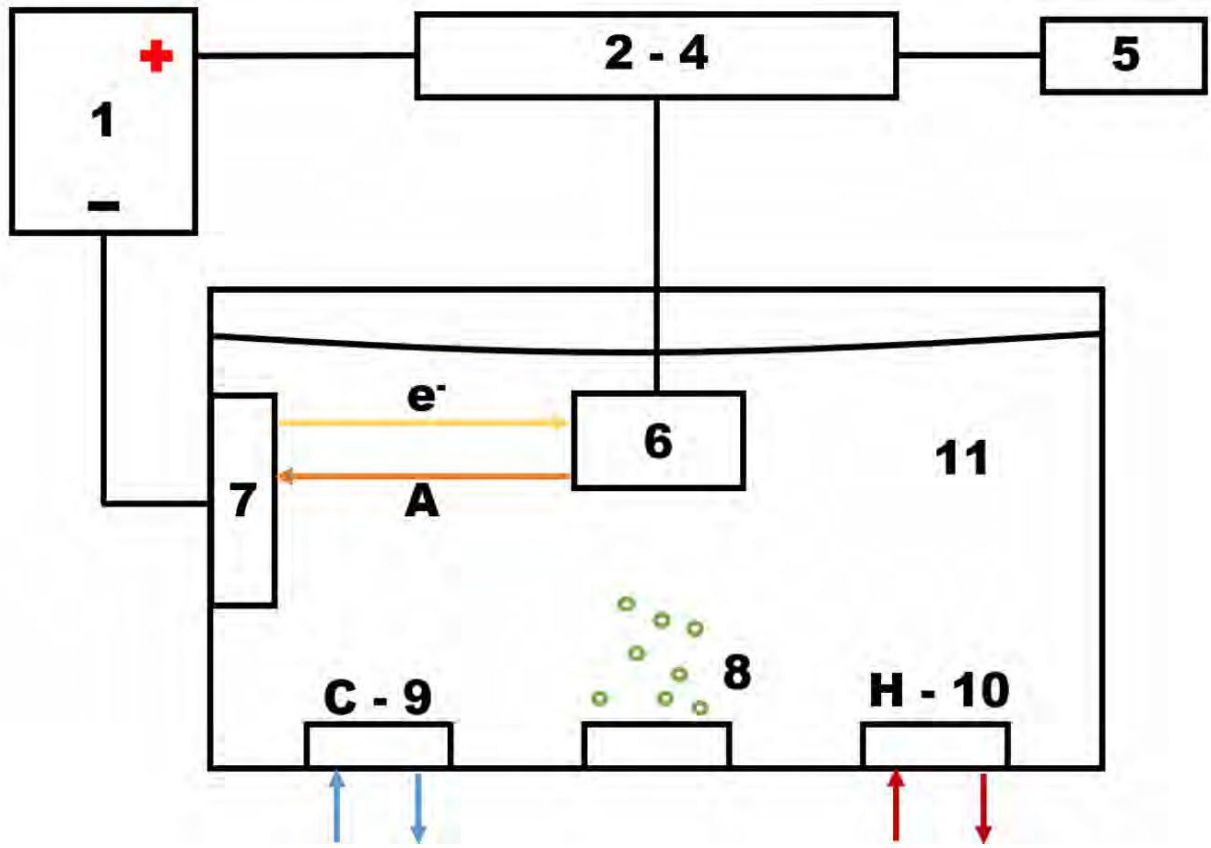

Figure 3.1 Anodizing system: 1) power supply, 2) voltmeter, 3) ammeter, 4) amp-hour meter, 5) computer, 6) anode, 7) cathode, 8) air agitation, 9) cooling system, 10) heating system, 11) electrolytic solution.

Experiments were carried out on AA7075-T6 provided by Anacon 1st Choice, 425 W LA Cadena Riverside, California. Its chemical composition is given in Table 1. All specimens were purchased as 10 x 10 x 0.16 *cm* squares with a hole of 0.64 *cm* diameter in the middle.

Specimens (6) were then further cut to 2.54 x 2.54 x 0.16 *cm* squares using a diamond blade and a portable bandsaw and then deburred to reduce sharp edges. Prior to chemical cleaning and acid etching, all samples were cleaned with reagent-grade acetone prior to racking to remove glue and ink. The samples were then racked and chemically processed to clean and prepare the surface for anodization. The preparation steps in order consisted of alkaline cleaner, NaOH, for 10 minutes, followed by a pickling process in a ferric sulfate/nitric acid bath for 5 minutes. Samples were rinsed in between each chemical step. After the preparation steps, samples were anodized at room temperature, 20 *°C,* for 30 minutes. The electrolyte (11) consisted of sulfuric acid, 180 *g/L*. Samples were anodized at room temperature, 20 *°C,* for 30 minutes. After anodization, the samples were cleaned in deionized water and air dried. Samples that underwent corrosion resistance testing were sealed in a 2.0 *v/v %* nickel acetate solution for 20 minutes and 90 *°C*. The area of each load is 0.194 m^2 with 0.097 m^2 being the rack area and 0.097 m^2 being the part area.

Table 3.1 Composition of AA7075-T6 Provided by Anacon 1st Choice, 425 W LA Cadena Riverside, California

Material (%)	Al	Zn	Mg	Cu	Fe	Si	Cr	Other
AA7075	Bal	5.2	1.95	1.22	0.25	0.23	0.17	0.08

Four anodization regimes were studied: a conventional R1 with a constant electric current and R2, R3, R4 with raising current in two, four and eight ramping steps, respectively. Process R1 is considered as the baseline for comparison. Ramping of an applied electric current in processes

R2, R3, and R4 is conducted for 10 minutes, and the remaining 20-min period of each anodizing process is performed at a constant current, **Table 3.2**.

The total electric charge passing through the system during anodization was taken as the basic parameter to characterize the outcome of the overall anodizing reaction at the aluminum surface. Magnitudes of the starting and ending electric currents in each step of processes R2, R3, and R4 were therefore designed to have the total electric charge transferred in these processes the same as that in process R1, **Table 3.2**. Magnitudes of electric current and charge listed in **Table 3.2** were calculated using Equation (3.1):

$$A = X \cdot J \tag{3.1}$$

Where A is the current in amperes, X is the area in m^2, and J is the current density in A/m^2. The electric charge transferred during the processing was calculated using Equation (3.2):

$$C = 60 \cdot A \cdot M \tag{3.2}$$

where C is Coulomb = $A \cdot sec$, A is in amperes and M is the period in minutes during which a certain current is applied, 60 is the conversion factor from minutes to seconds. Computed values of the anodizing electric current and the expected transferred electric charge for processes R1, R2, R3, and R4 are summarized in Table 3.2. Process R2 has two ramp stages, process R3 has four and process R4 has eight (Table 3.2). Process R1 is considered as the baseline for comparison. In processes R2, R3, and R4, ramping of an applied electric current is conducted for 10 minutes and the remaining 20-minute period is performed at a constant current (Table 3.2).

Table 3.2 Anodizing Regimes Designed for Experiments. A Common Process with a Constant Electric Current, R1, and Processes with Two, R2, Four, R3, and Eight, R4, Steps of Current Ramping. Each Ramp had Different Starting and Stopping Voltages as the Current Varied in the Course of Anodization. The Expected Values of Electric Charge for the Designed Regimes of Anodization were Computed with the use of Equations (2.1) and (2.2)

Process 1 (R1)			
Mins	A/m^2	Charge (C)	Amps
30	111.2	39600	22
Process 2 (R2)			
Mins	A/m^2	Charge (C)	Amps
5	64.6	3900	13
5	86.1	5100	17
20	129.2	30000	25
Process 3 (R3)			
Mins	A/m^2	Charge (C)	Amps
2.5	43.1	1200	8
2.5	64.6	1950	13
2.5	86.1	2550	17
2.5	107.6	3150	21
20	129.2	30000	25
Process 4 (R4)			
Mins	A/m^2	Charge (C)	Amps
1.25	32.3	450	6
1.25	43.1	600	8
1.25	53.8	750	10
1.25	64.6	975	13
1.25	86.1	1275	17
1.25	96.9	1425	19
1.25	107.6	1575	21
1.25	118.4	1725	23
20	129.2	30000	25

3.2.2 Characterization techniques

3.2.2.1 Processing parameters. The values of actual voltage, amperage, and transferred electric charge were measured with the use a module UPC 5000 calibrated to NIST (+/- 0.1 *V*, 0.1 *A*). The presented voltage, amperage, and charge are values averaged over three repeated process runs.

3.2.2.2 SEM/EDS. Surface morphology of anodized samples was observed by scanning electron microscopy (SEM, JEOL JSM-7900F FE-SEM). Energy Dispersive X-Ray Spectroscopy (EDS) scanning of the alloying elements over the surface of an anodized sample was conducted using the program AZTEC, JEOL. All samples were gold sputtered and EDS measurements were analyzed using 5 *kV*. Microscopy images at 1700x were obtained for R1, R3 and R4, 1900x magnification was usedfor R2. These images were obtained using 2.0 *kV*, under LED and the height of the specimen stage,WD, differed for each ramp, R1) 19.8 *mm*, R2) 25.1 *mm*, R3) 25.1 *mm* and R4) 24.7 *mm*. For Fig. 4 (a-d), microscopy views at 19,000x were obtained using 5.0 *kV*, under LED and the height of thespecimen stage, WD, was 10.0 *mm*. High-magnification microscopy images at 100,000x were obtained using 10.0 *kV*, under LED and the height of the specimen stage, WD, was 10.0 *mm*. The National Institutes of Health (NIH) open-source image processing software ImageJ [91] was used to compute the porosity, pore diameter and the interpore distance in high-magnification SEM images (100,000x). The processing of an original SEM image combined a sequence of standard ImageJ procedures: Set the image scale in pixels/micrometer based on the scale bar in the image equal to 100 nanometers; convert image type to 8-bit grayscale; reduce noise and enhances image contrast by using histogram equalization; use flat-field-correction and subtract background to correct for uneven illumination, use a locally adaptive thresholding technique to detect the boundaries between different regions in the image, and select a region of interest (ROI) to automatically compute the pore size.

Depth of structure was measured by measuring the radius of the opening to solid film and rotating the image to align it vertically. After rotation, the distance between the two sides of the right triangle was measured and compared to the scale of the image. Three SEM images and readings were taken for each anodized sample and the presented result is averaged over three repeated anodizing processes.

3.2.2.3 Microhardness. Microhardness of anodized samples was measured by a digital Vickers tester (Durascan 50, Struers, Ohio) with a 10 *g* load for 15*s*. Two micro-hardness readings were taken for each anodized sample and the presented result is averaged over three repeated anodizing processes.

3.2.2.4 Wear resistance. Test panels for abrasion resistance were conditioned at 51% relative humidity (*RH)* and 23°*C* for 48 hours before testing. After conditioning, panels were weighed to the nearest +/-.0001 *g* with an Ohaus digital balance (PA224, Ohaus, New Jersey). Weighting was performed outside the test chamber. After weighing, panels were positioned on the Taber abraser and allowed to re- condition for 2 hours. Abrasion CS-17 wheels (CS-17, Taber, New York) with a 1000 *g* load were used to provide a course surface. Following the American Society for Testing and Materials (ASTM) D4060 standard, the Taber abraser was placed inside the SCCH high humidity chamber to condition the testing environment. Abrasion resistance was tested on two anodized samples per process and the presented result is averaged over three repeated anodizing processes.

3.2.2.5 Corrosion resistance. Testing of corrosion resistance was conducted using 10 x 10 x 0.16 *cm* test panels that were anodized and sealed in Anodal MS-1 New (Reliant Aluminum

Products, North Carolina) for 20 minutes at 90 °*C*. The system used to create the corrosive environment is a Q-Fog Cyclic Corrosion Chamber (Q-Fog/SSP600, Q-LAB, Florida). Test panels were tested in accordance with ASTM B117. One anodized sample per process was tested, and the presented result is averaged over three repeated anodizing processes.

3.2.2.6 Coating thickness. Measurements of the coating thickness were taken after air drying of anodized specimens at temperature of 20.0 °*C* for about for 1 hour (+/- 5 minutes). The coating thickness was measured with an Eddy current tester (Positector 6000, Deflesko, New York). Four thickness readings were taken for every anodized sample and the presented result is averaged over three repeated anodizing processes.

3.2.2.7 X-ray diffraction . X-ray diffraction (XRD) measurements were conducted on EMPYREAN, Malvern PANalytical, UK at an incident angle 5° in parallel beam geometry with Rigaku Optima IV diffractometer equipped with CuKα radiation. Two scans at the operating parameters of 40 *mA*, 45 *kV* and 0.5° min^{-1} scanning speed were conducted for every anodized sample and the presented result is averaged over three repeated anodizing processes. To reduce the signal from the substrate and enhance the signal from the coating, two scans with a grazing incident angle of 2^0 at the same operating parameters and scanning speed were also conducted for every anodized sample and the result was averaged over three repeated anodizing processes.

3.2.2.8 Percent difference. The percentage difference between two experimental values, val_1 and val_2, was calculated using Equation (3.3):

$$\text{Difference } (\%) = 100 \cdot \frac{\text{val}_1 - \text{val}_2}{(\text{val}_1 + \text{val}_2)/2} \tag{3.3}$$

3.2.2.9 Statistical Analysis. In the statistical analysis of data, measurements of the anodic coating characteristics were arranged in comparison groups: Group 1 (R1,R2) and Group 2 (R3,R4). The F-test of equality of variances was used to determine whether both populations have the same variance [92]. The null hypothesis of an experiment states that a difference between measurements within a particular group compared with the other group appeared by chance. The alternative hypothesis is that this difference was influenced by differences in anodizing processes. The following three-step procedure performed with Analysis of Variance (ANOVA) Microsoft Excel was used for testing the null hypothesis: (1) compute the mean and variance of measurements for each of two groups, (2) compute the overall mean and variance for both groups taken together, and (3) compute the F factor as the ratio between the mean variability of measurements within one group and the mean variability of data within both groups taken together. The value of the F factor will be large only if the variability between the groups is large compared to the variability within both groups taken together. The number of measurements in each group, the total number of measurements and the chosen alpha level, α, yield the confidence level $100 \cdot (1 - \alpha)\%$ [92]. There are two criteria for rejecting or accepting the null hypothesis. One is to calculate F_α that is a function of α: F should exceed F_α for the null hypothesis to be rejected. The other is to calculate the P_α −value that is a function of α for rejecting, $\alpha > P_\alpha$, or accepting, $\alpha \leq P_\alpha$, the null hypothesis. The reported results of F-tests were conducted for $\alpha = 0.05$ corresponding to the confidence level of 95%.

3.3 Results and Discussion

3.3.1 Thickness of anodized layer

Measurements of the layer thickness with the use of the eddy current testing technique are presented in **Table 3.3**. Results of processes R3 and R4 are similar in terms of the layer thickness while both those processes formed layers larger by 23.2% and 25.4% than R1 over the same processing time. The observed differences in the coating thickness are larger than 10%-15% variation of the layer thickness over the sample surface allowed in anodization processes. The results of statistical analysis presented in **Table 3.3** demonstrate that a difference between the influence of anodizing processes in Group 1 and Group 2 on the coating thickness is statistically significant as $FF > FF_{0.05}$ and $0.05 > PP_{0.05}$.

3.3.2 Microhardness of anodized samples

Table 3.3 lists the average micro-hardness values in *MPa*. Note that the coating thickness on a sample influenced its hardness due to the relative softness of the aluminum underneath. Compared to standard process R1, hardness of coatings formed in processes R2, R3, and R4 increased by 4.3%, 10.3%, 14.6%, respectively. The presented measurements indicate that oxide coatings built in processes R3 and R4 are more compact throughout the anodized surface. The results of statistical analysis presented in **Table 3.3** demonstrate that a difference between the influence of anodizing processes in Group 1 and Group 2 on the microhardness is statistically significant as $FF > FF_{0.05}$ and $0.05 > PP_{0.05}$.

Table 3.3 The Thickness of Coatings (μm) Formed in Processes R1, R2, R3, and R4 was Measured by Eddy Current Testing Technique. Presented Values were Averaged Over Three Repeated Anodizing Processes with Four Thickness Readings Taken for Each Sample. Microhardness (MPa) of Coatings Formed in Processes R1, R2, R3, and R4 were Analyzed by Taking Two Microhardness Readings for Each Anodized Sample and Repeated Over Three Anodizing Processes. Statistical Analysis of Data Between Processes in Group 1 (R1 & R2) and Group 2 (R3 & R4) for the Overall Process is Listed Below

Process	Thickness (μm)	Avg. Hardness (MPa)			
R1	10.2 ± 0.18	1169 ± 17			
R2	11.0 ± 0.17	1220 ± 28			
R3	13.0 ± 0.16	1296 ± 18			
R4	13.3 ± 0.18	1353 ± 16			
Thickness					
Group	Count	Average	$P_{0.05}$	F	$F_{0.05}$
Group 1	24	10.6 ± 0.5	6.7E-17	167.0	4.1
Group 2	24	13.1 ± 1.8			
Hardness					
Group	Count	Average	$P_{0.05}$	F	$F_{0.05}$
Group 1	12	1194 ± 34	5.9E-09	84.0	4.3
Group 2	12	1324 ± 35			

3.3.3 Corrosion resistance of anodized samples

All test specimens passed the acceptance criteria for the 336-hour salt spray test. Coatings formed in processes R1 and R4 did not exhibit corrosion pits, see **Figure 3.2**. The powdery finish observed on the surface of the oxide layer built in R1 process did not affect the coatings resistance to corrosion. This in fact means that the coating underneath the burned layer did properly seal to protect the base metal from galvanic corrosion. However, coatings formed in processes R2 and R3

did exhibit a single corrosion pit. According to [93], localized corrosion on anodized aluminum alloys is likely caused by microgalvanic coupling between the different metallographic phases. While these panels were still compliant to the testing standard, their performance was worse compared to anodizing in processes R1 and R4. The presented results indicate that ramping of the current density more frequently does not directly affect the coating corrosion resistance, that is controlled by the ability to seal the aluminum oxide pores.

3.3.4 Abrasion resistance of anodized samples

Abrasion resistance was characterized by calculating the weight of the anodic coating removed following a predetermined number of abrasive cycles. The weight loss measurements for each sample are listed in **Table 3.4.**

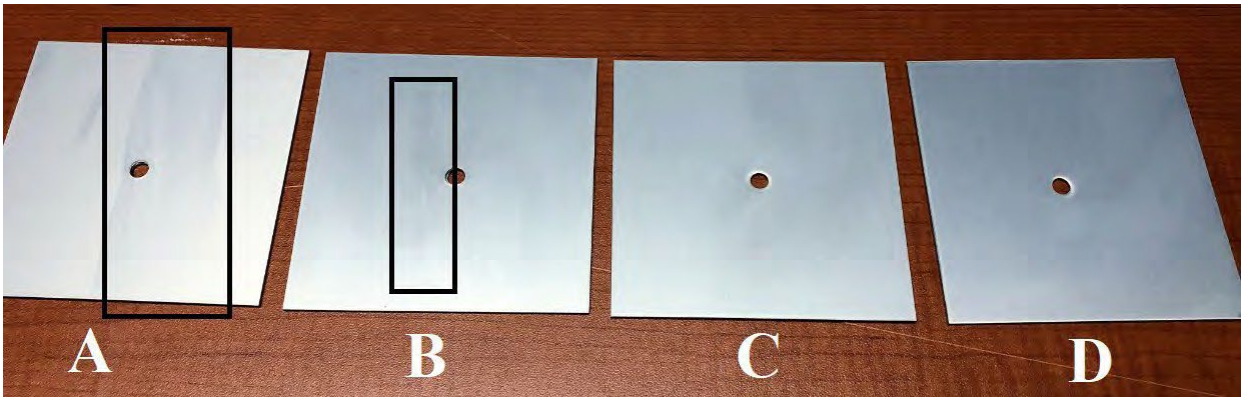

Figure 3.2 Appearance of four 10 x 10 x 0.16 cm anodized specimens after drying. (A) is R1, B) is R2, (C) is R3, (D) is R4. It can be seen inside the black boxes that the top layer of anodic film is loose and powdery and comes off with little to no resistance.

Table 3.4 Weight Loss in mg of Specimens. Specimens were Conditioned and Processed at 51% RH and 23 °C. Abrasion Resistance was Tested on Two Anodized Samples per Process and the Presented Result is Averaged Over Three Repeated Anodizing Processes of R1, R2, R3, and R4. Statistical Analysis of Data Between Processes in Group 1 (R1 & R2) and Group 2 (R3 & R4) for the Overall Process is Listed Below

	Processes				
	R1	R2	R3	R4	
Wt. loss in mg	18.8 ± 0.48	13.1 ± 0.36	11.8 ± 0.27	8.6 ± 0.27	
	20.3 ± 0.48	15.5 ± 0.36	10.8 ± 0.27	8.2 ± 0.27	
	17.7 ± 0.48	14.8 ± 0.36	11.4 ± 0.27	9.7 ± 0.27	
	17.4 ± 0.48	15.4 ± 0.36	10.2 ± 0.27	7.8 ± 0.27	
	19.8 ± 0.48	14.6 ± 0.36	9.9 ± 0.27	9 ± 0.27	
	17.3 ± 0.48	15.7 ± 0.36	10.6 ± 0.27	7.9 ± 0.27	
Average	18.55 ± 0.48	14.85 ± 0.36	10.78 ± 0.27	8.53 ± 0.27	
Group	Count	Average	$P_{0.05}$	F	$F_{0.05}$
Group 1	12	16.7 ± 2.2	3.8E-09	88.0	4.3
Group 2	12	9.7 ± 1.9			

Compared to R1, processes R2, R3 and R4 provided a higher abrasion resistance by reducing the weight loss on 22.2%, 53.0%, and 74.0%, respectively. Plots in **Figure 3.3** illustrate the relation between the average weight loss of coating and the final voltage of the anodizing process. As can be seen in **Figure 3.3**, the abrasion resistance was increasing with lowering the final voltage. This trend is caused by improvement of the coating compactness due to reduced heating of forming oxides. The results of statistical analysis presented in **Table 3.4** demonstrate that a difference between the influence of anodizing processes in Group 1 and Group 2 on the abrasion resistance is statistically significant as $FF > FF_{0.05}$ and $0.05 > PP_{0.05}$.

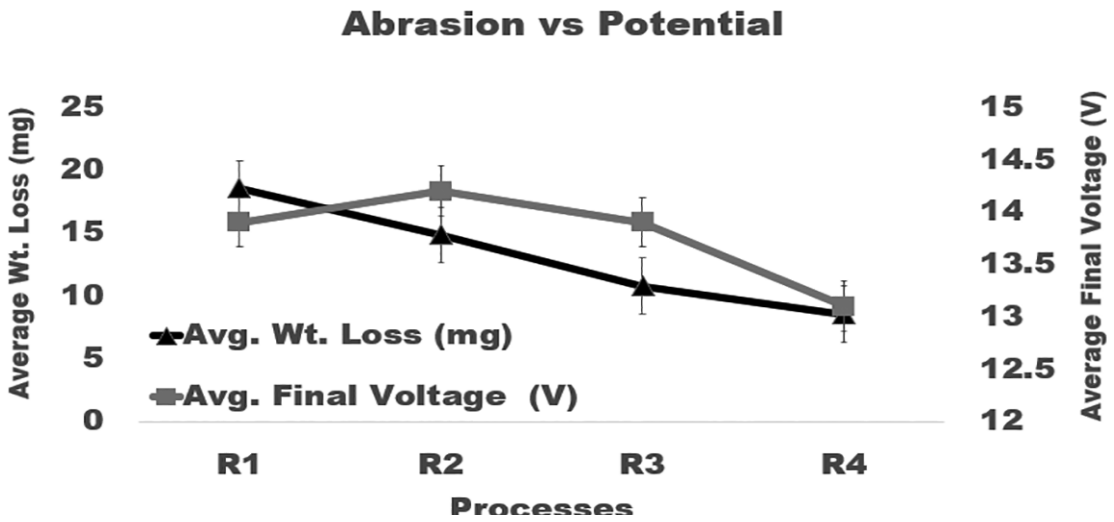

Figure 3.3 Graph of average wt. loss, mg, versus average final voltage, V. Whereas the blue line represents average wt. loss, and the red line represents average final voltage. A downward trend in wt. loss is noticed from R1 ➔ R4.

3.3.5 SEM/EDS analysis

The low magnification SEM images of coating surface morphology formed in processes R1, R2, R3, and R4 are presented in **Figure 3.4**. The surface of a coating formed in process R1 exhibits numerous cracks and crevices. A powdery appearance and a poor adhesion of this coating indicate that it was burned due to local spikes of the current density. The appearance of whitish spots in the image of a coating built in process R2 also indicates it burning in localized areas. Images of coatings formed in processes R3 and R4 show that they are relatively uniform and smooth. Undulations seen in these coatings along the grain boundary are relatively small.

Each SEM image in **Figure 3.5** display five sampling sites labeled 1 – 5 where the EDS analysis was performed. Due to similarity, the EDS plots are reported in **Figure 3.5** only for sites 1 and 2. Plots in **Figures 3.6 – 3.9** demonstrate the effect of anodizing regimes R1, R2, R3, and R4 on the content of aluminum, oxygen, sulfur, and zinc in an oxide coating.

The highest aluminum concentration of about 55 *wt. %* was found in coatings formed in processes R3 and R4. It is greater by about 10 *wt. %* than the aluminum content in coatings built in processes R1 and R2. Comparison of the aluminum content in coatings formed in processes R1, R2, R3, and R4, **Figure 3.6**, demonstrates that a difference between concentrations of aluminum in coatings created by different anodizing regimes exceeds variation of the aluminum level within a coating formed under the same anodizing conditions.

The lowest oxygen content of about 39 *wt. %*, was found in coatings formed in process R3 and R4. It is smaller by about 10 *wt. %* than the oxygen concentration in coatings built in processes R1 and R2. Comparison of oxygen concentration in coatings formed in processes R1, R2, R3, and R4, **Figure 3.7**, shows clearly that a difference between the oxygen level in coatings created by different anodizing regimes exceeds variation of the oxygen level within a coating built under the same anodizing conditions.

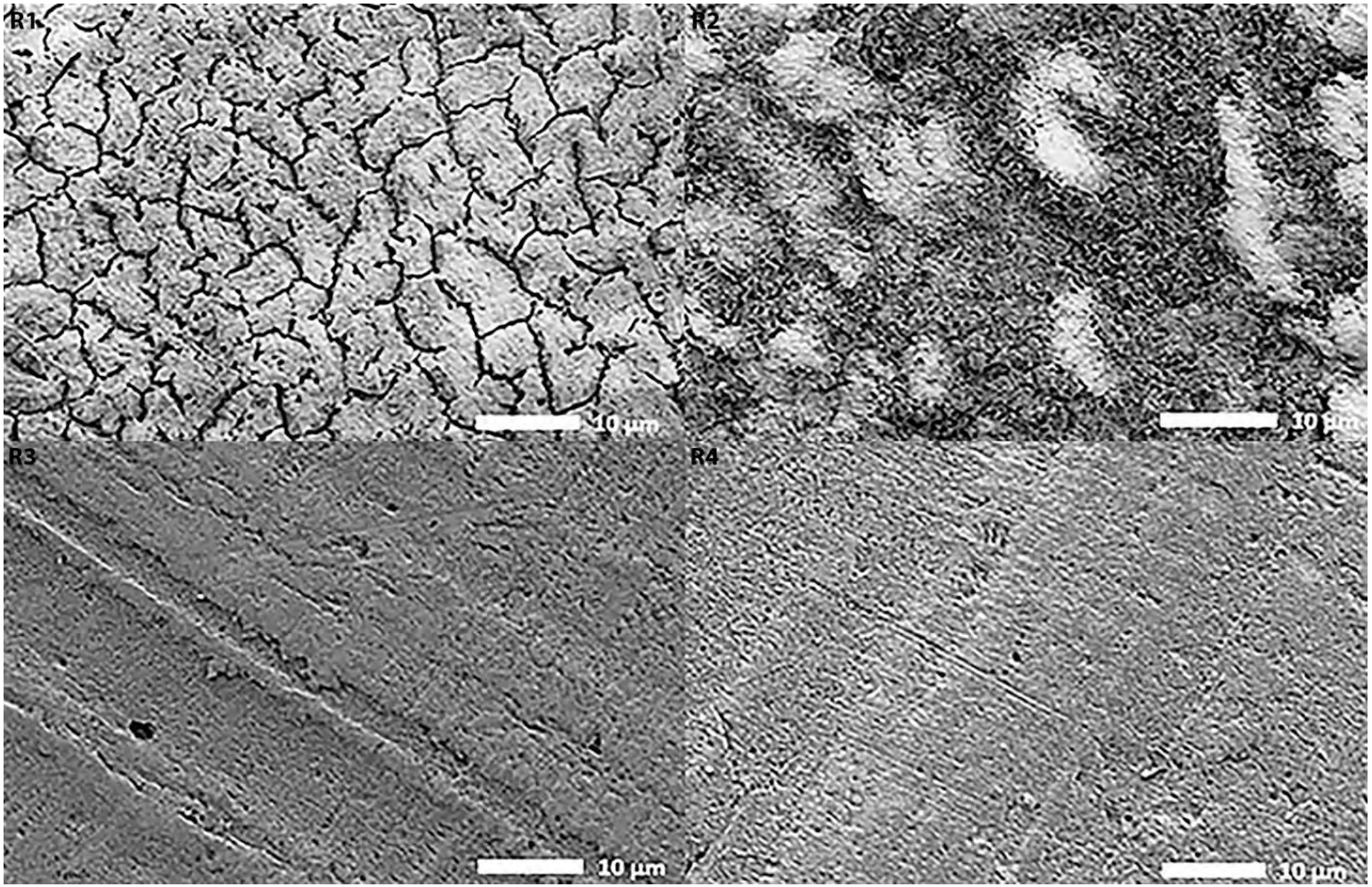

Figure 3.4 Microscopy views at 1700x were obtained for R1, R3 and R4. 1900x magnification was used for R2. The images obtained using 2.0 kV, under LED and the height of the specimen stage, WD, differed for each ramp, R1) 19.8 mm, R2) 25.1 mm, R3) 25.1 mm and R4) 24.7 mm.

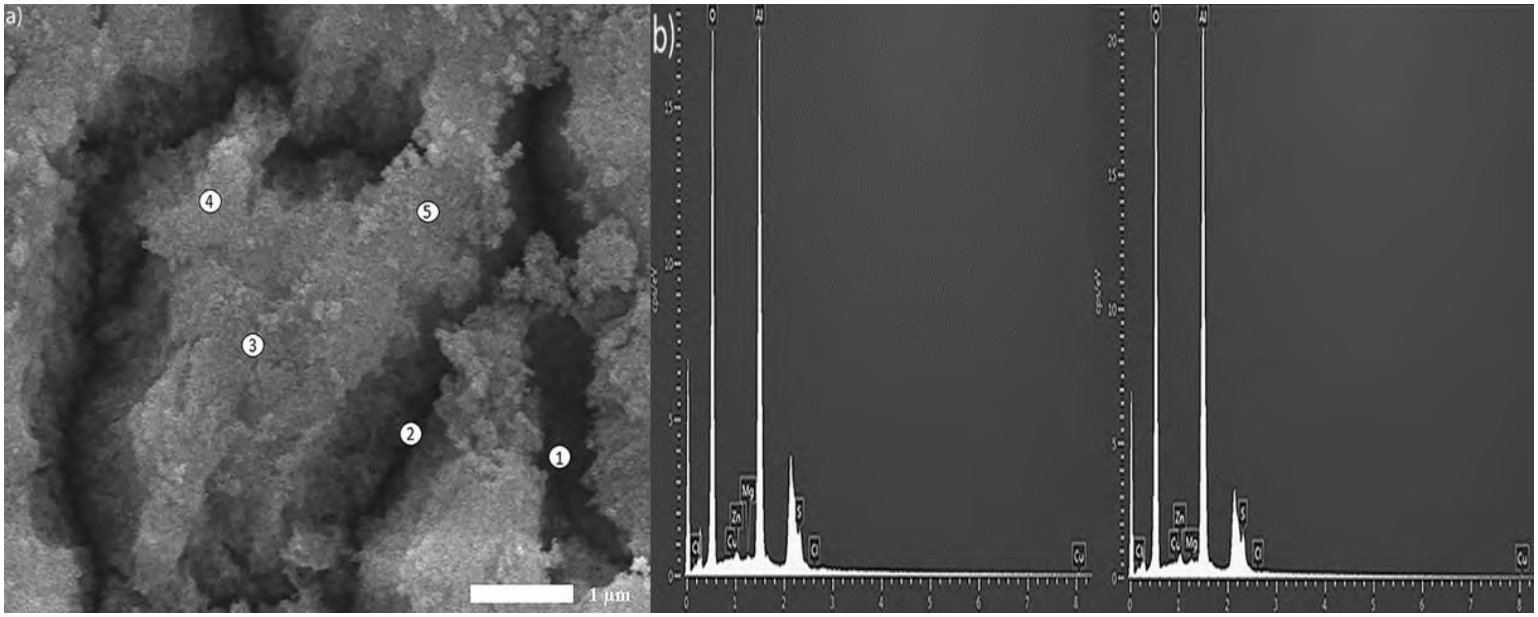

Figure 3.5 (a-b) Microscopy views and EDS results for process R1. Images at 19,000x were obtained using 5.0 kV, under LED and the height of the specimen stage, WD, was 10.0 mm. SEM images and EDS plots for sites 1 (left) and 2 (right), respectively, are presented in a, b.

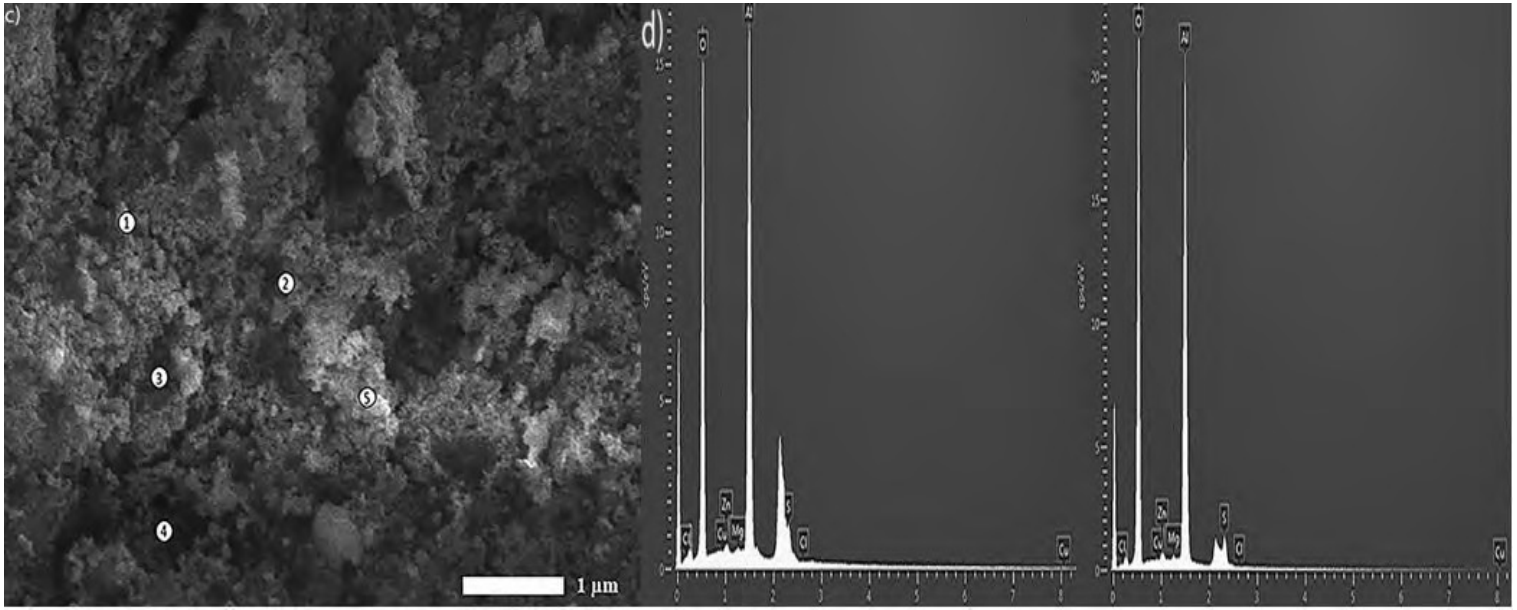

Figure 3.5 (c-d) Microscopy views and EDS results for process R2. Images at 19,000x were obtained using 5.0 kV, under LED and the height of the specimen stage, WD, was 10.0 mm. SEM images and EDS plots for sites 1 (left) and 2 (right), respectively, are presented in c, d.

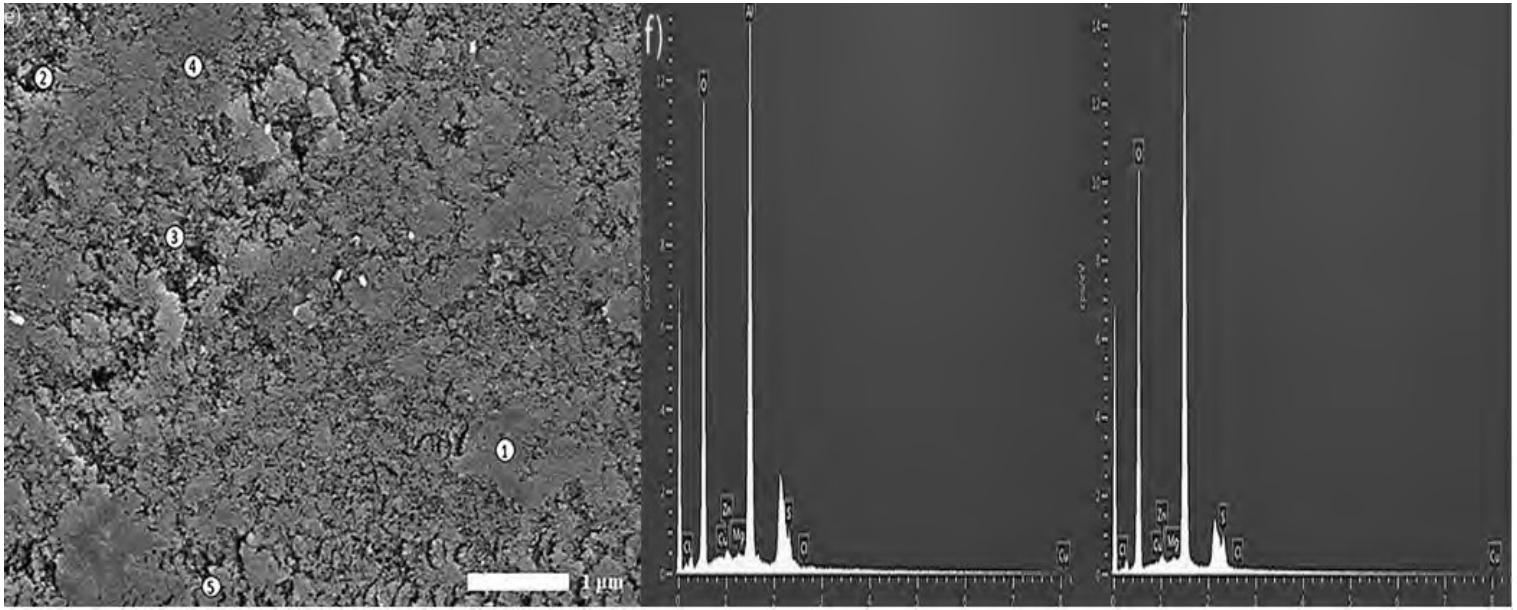

Figure 3.5 (e-f) Microscopy views and EDS results for process R3. Images at 19,000x were obtained using 5.0 kV, under LED and the height of the specimen stage, WD, was 10.0 mm. SEM images and EDS plots for sites 1 (left) and 2 (right), respectively, are presented in e, f.

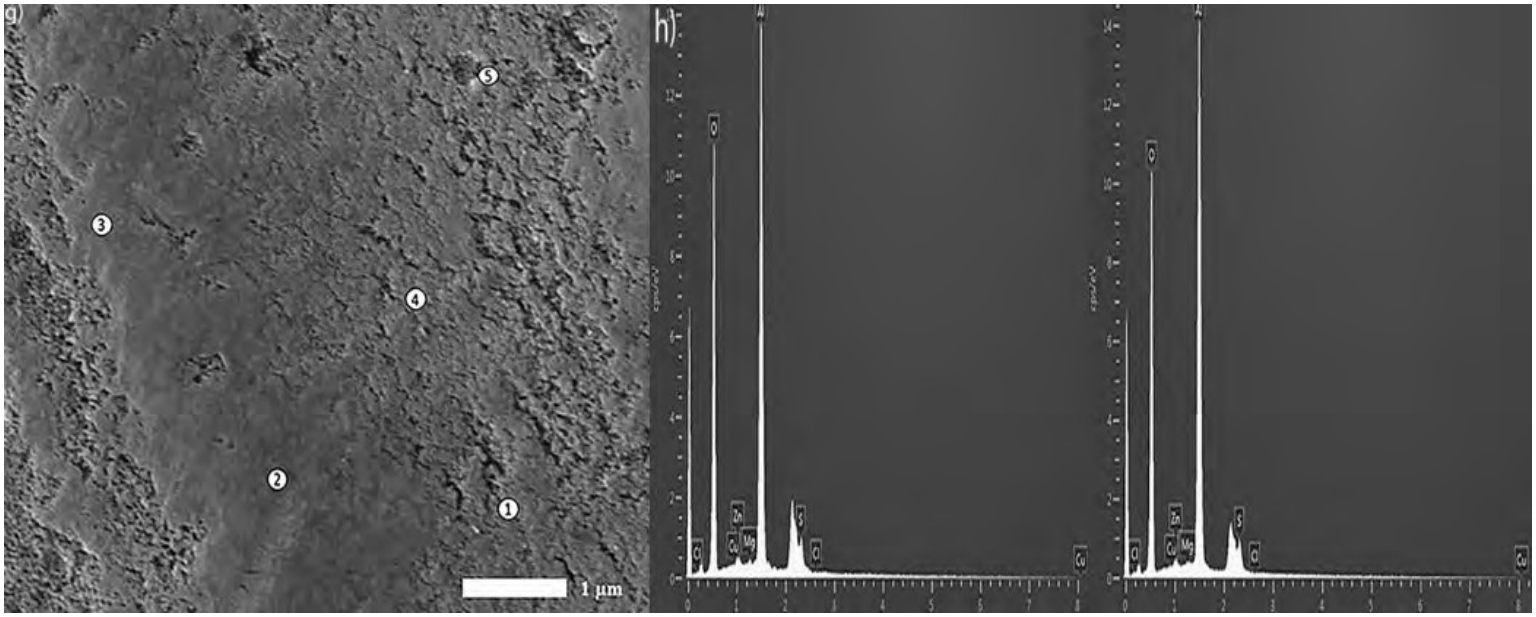

Figure 3.5 (g-h) Microscopy views and EDS results for process R4. Images at 19,000x were obtained using 5.0 kV, under LED and the height of the specimen stage, WD, was 10.0 mm. SEM images and EDS plots for sites 1 (left) and 2 (right), respectively, are presented in g, h.

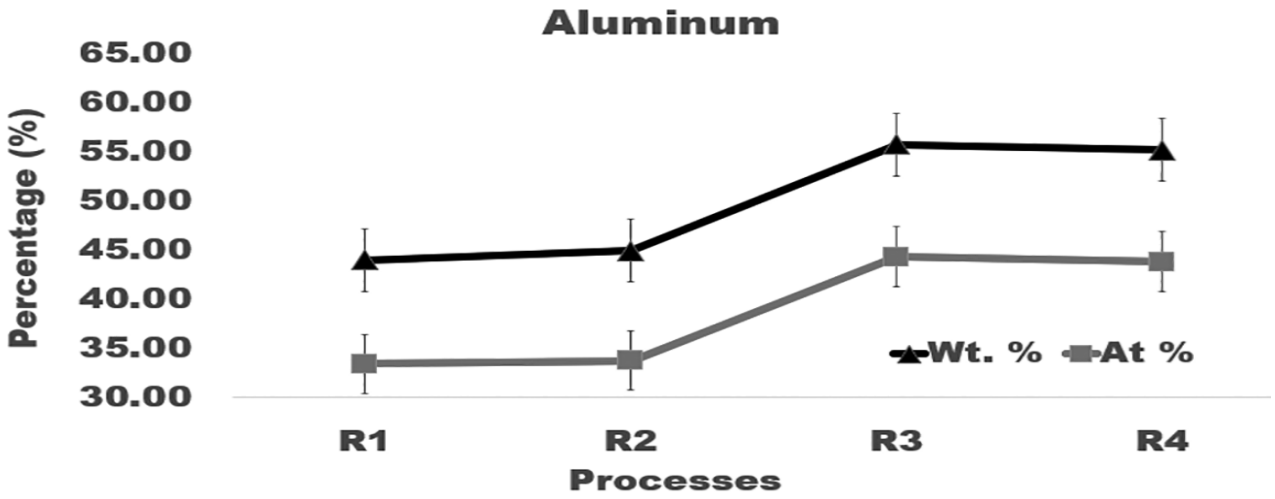

Figure 3.6 Graph of the amount of aluminum in surface layer formed after anodizing of aluminum using varying current density processes.

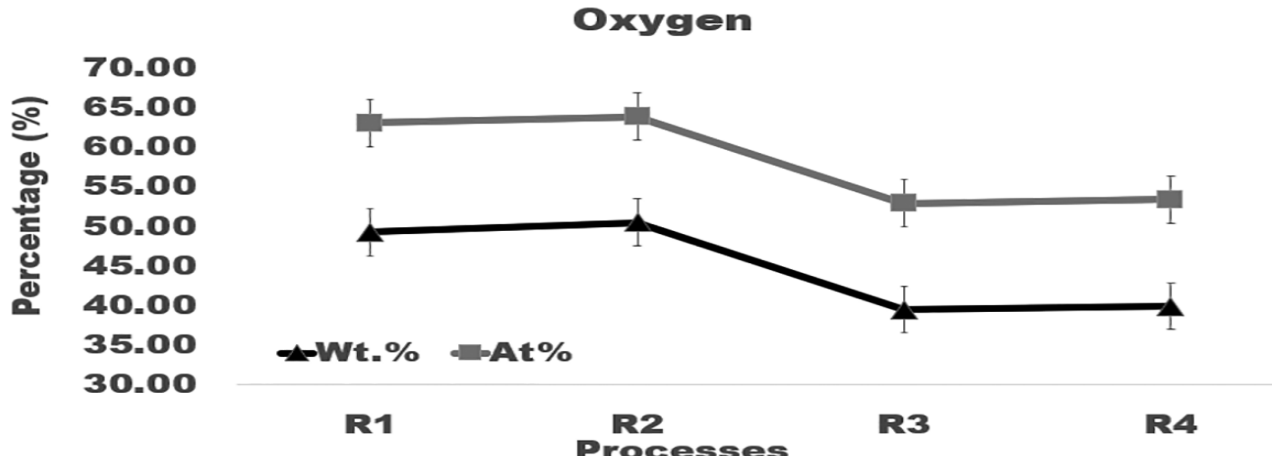

Figure 3.7 Graph of the amount of oxygen in surface layer formed after anodizing of aluminum using varying current density processes.

Coatings with the atomic Al/O ratio of 0.53 were formed in R1 and R2 processes, whereas this ratio was 0.83 in coatings built in R3 and R4 processes. The former is smaller than the Al/O stoichiometric ratio of 0.67 in Al_2O_3 oxide, whereas the latter is greater. A higher percentage of aluminum and a lower percentage of oxygen in coatings created in processes R3 and R4 made the coating surface smooth and solid-like as it is seen in SEM images in **Figures 3.3** and **3.4**. In contrast, a lower percentage of aluminum and a higher level of oxygen infused into coatings formed

in processes R1 and R2 caused them to burn and exhibit a powdery appearance as can be seen in SEM images in **Figures 3.4 and 3.5.**

Sulfur was adsorbed into the oxide layer with SO_4 ions penetrating from the electrolyte. The average sulfur level in coatings formed in processes R2, R3, and R4, **Figure 3.8**, is smaller by about 0.5 wt. % than in coatings built in process R1. Zinc diffused into an oxide layer from the alloy matrix. Compared to R1, the average content of zinc in samples anodized in processes R2, R3, and R4 is smaller by about 0.6 wt. %. However, comparison of the sulfur and zinc levels in coatings formed in processes R1, R2, R3, and R4, **Figures 3.8 and 3.9**, show that their differences fall within variations of the sulfur and zinc concentrations from location to location in a coating built under the same anodizing conditions.

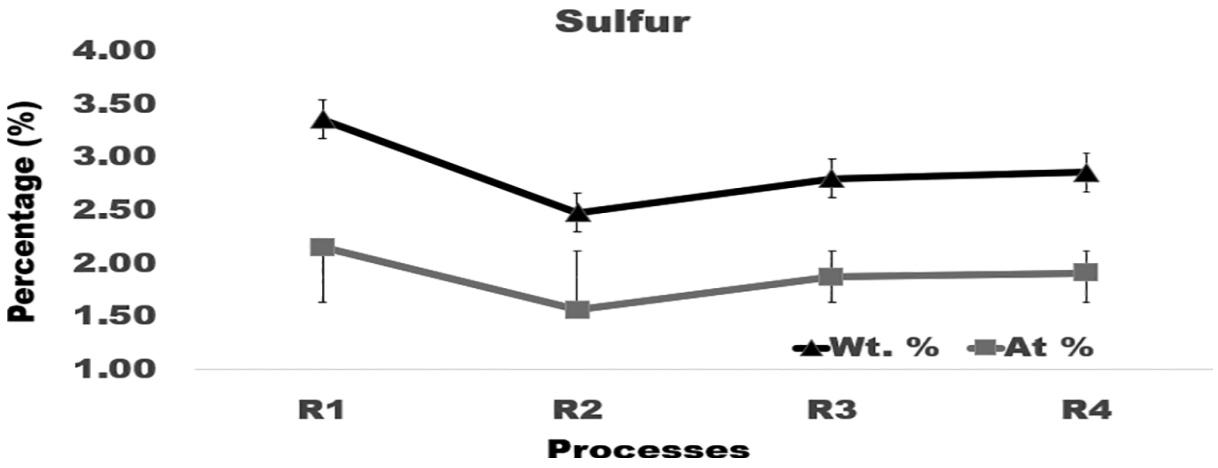

Figure 3.8 Graph of the amount of sulfur in surface layer formed after anodizing of aluminum using varying current density processes.

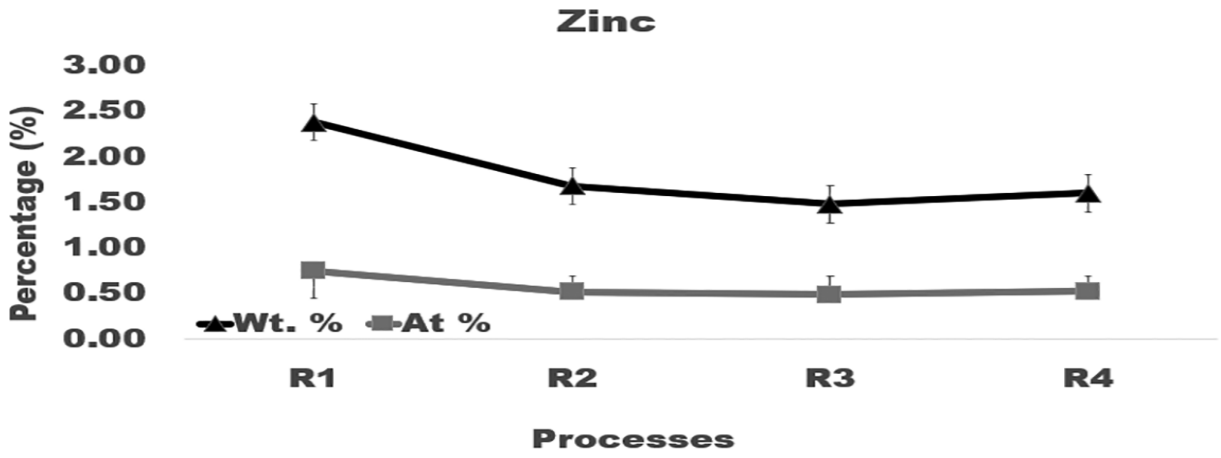

Figure 3.9 Graph of the amount of zinc in surface layer formed after anodizing of aluminum using varying current density processes.

High-magnification SEM images of the surface of anodic films developed in processes R1-R4 are presented in **Figure 3.10**. Values of the pore diameter, interpore distance and pore density are given in **Table 3.5**. Pore density was calculated using Equation (3.4) [94]:

$$N = \frac{2\,xx\,10^{\circ}}{\sqrt{3}(DD_{iiiiii}{}^{2})} \tag{3.4}$$

where N is the number of pores per unit area in μm^2 and D_{int} is the interpore distance in *nm*. As can be seen in **Table 3.5**, the observed dependence of the interpore distance and pore density on the applied initial voltage is consistent with Equation (3.5) [95] for the porosity of anodic aluminum oxides formed in sulfuric acid electrolyte:

$$DD_{iiiiii} = 12.1 + 1.99 \cdot U \qquad \text{for} \qquad 3 \leq U \leq 18 \tag{3.5}$$

where U is the applied voltage in V.

High-resolution SEM images (100,000x) in **Figure 3.10** demonstrate that processes R3 and R4 formed more intact coatings with fewer voids and crevices. They are not visible in SEM images presented in **Figures 3.4 and 3.5** which were taken at a lower magnification.

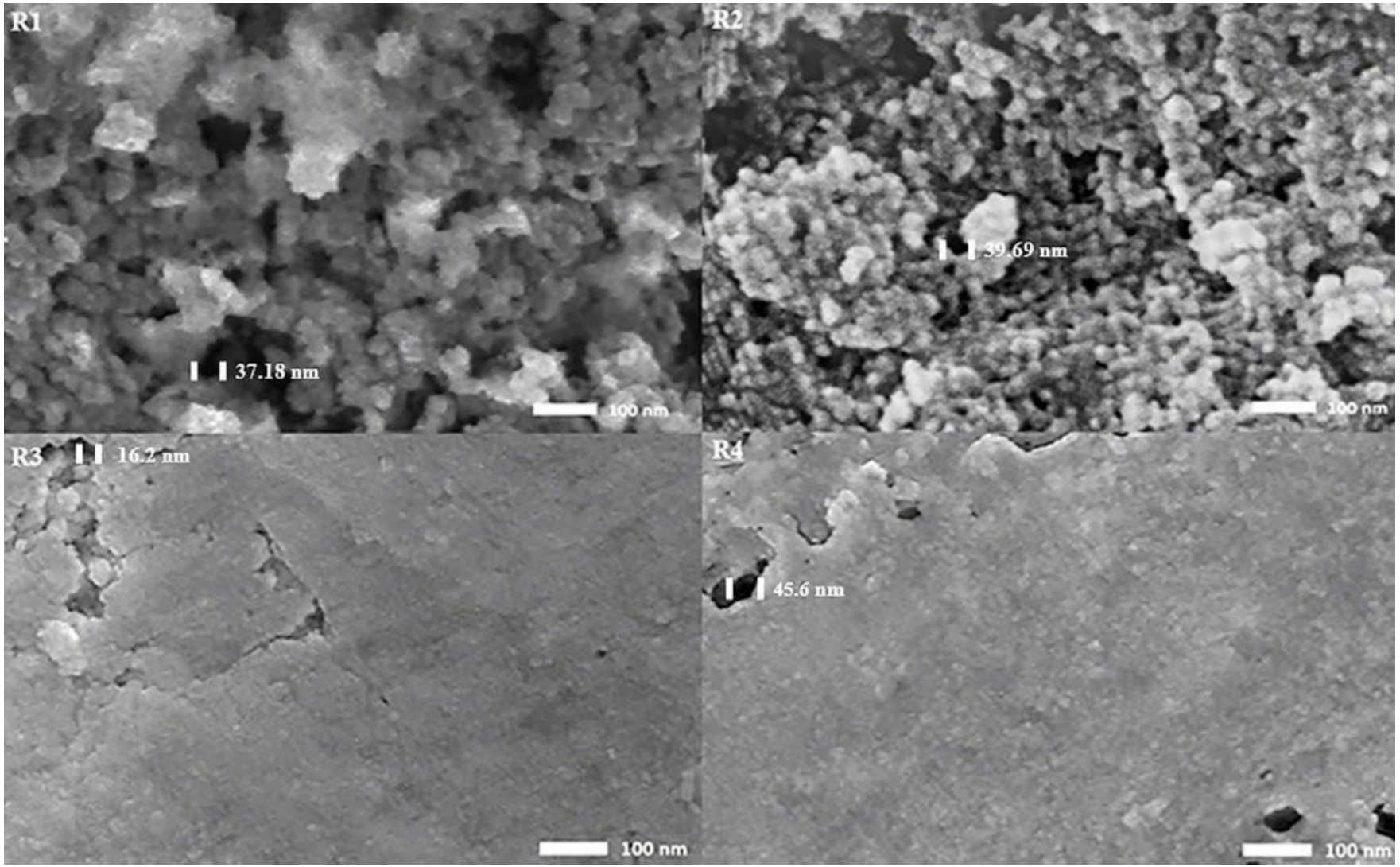

Figure 3.10 Microscopy views at 100,000x were obtained using 10.0 *kV*, under LED and the height of the specimen stage, WD, was 10.0 *mm* of processes R1, R2, R3, and R4. Pore diameter size and locations are identified for reference.

Whereas the depth of crevices in coatings built in R3 and R4 processes is 0.01 – 0.02 μm, crevices in coatings formed in R1 and R2 processes are 0.1-0.2 μm deep. Due to a smaller size of pores, coatings developed by processes R3 and R4 demonstrated higher hardness and resistance to abrasion. For R3 and R4, small pores can be seen in areas of delaminated coating in the upper left of **Figure 3.10**, whereas most of the coating has been fused together into a continuous film elsewhere. R1 and R2 exhibit a patchy coating which makes the pore structure visible. However, it did not increase their corrosion resistance that is mainly controlled by the ability to inhibit the penetration of corrosion elements to the substrate metal. The results of statistical analysis presented in **Table 3.7** demonstrate that a difference between the influence of anodizing processes in Group 1 and Group 2 on the pore diameter, interpore distance and pore density are statistically significant as $FF > \mathbb{F}_{0.05}$ and $0.05 > \mathbb{P}_{0.05}$.

Table 3.5 Pore Diameter, Interpore Distance, and Pore Density in Coatings Formed in Anodizing Processes R1, R2, R3, and R4. Statistical Analysis of Data Between Processes in Group 1 (R1 & R2) and Group 2 (R3 & R4) for the Overall Process is Listed Below

Processes	Pore Diameter (nm)	Interpore Distance (nm)	Pore Density ($1/\mu m^2$)		
R1	68.8 ± 29.8	38.8 ± 5.2	815.5 ± 251.2		
R2	62.8 ± 30.8	30.8 ± 5.7	1574.5 ± 855.5		
R3	24.8 ± 7.6	21.8 ± 4.1	2515.1 ± 907.4		
R4	43.4 ± 8.3	17.2 ± 3.8	4506.8 ± 1877.4		
Pore diameter					
Group	Count	Average	$P_{0.05}$	F	$F_{0.05}$
Group 1	21	65.9 ± 29.7	6.7E-05	20.0	4.1
Group 2	19	33.6 ± 11.1			
Interpore distance					
Group	Count	Average	$P_{0.05}$	F	$F_{0.05}$
Group 1	6	31.8 ± 26.7	0.0004	28.0	4.9
Group 2	6	20.4 ± 9.1			
Pore density					
Group	Count	Average	$P_{0.05}$	F	$F_{0.05}$
Group 1	6	1220 ± 388	1.1E-5	65.0	4.9
Group 2	6	2785 ± 274			

3.3.6 XRD patterns of anodized samples

Results of XRD measurements on samples anodized in processes R1, R2, R3, R4 and, for comparison, on samples of the untreated alloy AA7075-T6 are shown in **Figure 3.11 (a-b)**. Compared to the XRD data collected at an incident angle of 5^0 (regular regime), the contribution of signals from the substrate in the grazing XRD collected at an incident angle of 2^0 was reduced while the contribution of signals from the coating was enhanced. Grazing XRD was taken to provide more information about characteristics of the coating, with trying to reduce the effects of the base material. According to the instrument peak profiles, eight peaks in XRD patterns collected at an incident angle of 5^0 and four peaks collected at an incident angle of 2^0 corresponded to the aluminum face-centered-cubic (fcc) crystal structure.

However, specific diffraction peaks of aluminum oxides were not observed in both types of diffraction patterns collected on anodized samples. It indicates that amorphous aluminum oxides formed in the coating.

Compared to the untreated alloy, anodization changed the position and width of peaks in diffraction patterns. The lattice constant of the fcc structure of samples reported in **Figure 3.12(a)** was computed for both types of XRD measurements from Equation (3.6) [96]:

$$d_{hkl} = \frac{\omega\omega}{\sqrt{(h^2+kk^2+\ ll^2)}} \tag{3.6}$$

where d_{hkl} is the distance between the adjacent lattice planes in the fcc structure for the peak Bragg angle in *nm*, *a* is the lattice constant/parameter in *nm,* and *hkl* are the Miller indices for the lattice planes.

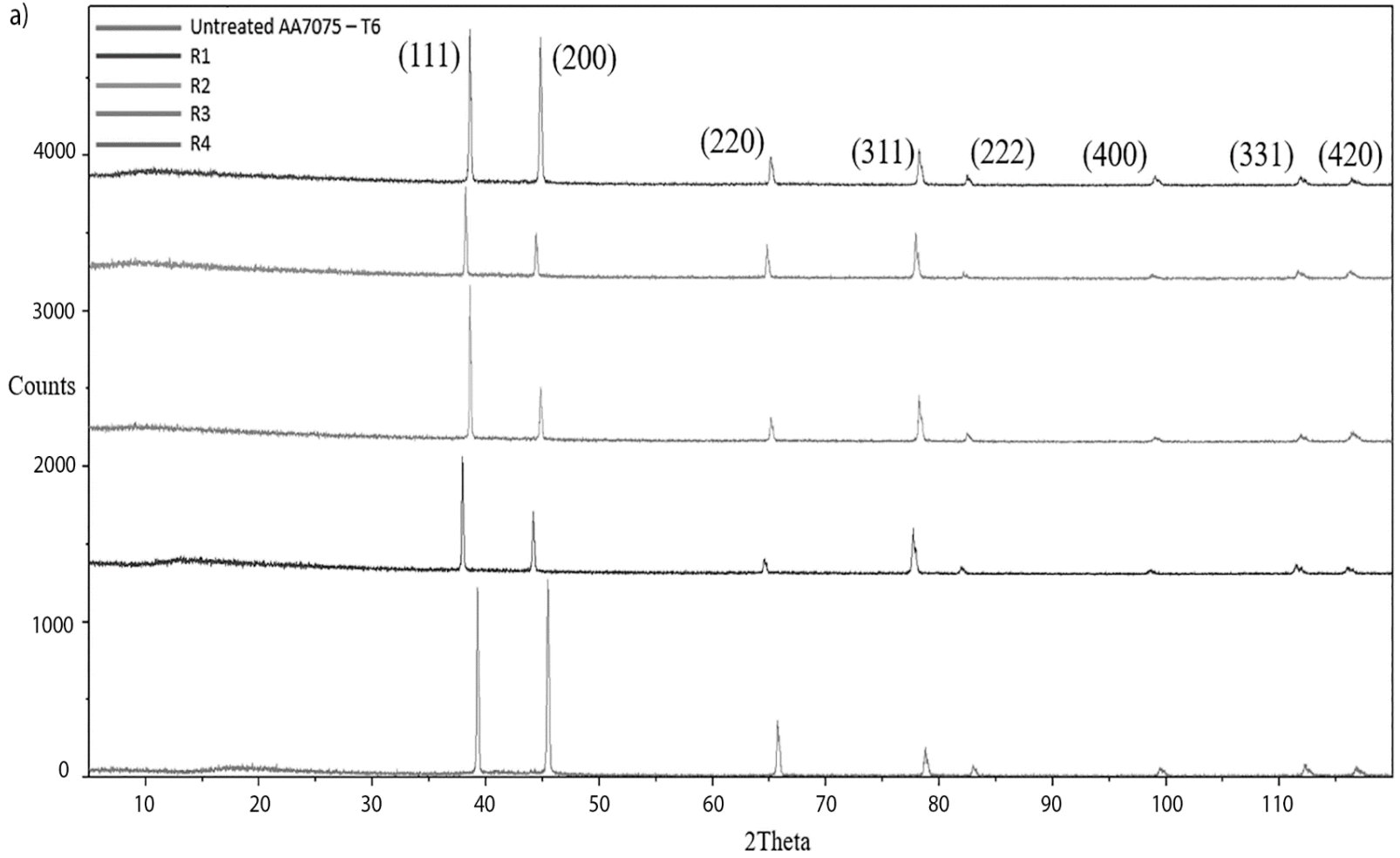

Figure 3.11a XRD measurements on samples of the untreated alloy AA7075-T6 and alloy samples anodized in processes R1, R2, R3, R4 collected at incident angles 5^0.

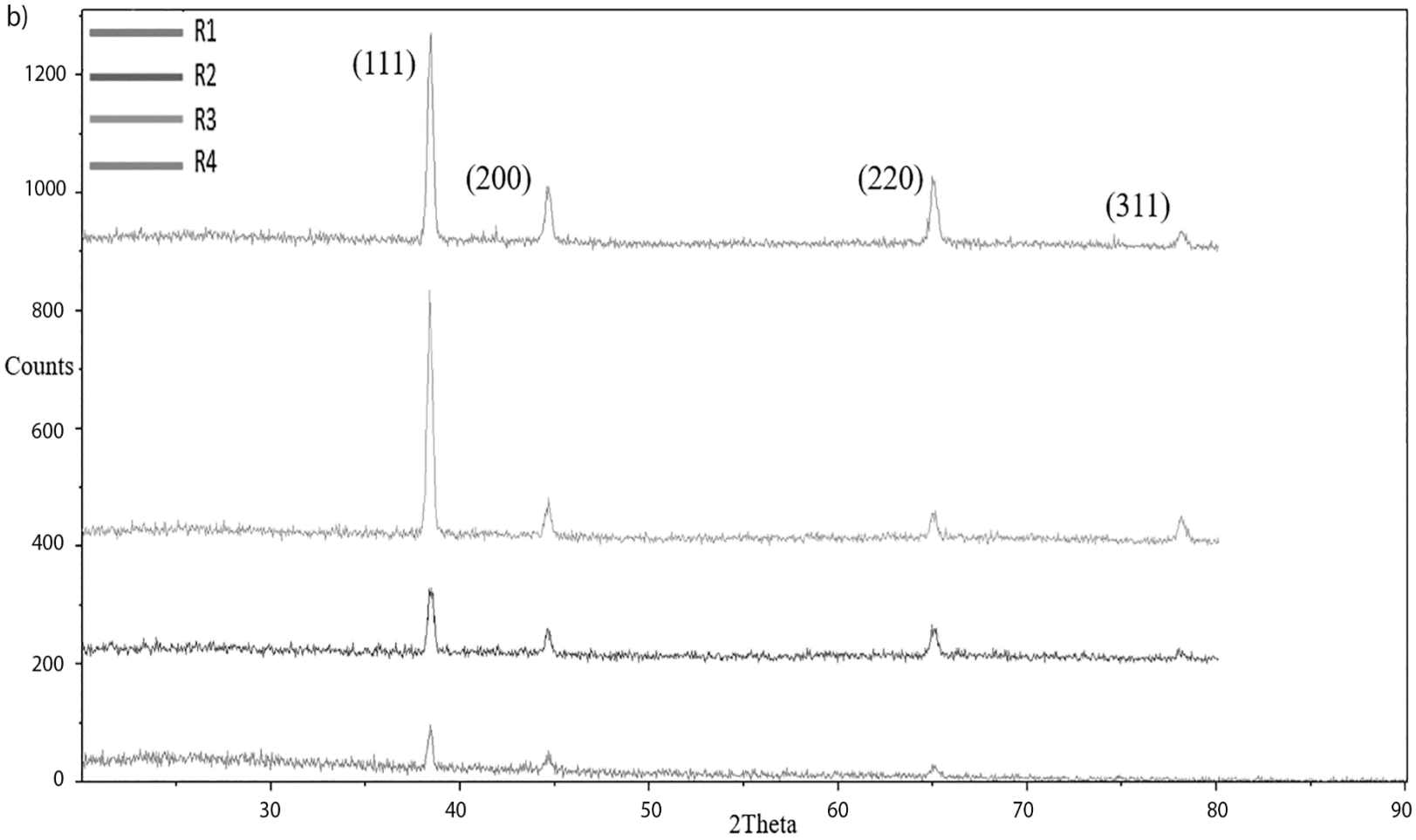

Figure 3.11b XRD measurements on samples anodized in processes R1, R2, R3, R4 collected at incident angles 2^0 using grazing technique.

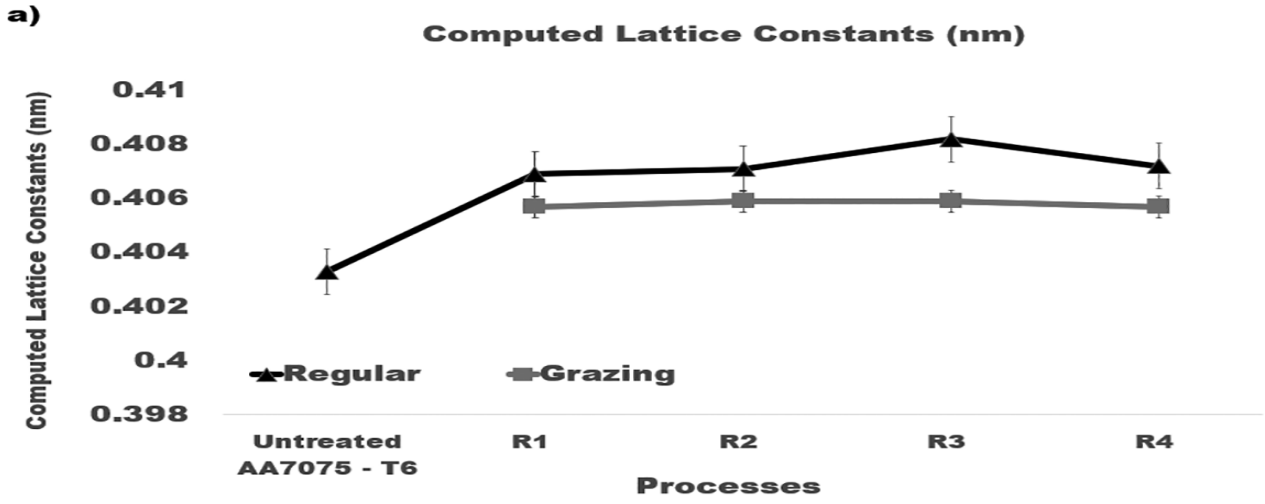

Figure 3.12a Computed lattice constants of the FCC structure of crystallites.

Plots in **Figure 3.12(a)** show that lattice constants of crystallites in anodized samples calculated from both types of XRD measurements are consistent and slightly larger than that of the untreated alloy.

The Scherrer equation, Equation (3.7) [96], was taken to compute the size of coherently scattering crystalline domains from the peak width

$$LL = \frac{KKKK}{\beta\beta_{\boldsymbol{h}kkll}cccccc(\theta\theta_{\boldsymbol{h}kkll})} \tag{3.7}$$

where L is the mean size of the crystalline domains in nm, $KK = 0.9$ is the shape factor, λ=0.15406 nm is the wavelength of the CuKα radiation, $\theta\theta_{\boldsymbol{h}kkll}$ is the peak Bragg angle in radians, $\beta\beta_{\boldsymbol{h}kkll}$ is the corrected value of the full width at half-maximum (FWHM) of the peak in radians, and hkl are the Miller indices of the crystallographic planes. The measured broadening, Equation (3.8) [96], of a peak was corrected by the data on the instrumental peak broadening as

$$\beta\beta_{\boldsymbol{h}kkll} = \left(\beta\beta^{2}_{mm,\boldsymbol{h}kkll} - \beta\beta^{2}_{iiiiiii,\boldsymbol{h}kkll}\right)^{1/2} \tag{3.8}$$

here $\beta_{m,hkl}(rad)$ is the measured FWHM, and $\beta_{inst,hkl}$ (rad) is the instrumental FWHM. Estimated values of $\beta_{inst,hkl}$ at the scanning regime utilized in the XRD measurements were kindly provided by Dr. Mirko Schoenitz (New Jersey Institute of Technology, New Jersey). They were calculated from data on the peaks in diffraction patterns of annealed spheroidal aluminum powders.

Plots in **Figure 3.12(b)** present data on the crystalline domain sizes for both types of XRD measurements. Results of these calculations were averaged over all peaks identified in the diffraction pattern and then averaged over three samples. As can be seen from **Figure 3.12(b)**, the size of crystalline domains in anodized samples computed from measurements at an incident angle of 5^0 (regular regime) is larger than in the untreated alloy. However, the size of crystalline domains in anodized samples found from data on the grazing XRD appear to be nearly twice as small. This outcome is related to the fact that the contribution of signals from the substrate is reduced while the contribution of signals from the coating is enhanced in the grazing XRD measurements. It is also noticeable in **Figure 3.12** those variations of the anodization regime do not seem to have an impact on the lattice constants and the size of crystalline domains.

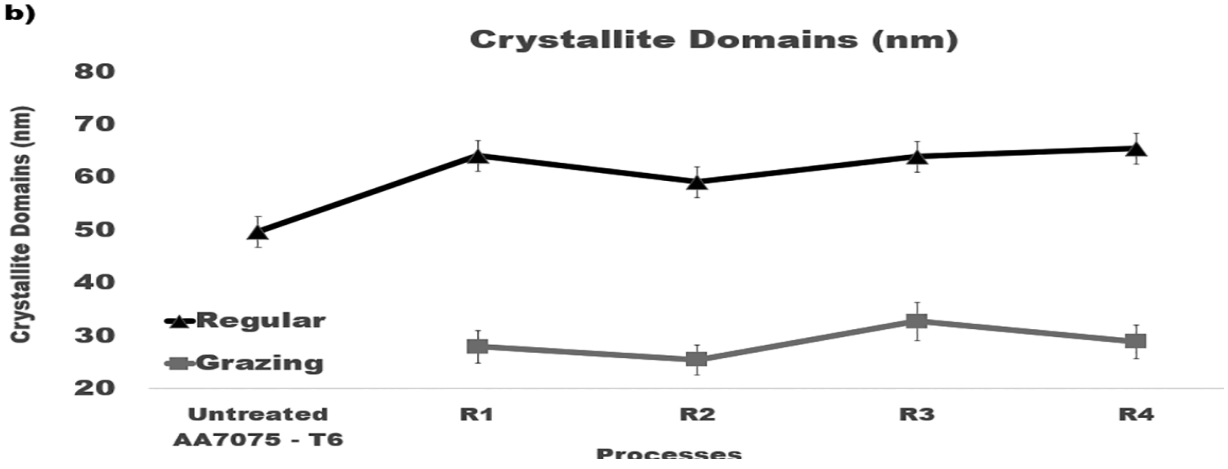

Figure 3.12(b) Computed sizes of crystalline domains.

3.3.7. Electric charge transferred during anodization

The amount of voltage applied in anodization controls the electric current and ultimately the coating formation. **Table 3.6** lists the anodizing current specified by **Table 3.2** and presents average data on measured initial and final voltage for each ramping step of processes R1, R2, R3, and R4.

These measurements were used to compute the work required to transfer the electric charge specified in **Table 3.2**. The work performed in each run is equal to the product of the applied voltage and the electric charge. Results are summarized in **Table 3.7**.

The amount of voltage applied to initiate the processes decreased with increasing the number of steps from R1 to R4 (**Table 3.6**). A larger amount of work was performed to build an oxide layer on the metal surface in processes R3 and R4 (**Table 3.7**). Compared to processes R1 and R2, processes R3 and R4 required a shorter period of applying an elevated voltage that suppressed the appearance of burning and processing defects in formed oxide layers. Processes R3 and R4 also provided a higher rate of the coating growth while requiring a smaller electric charge per one micrometer of the coating thickness (**Table 3.7**). The results of statistical analysis presented in **Table 3.7** demonstrate that a difference between the influence of anodizing processes in Group 1 and Group 2 on the initial and final voltage is statistically significant as $FF > \mathbb{FF}_{0.05}$ and $0.05 > \mathbb{PP}_{0.05}$.

Table 3.6 Data on the Applied Anodizing Current, Initial and Final Voltage and Transferred Electric Charge for Each Ramping Step of Processes R1, R2, R3, and R4. The Charge Value was Computed Based on Measurements of Anodizing Current. The Presented Values were Averaged Over Three Runs. Statistical Analysis of Data Between Processes in Group 1 (R1 & R2) and Group 2 (R3 & R4) for the Overall Process is Listed Below

Process R1			
Minutes	Amps	Initial voltage (V)	Final voltage (V)
30	22	12.3 ± 0.2	13.9 ± 0.3
Process R2			
Minutes	Amps	Initial Voltage (V)	Final Voltage (V)
5.00	13	7.5 ± 0.17	10.7 ± 0.12
5.00	17	11.8 ± 0.22	12.1 ± 0.21
20.00	25	12.6 ± 0.26	14.2 ± 0.17
Process R3			
Minutes	Amps	Initial Voltage (V)	Final Voltage (V)
2.50	8	4.6 ± 0.12	6 ± 0.21
2.50	13	8.5 ± 0.12	8.8 ± 0.2
2.50	17	10.6 ± 0.17	10.9 ± 0.12
2.50	21	11.7 ± 0.16	11.9 ± 0.13
20.00	25	12.1 ± 0.3	13.9 ± 0.18
Process R4			
Minutes	Amps	Initial Voltage (V)	Final Voltage (V)
1.25	6	3.7 ± 0.1	4.9 ± 0.16
1.25	8	5.7 ± 0.28	6.5 ± 0.12
1.25	10	7.1 ± 0.16	7.6 ± 0.16
1.25	13	8.2 ± 0.25	8.7 ± 0.12
1.25	17	9.4 ± 0.16	9.6 ± 0.21
1.25	19	10.3 ± 0.24	10.7 ± 0.12
1.25	21	10.9 ± 0.12	11.2 ± 0.1
1.25	23	11.4 ± 0.17	12.1 ± 0.17
20.00	25	12.7 ± 0.17	13.1 ± 0.17

Initial Voltage					
Group	Count	Average	$P_{0.05}$	F	$F_{0.05}$
Group 1	6	9.9 ± 2.6	0.0004	28.0	4.7
Group 2	6	4.2 ± 0.5			
Final Voltage					
Group	Count	Average	$P_{0.05}$	F	$F_{0.05}$
Group 1	6	14.0 ± 0.3	0.049	4.98	4.96
Group 2	6	13.5 ± 0.5			

Table 3.7 The Total Work (kJ) Required to Transfer Charge and Coating Formation Rate (μm/min) Averaged Over Three 30-min Runs of Anodizing Processes R1, R2, R3, and R4. Statistical Analysis of Data Between Processes in Group 1 (R1 & R2) and Group 2 (R3 & R4) for the Overall Process is Listed Below

Processes	Work (kJ)	Rate of coating formation (μm/min)			
R1	13511 ± 115	0.34			
R2	16358 ± 461	0.37			
R3	17014 ± 401	0.43			
R4	16506 ± 269	0.44			
Work					
Group	Count	Average	$P_{0.05}$	F	$F_{0.05}$
Group 1	6	14899 ± 1571	0.02	7.9	4.9
Group 2	6	16759 ± 382			
Coating Rate					
Group	Count	Average	$P_{0.05}$	F	$F_{0.05}$
Group 1	24	0.35 ± 0.02	6.70E-17	167	4.1
Group 2	24	0.44 ± 0.02			

As can be seen in **Tables 3.6 and 3.7**, basic characteristics of processes R3 and R4 are similar. Both demonstrated the layer growth rate was faster by 23.4% and 25.6%, respectively, than conventional process R1. It indicates that ramping the anodizing current density allows for more efficient coating formation later in the process. Interestingly, improvement of the mechanical properties of coatings formed in processes R2, R3, and R4 compared to R1 strongly correlates with increasing the amount of work implemented to form the oxide layer (**Table 3.7**). The results of statistical analysis presented in **Table 3.7** demonstrate that a difference between the influence of anodizing processes in Group 1 and Group 2 on the work and coating rate is statistically significant as $FF > \mathbb{F}_{0.05}$ and $0.05 > {}^{PP}_{0.05}$.

3.4 Conclusion

This study successfully demonstrated the overall advantages of multistep anodization of AA 7075-T6. Four anodizing regimes in a sulfuric acid bath were considered: a conventional R1 with a constant applied current and R2, R3, R4 with ramping of an applied current in two, four, and eight steps, respectively. Since oxides grew more slowly in initial lower-voltage steps of R3 and R4, the electrical resistance of the oxidized layer during this period was lower, which allowed heat to dissipate more readily and thereby suppressed formation of burns and defects. Compared to R1, multistep current ramping in R3 and R4 increased the overall growth rate of oxides by 23.4% and 25.6%, respectively and reduced by 8.4% the amount of a transferred electric charge per micrometer of the layer thickness. Like other conventional methods, process R1 was accompanied with spikes and burns at the beginning and did not provide a sufficient current at the end.

Processes R1 and R2 formed coatings with the atomic Al/O ratio of 0.53 smaller than 0.67 for oxide Al_2O_3, whereas R3 and R4 created coatings with the Al/O ratio of 0.83. A higher level of oxygen infused into coatings built in R1 and R2 caused them to burn and exhibit a powdery appearance, whereas processes R3 and R4 formed coatings with a smooth solid-like surface. Coatings created in processes R3 and R4 have substantially smaller number of crevices and their depth was about 0.01– 0.02 μm, whereas crevices in coatings formed in R1 and R2 were 0.1-0.2 μm deep. The pore size in the coatings formed in processes R1 and R2 was about 94% and 87% larger than in the coatings formed in processes R3, respectively. Compared to R1, process R4 created coatings that were 74.0% more resistant to abrasion, 14.6% harder and 25.4% thicker. As no specialized equipment is required, the presented multistep anodization is well suited for large-scale manufacturing.

CHAPTER 4

EFFECT OF CURRENT DENSITY RAMPING ON THE GROWTH RATE AND STRUCTURE OF AA2024-T3

4.1 Introduction

The use of 2000 series aluminum alloys in aerospace applications requires surface modifications to improve the corrosion resistance and mechanical properties of the product surface [1]. Surface modifications such as anodization, friction stir processing, and plasma electrolytic oxidation are needed to improve mechanical properties such as hardness, wear and corrosion resistance, and tribological properties [97-99]. Anodization is one of the most utilized methods to enhance the mechanical properties of aluminum alloys [88,100-102].

The presence of copper, a key alloying element, is used to form precipitates in the bulk by thermal ageing treatment [53,103] to enhance the alloy mechanical strength, fracture toughness, and fatigue properties [15-17]. Unfortunately, a difference between electrochemical potential of the aluminum alloy matrix and intermetallics promotes galvanic reactions that render the surface highly electro active [17,55,104]. These electrochemical differences lead to uneven growth and burning during anodization due to a spatially non-uniform distribution of electric current [11,15,17,55,75-77,104]. This condition is exacerbated if higher voltages and current densities are applied [11,15,17,55,75-77,104]. The presence of copper enhances local parasitic reactions that reduce faradaic efficiency of anodization and produce a flawed porous oxide layer [17,54,59-61].

The research on anodization of aluminum-copper alloys generally focuses on evaluating the influence of complex electrolyte baths, where addition of different acids such as malonic [100], carboxylic [105] fluorozirconic [106], citric [107], boric [108], and adipic [109] acids, are mixed with sulfuric acid to enhance the mechanical properties, morphology and reduce processing issues

[105-111]. Alternatively, industrial Types II and III anodization processes of aluminum alloys require the use of a sulfuric acid bath, and the application of electrolyte blends is limited [1,63,68]. Temperature and applied current/voltage are the basic process variables which can be manipulated in industry to improve the anodic coating [100]. However, variation of temperature is limited to the process of Type III, hard anodization. Therefore, the influence of applied current/voltage on the morphology and properties of anodic coatings are a subject of major interest for the industrial Type II anodizing process [1,63,68].

Anodizing current/potential influences the coating structure and properties as porosity and pore size are directly proportional to their magnitudes [112-114]. Anodization at high fixed voltages promote large current densities and high local heating at the beginning of the process that generates burning and reduces the film growth. This renders the coating properties unsuitable for a wide range of applications due to the presence of soft, porous coating and conical asperities [17,60,108]. The concept of ramping in anodization is to gradually raise the current density at the beginning of the process to prevent overpotential spikes. It has been recognized that changing the current density during the process has positive effects by increasing the heat dissipation and deoxygenation at the surface of the forming anodic coating [17,18,57,69,77,80,115]. Pulse anodization, an example of varying current density, [17] was observed to improve coating properties of AA 2024-T3, but the proposed process requires expensive equipment that is not readily available in an industrial setting.

Our previous work [104] revealed the advantages of multistep anodization of AA 7075 – T6, (5.6–6.1% Zn, 2.1–2.5% Mg, 1.2–1.6% Cu), in a standard Type II sulfuric acid electrolyte. The composition of AA2024 – T3, (4.3–4.5% Cu, 0.5–0.6% Mn, 1.3–1.5% Mg), is much different, and the difference in composition changes electrochemical behavior. It is well established that a difference in the size and mobility between copper and zinc ions changes their diffusion patterns

and alters the formation of an anodic coating on these alloys [11,55-57]. Zinc ions accumulate at the anodic oxide/aluminum interface, while copper ions are found throughout the anodic coating and on the specimen surface [11,56-57]. The presence of zinc and copper are known to create defects in the anodic coating that are detrimental for the coating morphology and properties. Since AA7075 – T6 and AA2024 – T3 require different anodizing processes [54,55,63-65,116,117], it is difficult to predict whether advantages of stepwise anodization observed for AA7075 – T6 would also benefit AA2024 – T3.

The present paper aims to study the influence of applying current density in multiple steps during the ramping stage on the morphology and performance properties of an anodic coating formed on AA 2024-T3 in a sulfuric acid bath. The results presented in this paper on the microstructure, growth rate and service performance of a coating formed on AA2024 – T3 show that raising the current density in five steps improves the overall process in terms of consistency, performance, and efficiency compared to a constant current anodization. We expect that a better understanding of the impact of multistep anodization on the coating properties of AA2024 – T3 taken together with data on AA7075 – T6 [104] would lay out the framework for the development of more efficient anodization processes on aluminum alloys.

4.2 Materials and Methods

4.2.1 Anodizing process

Anodization was performed in an electrochemical cell, **Figure 4.1**, in which voltage, amperage, and transferred charge are controlled with the module UPC 5000 RC-2 D P18/1000-24VN-C0, American Plating Power LLC, Florida. The UPC 5000 module was connected by a 50-mA shunt to the DC rectifier (American Plating Power LLC, Fort Myers, FL, USA) (1). The electrochemical cell consists of a polyvinylchloride tank, where the electrolyte temperature was controlled

externally by a two-output/input controller. Air agitation was performed utilizing constant low-pressure air (8). The cathodes (7) and the rack that suspended the anode (6) into the electrolyte were made of 6063 aluminum extruded bars. The cathode/anode area was kept at a 1:1 ratio measuring a total area of 0.097 m^2. The area of each load is 0.097 m^2 with 0.0485 m^2 being the rack area and 0.0485 m^2 being the part area. One cathode was mounted on each side of the tank for even distribution of an electric current.

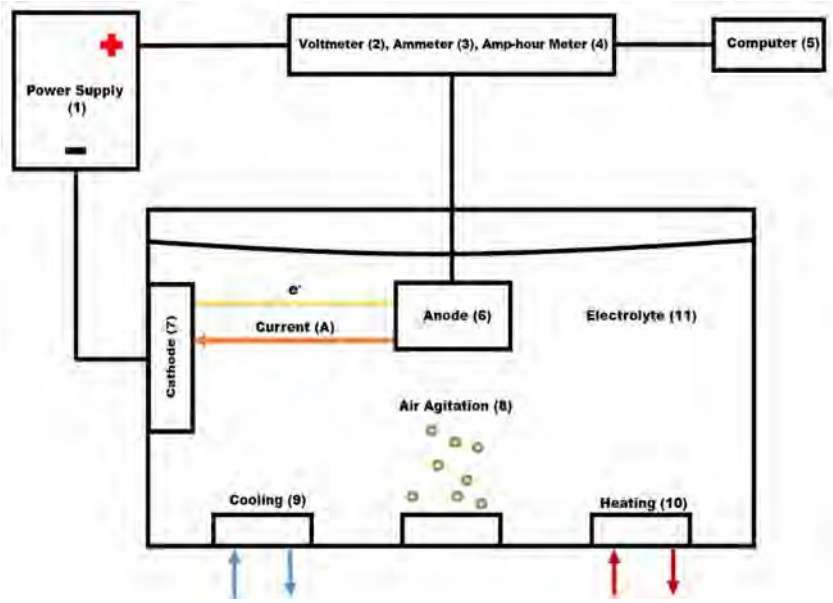

Figure 4.1 Anodizing system: 1) Power supply, 2) Voltmeter, 3) Ammeter, 4) Amp-Hour meter, 5) Computer, 6) Anode, 7) Cathode, 8) Air agitation, 9) Cooling system, 10) Heating system, 11) Electrolytic solution.

Experiments were carried out on specimens of AA2024 – T3 provided by Anacon 1st Choice, 425 W LA Cadena Dr., Riverside, CA, USA. The bulk chemical composition of this alloy given by the manufacturer is reported in the first row of **Table 4.1**. Scanning electron microscopy (SEM, JEOL JSM-7900F FE-SEM, Peabody, MA, USA) images show the presence of particles on the specimen surface. The Energy Dispersive X-Ray Spectroscopy, (EDS), (AZTEC, Oxford Instruments, Abingdon, UK) measurements taken from the specimen surface in locations with particles and without particles are also reported in **Table 4.1**. They demonstrate a substantial

difference between the local surface and bulk compositions in aluminum-copper alloys formed by micro-segregation and macro-segregation of alloying elements [1].

Table 4.1. Composition, wt. % of AA2024 – T3 Specimens Provided by Anacon 1st Choice, 425 W LA Cadena. Riverside, California. The First Row is the Bulk Composition Given by the Manufacturer. Secondary and Backscattered SEM Images at 30,000× Were Obtained Using 10 kV Under LED and the Height of the Specimen Stage, WD, of 10.0 mm to Observe the Surface Morphology and Measure the Local Composition with EDS

Elements (wt. %)	Al	Cu	Mg	Mn	Fe	Zn	Si	O
Manufacturer Data	92.8	4.8	1.4	0.6	0.2	0.1	0.1	-
EDS/Non - Particle Region	80.2 ± 7.4	5.7 ± 1.1	4.4 ± 0.9	1.1 ± 0.7	1.0 ± 0.8	0.7 ± 0.2	0.5 ± 0.1	6.4 ± 3.8
EDS/ Particle Region	65.2 ± 6.3	12.3 ± 4.7	6.2 ± 3.2	2.5 ± 1.6	2.4 ± 1.1	0.4 ± 0.1	0.4 ± 0.1	10.6 ± 4.6

All specimens were purchased as 10 cm x 10 cm x 0.16 cm squares with a hole of 0.64 cm diameter in the middle. Specimens were then further cut to 2.54 cm x 2.54 cm x 0.16 cm squares using a diamond blade and a portable bandsaw and then deburred to reduce sharp edges. Prior to chemical processing, all specimens, anodized and non-anodized, were cleaned with reagent-grade acetone before racking to remove glue, ink, and other surface impurities. Specimens were chemically processed using an alkaline cleaner, NaOH, for 10 mins, followed by a pickling process in a ferric sulfate/nitric acid bath for 5 mins. Specimens were rinsed by deionized (DI) water in between each chemical step. Untreated specimens went directly to the drying step after the cleaning process. After the preparation steps, specimens were anodized at room temperature, 20°C, for 30 mins. The electrolyte (11) consisted of sulfuric acid, 180 g/L. After anodization, the specimens were cleaned in DI water and air dried.

Five anodization processes listed in **Table 4.2** as Base, OS1, OS2, MS1 and MS2 were studied. “Base” is a conventional process with a constant electric current density; letters “OS” and “MS” mean, respectively, one-step and five-step ramping of an applied current density. Numbers “1” and “2” indicate, respectively, low, and medium current densities in ramping steps. Electric

current densities applied in these processes, **Table 4.2**, span a typical range of current densities utilized in industry.

Table 4.2. Anodizing Processes Designed for Experiments: A Conventional Base Process With a Constant Applied Current Density and Processes With Current Density Applied in One (OS1 and OS2) and Five (MS1 and MS2) Steps at Different Magnitudes During the Ramp Period. The Expected Values of Transferred Electric Charge Computed With the Use of Equation (4.1) and Equation (4.2)

Process	Mins	Current Density, A/m^2	Charge, C	Amperage, A
Base	30	180	30600	17
OS1	10	32	1800	3
	20	180	20400	17
OS2	10	111	6600	11
	20	180	20400	17
MS1	2	32	360	3
	2	40	480	4
	2	49	600	5
	2	57	600	5
	2	65	720	6
	20	180	20400	17
MS2	2	32	360	3
	2	64	720	6
	2	95	1080	9
	2	126	1440	12
	2	158	1800	15
	20	180	20400	17

Stepwise processes were designed to explore the influence of varying the number of steps and current density during the ramp on the coating morphology and properties. In the stepwise processes, (OS1, OS2, MS1 and MS2), ramping of an applied current density was conducted for 10 mins and the remaining 20-min period was carried out at a constant current (**Table 4.2**). The Base process, considered as the baseline for comparison, did not utilize a ramp. Anodic samples for testing were taken during three stages of the process. The samples were taken at 2-min intervals up to and including 10 mins, and at the end of the process, 30 mins. The Base process was included in the testing to study the effects of constant high current density in the same 10-min period.

The anodization process was designed to have the same electric charge passing through the system during the final stage of processing (20 mins) [104]. This task was implemented to show the impact of stepwise anodization during the ramp phase of processes listed in **Table 4.2**. An electric current was calculated with the use of Equation (4.1) and the expected values of electric charge for the designed processes of anodization were computed with the use of Equation (4.2):

$$A = X \cdot J, \tag{4.1}$$

where A is the current in amperes, X is the area in m^2, and J is the current density in A/m^2.

$$C = 60 \cdot A \cdot M, \tag{4.2}$$

where C is Coulomb = A·sec, A is in amperes and M is the period in minutes during which a certain current is applied, 60 is the conversion factor from minutes to seconds. Computed values of the anodizing electric current and the expected transferred electric charge for Base, OS1, OS2, MS1 and MS2 processes are summarized in **Table 4.2**.

4.2.2 Characterization techniques

i) The values of amperage, transferred electric charge, and actual voltage was measured using module UPC 5000 calibrated to NIST (+/- 0.1 V, 0.1 A). The presented voltage, amperage, and charge are values averaged over three repeated anodizing processes.

ii) Measurements of the coating thickness were conducted after air drying anodized specimens at temperature of 20.0 °C for 1 hour (± 5 mins). The coating thickness was measured using an Eddy current meter (Positector 6000, Deflesko, New York). Four thickness readings were taken for every anodized specimen and the presented result is averaged over three repeated

anodizing processes.

iii) Test panels for abrasion resistance were conditioned at 46.2 % relative humidity (RH) and 23.7 °C for 48 hours before testing. After conditioning, panels were weighed to the nearest ± 0.0001 g with an Ohaus digital balance (PA224, Ohaus, New Jersey). After weighing, panels were positioned on the Taber abraser and allowed to re- condition for 2 hours and then tested in the same conditions. Abrasion CS-17 wheels (CS-17, N Tonawanda, NY, USA) with a 1000 g load were used to abrade the surface of the specimen. Following the American Society for Testing and Materials (ASTM) D4060 standard, the Taber abraser was placed inside the SCCH high humidity chamber to condition the testing environment. Abrasion resistance was tested on two anodized specimens per process and the presented result is averaged over three repeated anodizing processes.

iv) Micro-hardness of anodized specimens was measured by a digital Vickers tester (Durascan 50, Struers, Ohio) with a 10 g load for 15 s. Micro-hardness readings were tested on two anodized specimens per process and the presented result is averaged over three repeated anodizing processes.

v) Acid dissolution tests of the 7.62 cm x 7.62 cm x 0.16 cm anodized specimens were carried out in accordance with ASTM B680 - 80 (2019) and ASTM B 137 – 95 (2014) specifications. A specimen was immersed for 15 ± 0.1 min in the stirred acid test solution maintained at a temperature of 38 ± 1 °C. Two tests were performed using the following solution: 35 ± 0.5 mL of Orthophosphoric acid of 85 mass %, 20 ± 0.5 g of Chromic acid anhydride (CrO3) and balance to 1000 ml of deionized water. Mass loss in mg/dm^2 was calculated using Equation (4.3) [118] in accordance with ASTM B680 – 80 (2019):

$$\text{Mass Loss, mg/dm}^2 = \frac{(W1-W2)}{A} \tag{4.3}$$

Total coating dissolved was calculated using Equation (4.4) [118] in accordance with both ASTM B 137 – 95 (2014) and ASTM B680 – 80 (2019):

$$\text{Coating Dissolved in Test, \%} = \frac{(W1-W2)}{(W_1-W_3)} \text{ x } 100 \qquad (4.4)$$

where, W_1 is the initial weight, mg, W_2 is the weight after testing, mg, W_3 is the weight after all coating was removed, mg, and A, is area in dm^2.

vi) Salt Spray (Fog) Testing is an accelerated corrosion test used to evaluate the corrosion resistance of metals and coated metals [119]. This test method, ASTM B117, has been approved for use by agencies of the U.S. Department of Defense and is widely used in the testing of anodic coatings [8,111,119-122]. Corrosion resistance testing by Salt Spray was conducted on 10 x 10 x 0.16 cm test panels that were anodized for 10 and 30 mins and sealed in Anodal MS-1 New (Reliant Aluminum Products, North Carolina) for 20 mins at 90 °C. One anodized specimen was tested for each anodizing process and the presented result is averaged over three repeated anodizing processes. The system used to create the corrosive environment was a Q-Fog Cyclic Corrosion Chamber (Q-Fog/SSP600, Q-LAB, Florida) in which specimens were exposed to a 5 wt. % NaCl fog for 336 hours, as per ASTM B117 [119]. The acceptance criterion is to form less than five corrosion pits for testing over 336- hour in a salt spray.

vii) Electrochemical impedance spectroscopy (EIS) is widely used to evaluate the corrosion resistance of an anodic coating on aluminum alloys [123-127]. EIS tests were conducted with a precision impedance analyzer (Agilent 4294A, Santa Clara, CA, USA). An experiment was carried out in a two-electrode arrangement using 1.0 cm^2 test area as the working electrode with the

reference electrode Ag/AgCl, +0.197 V vs. standard hydrogen electrode. Measurements were conducted in a 3.5 wt. % NaCl solution at room temperature over a frequency range from 40 to 60 MHz with the signal amplitude of 500 mV (rms). Tests were conducted on specimens anodized for 30 mins and the presented result is averaged over three repeated anodizing processes.

viii) Surface morphology of anodized and untreated specimens was analyzed by scanning electron microscopy (SEM, JEOL JSM-7900F FE-SEM, Peabody, MA, USA). Energy Dispersive X-Ray Spectroscopy (EDS) scanning of the alloying elements over the surface of anodized and untreated specimens was conducted using the program AZTEC, Oxford Instruments. Two methods of imaging were used to inspect the surface morphology. Secondary electron (SE) imaging, the default setting (LED), was used for inspection of the surface topography. Back-scattered electron (BSE) imaging, BED-C setting, was used to inspect the presence of voids and defects below the specimen surface [129]. All specimens that were anodized, were gold sputtered. Point and ID EDS measurements were analyzed using 10 kV while EDS mapping measurements were analyzed using 20 kV using a 45-min acquisition time. High-magnification SEM images at 100,000× were obtained using 10 kV under LED and the height of the specimen stage, WD, of 10.0 mm. BSE and SE large scale SEM images at 30,000x were obtained using 10 kV under LED for SE images and BED-C for BSE images, and the height of the specimen stage, WD, of 10 mm. Large- scale SEM images at 30,000× were obtained using 10 kV under LED and the height of the specimen stage, WD, of 10.0 mm. The non-anodized specimen was observed using secondary and backscattered imaging and with EDS mapping. Large scale SEM images at 30,000x were obtained using 20 kV under LED and the height of the specimen stage, WD, of 10.0 mm. A 20 kV beam was used for EDS mapping since mapping with a 10kV beam produced inaccurate data for alloying elements as it utilized *LLLL*-peaks for measuring their concentrations. Since the penetration of the 20 kV beam into the specimen was about 2 – 5μm, EDS mapping was carried out only on specimens anodized

for 30 mins of processing.

The National Institutes of Health (NIH) open-source image processing software ImageJ [130] was used to compute the porosity, pore diameter and the interpore distance in high-magnification SEM images (100,000×) (**Figure 4.3**). The processing of an original SEM image combined a sequence of standard ImageJ procedures: Set the image scale in pixels/μm based on the scale bar equal to 100 nm; convert image type to 8-bit grayscale; reduce noise and enhance image contrast by using histogram equalization; use flat-field-correction and subtract background to correct for uneven illumination; use a locally adaptive thresholding technique to detect the boundaries between different regions in the image; select a region of interest (ROI) to automatically compute the pore size.

ix) Equation (4.5) was used to calculate the efficiency of building an anodic coating, η_{ox}. The anodic efficacy can be described as the ratio of the measured coating mass to the theoretical coating mass computed from the charge transferred during anodization [115]:

$$\eta_{ox} = \frac{m_2 - m_3}{\eta_{charge^*} \frac{M_{ox} * Q(t)}{n_{ox} * F}} \tag{4.5}$$

where m_2 and m_3 are respectively the specimen mass measured after anodization, g/dm^2, and after removal of the anodic coating, g/dm^2; η_{charge} is the charge efficiency; M_{ox} is the molar mass of Al_2O_3 equal to 102 g/mol; Q(t) the cumulative charge transferred per dm^2; n_{ox} is the number of electrons associated with the oxide formation [131]; and F is the Faraday's constant (96,500 C/mol). Because η_{charge} is usually close to 1.0 for small anodizing systems, this value was used in calculations.

x) X-ray diffraction (XRD) measurements were conducted on EMPYREAN, Malvern

PANalytical, UK at an incident angle 2° in parallel beam geometry with grazing technique, to reduce the signal from the substrate and enhance the signal from the coating, with Rigaku Optima IV diffractometer, Wilmington, MA, USA, equipped with CuKα radiation. Two scans at the operating parameters of 40 mA, 45 kV and 0.5° min^{-1} scanning speed were conducted for every anodized specimen and the presented result is averaged over three repeated anodizing processes. The instrumental broadening of XRD peaks were measured using the National Institute of Standards and Technology Standard (NIST) Reference Material® 1976c consisted of a sintered alumina disc [132].

xi) The reported percentage difference between two measured values in all tests, val_1 and val_2 was calculated using Equation (4.6):

$$\text{Difference (\%)} = 100 \text{ x } \frac{\text{ABS}(\text{Val1} - \text{Val2})}{(\text{Val}_1 + \text{Val}_2)/2} \tag{4.6}$$

xii) In the statistical analysis of data, measurements of the anodic coating characteristics were arranged in comparison groups: Group 1 (Base, OS1, OS2) and Group 2 (MS1, MS2) as well as in two groups to compare the outcome of processing for 10 mins and 30 mins. The F-test of equality of variances was used to determine whether both populations have the same variance [92]. The null hypothesis of an experiment states that a difference between measurements within a particular group compared with the other group appeared by chance. The alternative hypothesis is that this difference was influenced by differences in anodizing processes. The following three-step procedure performed with Analysis of Variance (ANOVA) Microsoft Excel was used for testing the null hypothesis: (1) compute the mean and variance of measurements for each of two groups, (2) compute the overall mean and variance for both groups taken together, and (3) compute the F

factor as the ratio between the mean variability of measurements within one group and the mean variability of data within both groups taken together. The value of the F factor will be large only if the variability between the groups is large compared to the variability within both groups taken together. The number of measurements in each group, the total number of measurements and the chosen alpha level, α, yield the confidence level $100 \cdot (1 - \alpha)\%$ [92]. There are two criteria for rejecting or accepting the null hypothesis. One is to calculate F_α that is a function of α: F should exceed F_α for the null hypothesis to be rejected. The other is to calculate the P_α −value that is a function of α for rejecting, $\alpha > P_\alpha$, or accepting, $\alpha \leq P_\alpha$, the null hypothesis. The reported results of F-tests were conducted for $\alpha = 0.05$ corresponding to the confidence level of 95%.

4.3 Results and Discussion

4.3.1 Coating performance characteristics

4.3.1.1 Coating thickness. Anodic coating thickness was measured using an Eddy current meter. **Table 4.3** reports coating thickness measurements (μm) obtained from processes Base, OS1, OS2, MS1, and MS2.

Table 4.3 Thickness (μm) of Coatings Formed in Base, OS1, OS2, MS1, and MS2 Processes was Measured Using an Eddy Current Meter. Anodic Samples for Testing were Taken During 3 Stages of the Process. The Samples were Taken at 2-min Intervals up to and Including 10 mins, and at the End of the Process, 30 mins. Statistical Analysis of Data Between Processes in Group 1 (Base, OS1, OS2) and Group 2 (MS1, MS2) for the Overall Process is Listed Below

Thickness (μm)							
Process Time, Min	**0 to 2**	**2 to 4**	**4 to 6**	**6 to 8**	**8 to 10**	**10 to 30**	**Overall**
Base	1.0 ± 0.3	1.4 ± 0.4	2.0 ± 0.4	3.0 ± 0.5	4.1 ± 0.4	6.8 ± 0.5	10.9 ± 0.7
OS1	0.4 ± 0.2	0.7 ± 0.3	1.1 ± 0.2	1.3 ± 0.3	1.6 ± 0.3	7.7 ± 0.4	9.3 ± 0.5
OS2	0.8 ± 0.3	1.2 ± 0.4	2.0 ± 0.4	2.2 ± 0.4	2.7 ± 0.3	8.0 ± 0.3	10.7 ± 0.7
MS1	0.3 ± 0.1	0.8 ± 0.3	1.5 ± 0.4	1.7 ± 0.4	2.0 ± 0.3	10.2 ± 0.4	12.2 ± 0.4
MS2	0.2 ± 0.1	1.1 ± 0.3	1.5 ± 0.4	2.2 ± 0.3	2.9 ± 0.4	9.7 ± 0.4	12.6 ± 0.5
Groups	Count	Average	$P_{0.05}$	F	$F_{0.05}$		
Group 1	36	10.3 ± 0.9	2.7×10^{-14}	100.8	4.2		
Group 2	24	12.4 ± 0.5					

Three time periods were chosen to describe the effect of applying multistepped current density vs constant current density on coating build up. The first period, the 10-min ramp, was measured in five, 2-min increments. The current densities used were different for each ramp process and are referenced in **Table 4.2**. The final stage of anodization was carried out for 20 mins at the current density stage of 180 A/m^2 for every process. The rightmost column in **Table 4.3** presents the overall coating thickness.

Multistepped processes, MS1 and MS2, formed thicker coatings than coatings produced in the Base process. Noteworthy, the coating thickness formed during the final current density

stage for processes, MS1 & MS2, was greater than over the entire OS1 process. The total thickness formed by Base process, 10.9 μm, processes MS1 and MS2 produced 93.6% and 89.0% of that coating thickness in 33% less time. All processes utilizing ramping outperformed the Base process in coating thickness formed during the final 20-min stage of processing. The results of statistical analysis presented in **Table 4.3** demonstrate that a difference between the influence of anodizing processes in Group 1 and Group 2 on the coating thickness is statistically significant as $FF > \mathbb{F}_{0.05}$ and $0.05 > \mathbb{P}_{0.05}$.

4.3.1.2 Abrasion resistance of anodic coating

Abrasion resistance was characterized by calculating the weight of the anodic coating removed following 1,000 abrasive cycles. **Table 4.4** lists the weight loss measurements for each specimen.

The presented results demonstrate that processes utilizing lower applied voltage, OS1, MS1 and MS2 provided a higher abrasion resistance by 12.1%, 38.2%, and 31.2%, respectively, when compared to the Base process. The results of statistical analysis presented in **Table 4.4** demonstrate that a difference between the influence of anodizing processes in Group 1 and Group 2 on the abrasion resistance is statistically significant as $F > F_{0.05}$ and $0.05 > P_{0.05}$. Plots in **Figure 4.2** demonstrate as the final voltage decreased; the abrasion resistance increased.

High-magnification SEM images (100,000x) of anodic coatings posted in **Figure 4.3** demonstrate a correlation between the increased abrasion resistance and the improvement of the coating morphology. Specifically, these large regions of cracking and pitting formed during anodization are more prominent in the coatings produced by Base and OS2 processes. Coatings subjected to higher voltages, developed areas with surface asperities and porosity. Areas that exhibit these features will become loose upon abrasion.

Table 4.4 Testing Results of Abrasion Resistance, Microhardness, Acid Dissolution and Weight Loss Per Micron of Specimens Anodized in Base, OS1, OS2, MS1, MS2 Processes. Statistical Analysis of Data Between Processes in Group 1 (Base, OS1, OS2) and Group 2 (MS1, MS2) for the Overall Process is Listed Below

Process	Wt. loss (mg) in abrasion tests	Microhardness (MPa)	Wt. loss per coating area (mg/dm^2)	% Loss of total coating	Wt. loss per micron (mg/μm)
Base	39.3 ± 4.1	1282.3 ± 57.6	181.0 ± 11.3	99.6	19.3
OS1	34.8 ± 3.8	1147.4 ± 38.3	169.0 ± 4.9	99.2	21.3
OS2	39.2 ± 4.4	1369. 3 ± 20.8	186.0 ± 5.7	99.9	20.2
MS1	26.7 ± 2.0	1398.7 ± 28.1	205.0 ± 8.8	95.2	20.5
MS2	28.7 ± 3.3	1455.1 ± 23.5	227.0 ± 5.2	96.2	21.7

Abrasion					
Groups	Count	Average	$P_{0.05}$	F	$F_{0.05}$
Group 1	18	37.8 ± 4.7	4.3×10^{-7}	42.8	4.2
Group 2	12	27.7 ± 3.0			

Microhardness					
Groups	Count	Average	$P_{0.05}$	F	$F_{0.05}$
Group 1	18	1266.4 ± 103	2.1×10^{-5}	26.1	4.2
Group 2	12	1426.9 ± 40			

Acid Dissolution					
Groups	Count	Average	$P_{0.05}$	F	$F_{0.05}$
Group 1	18	178.7 ± 11.0	6.4×10^{-9}	67.2	4.2
Group 2	12	216.0 ± 13.8			

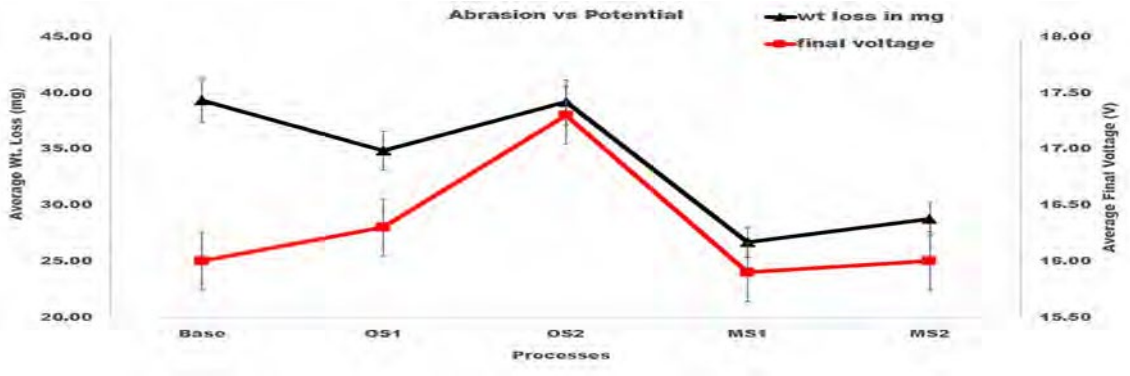

Figure 4.2 Average wt. loss, mg, versus average final voltage, V. The triangle shape represents the average wt. loss and the square, the average final voltage. A reduction in wt. loss with lower final voltage is noticed in MS1 and MS2.

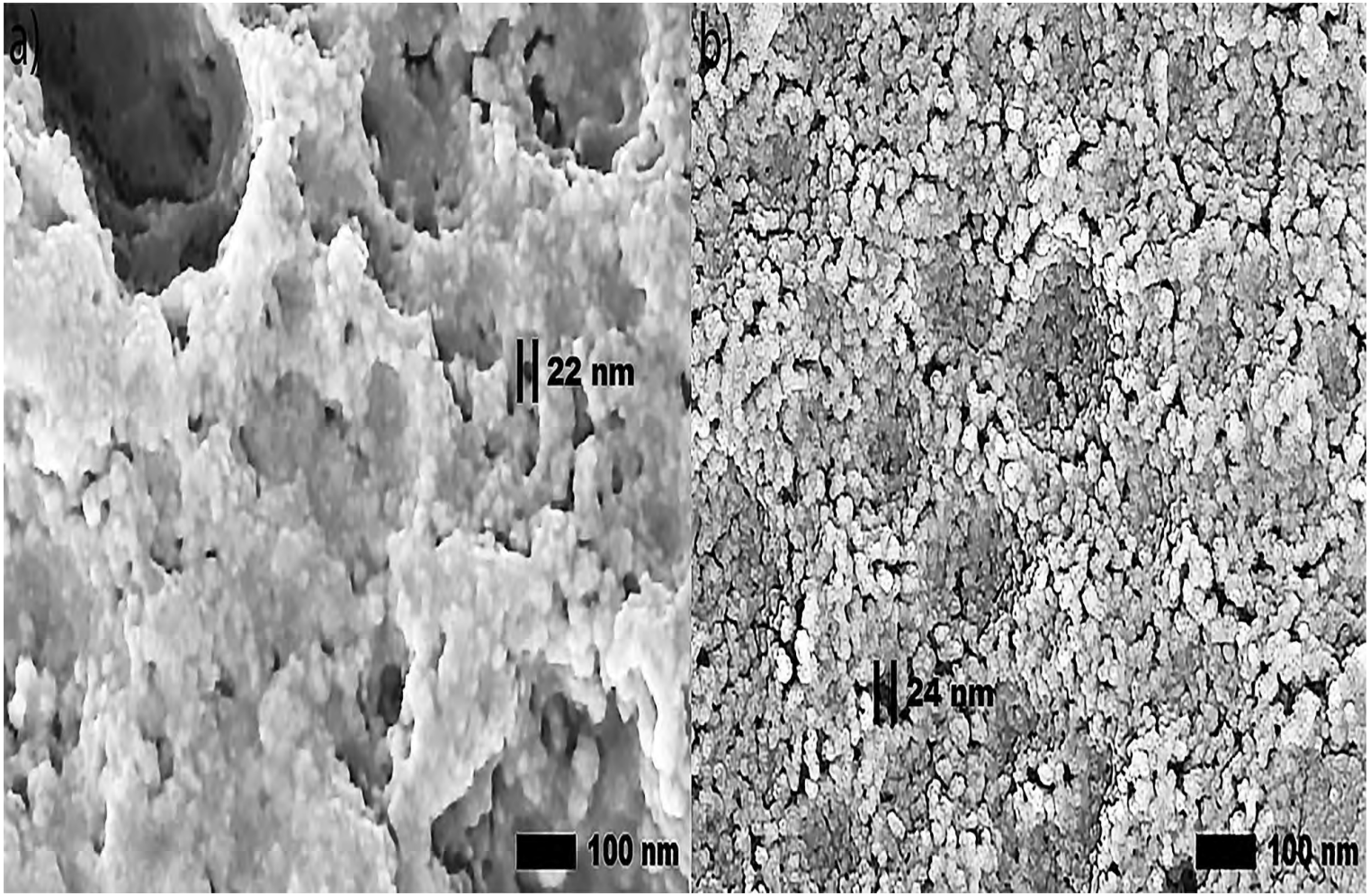

Figure 4.3(a-b) Secondary SEM images (100,000×) of the surface morphology reveal circular pores created in the anodization process, respectively, in the Base process. Left images show specimens anodized for 10 mins and right images show specimens anodized for 30 mins. Shown pore sizes were computed with ImageJ [130].

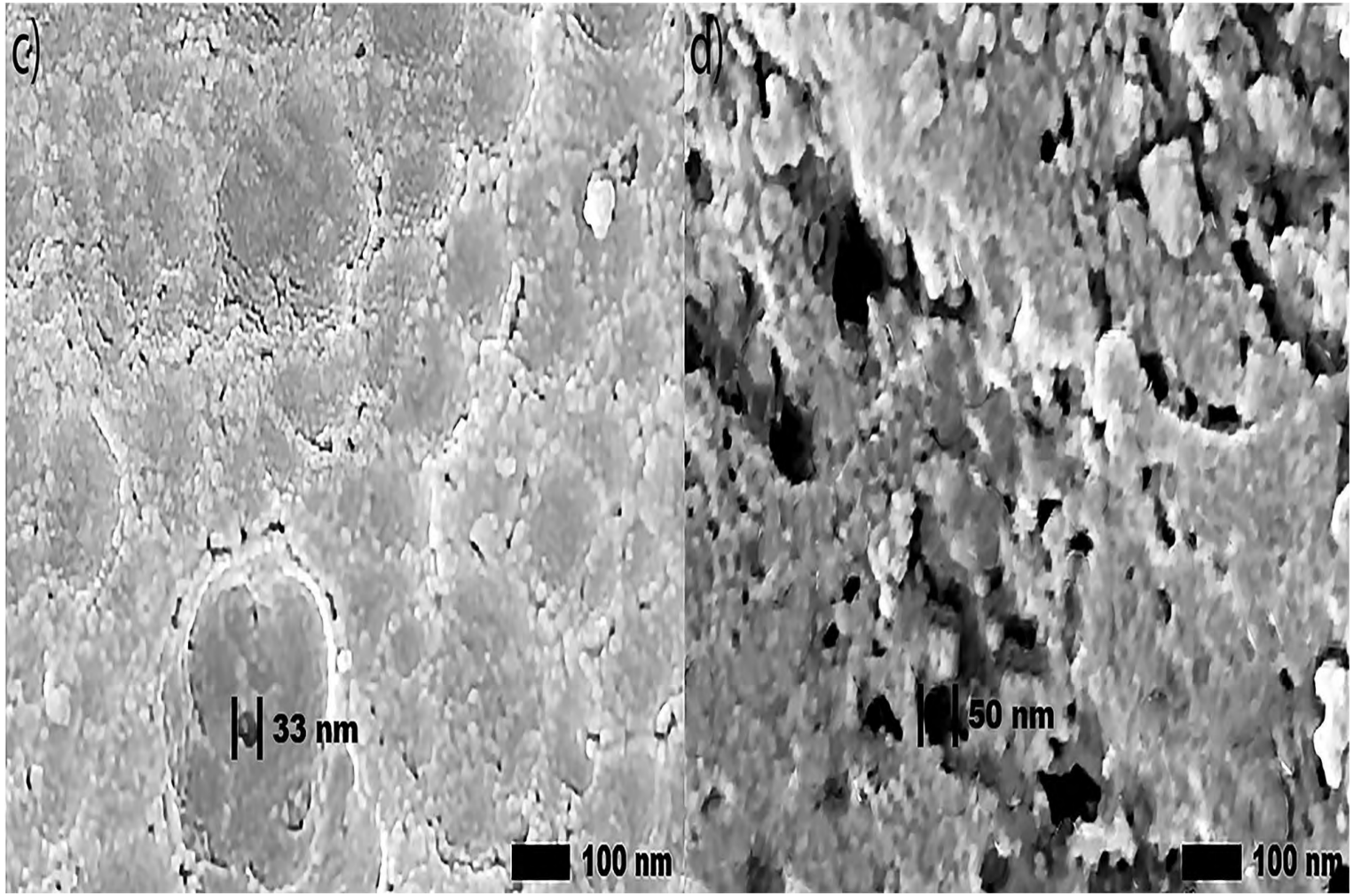

Figure 4.3(c-d) Secondary SEM images (100,000×) of the surface morphology reveal circular pores created in the anodization process, respectively, in the OS1 process. Left images show specimens anodized for 10 mins and right images show specimens anodized for 30 mins. Shown pore sizes were computed with ImageJ [130].

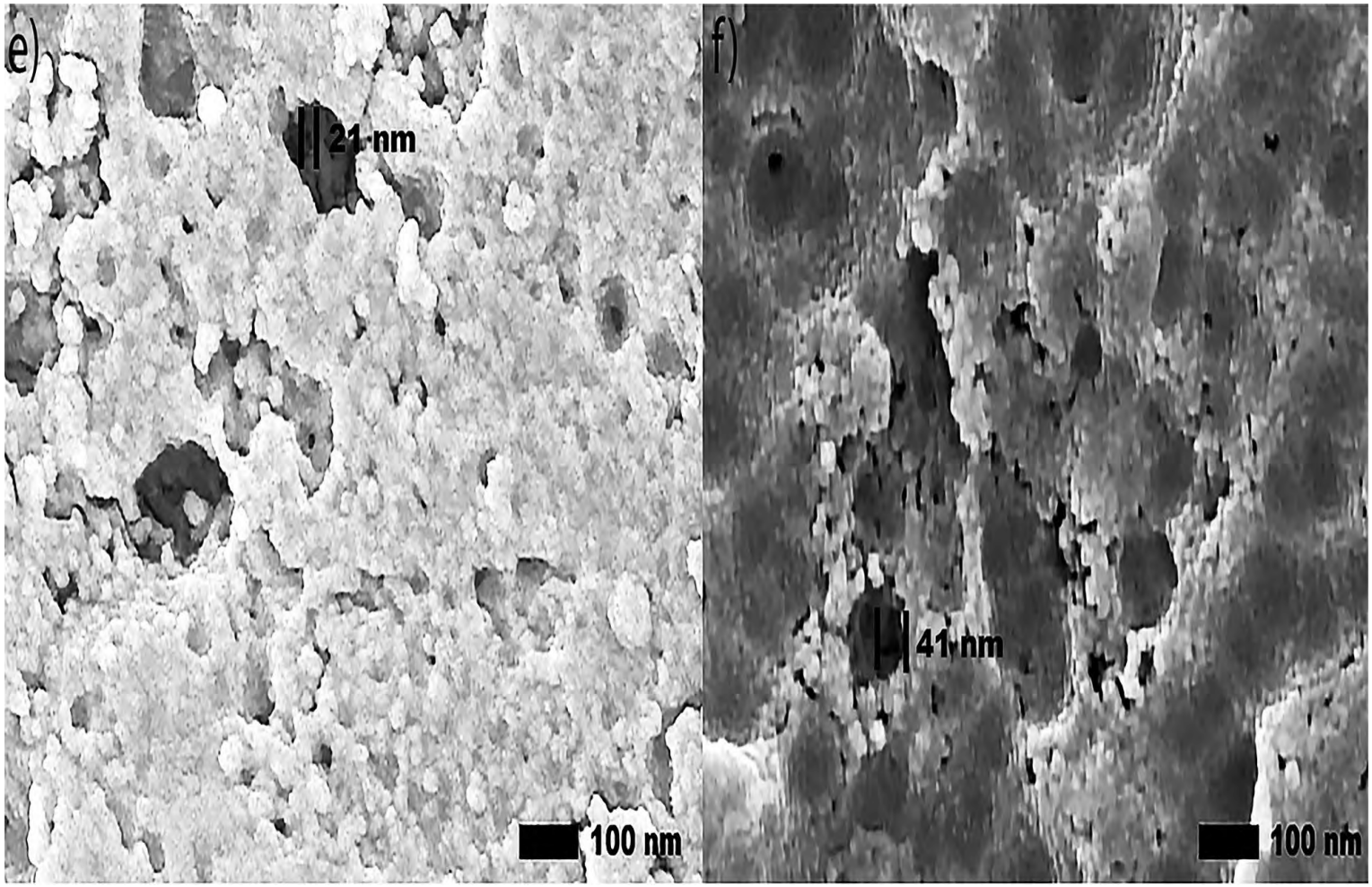

Figure 4.3(e-f) Secondary SEM images (100,000×) of the surface morphology reveal circular pores created in the anodization process, respectively, in the OS2 process. Left images show specimens anodized for 10 mins and right images show specimens anodized for 30 mins. Shown pore sizes were computed with ImageJ [130].

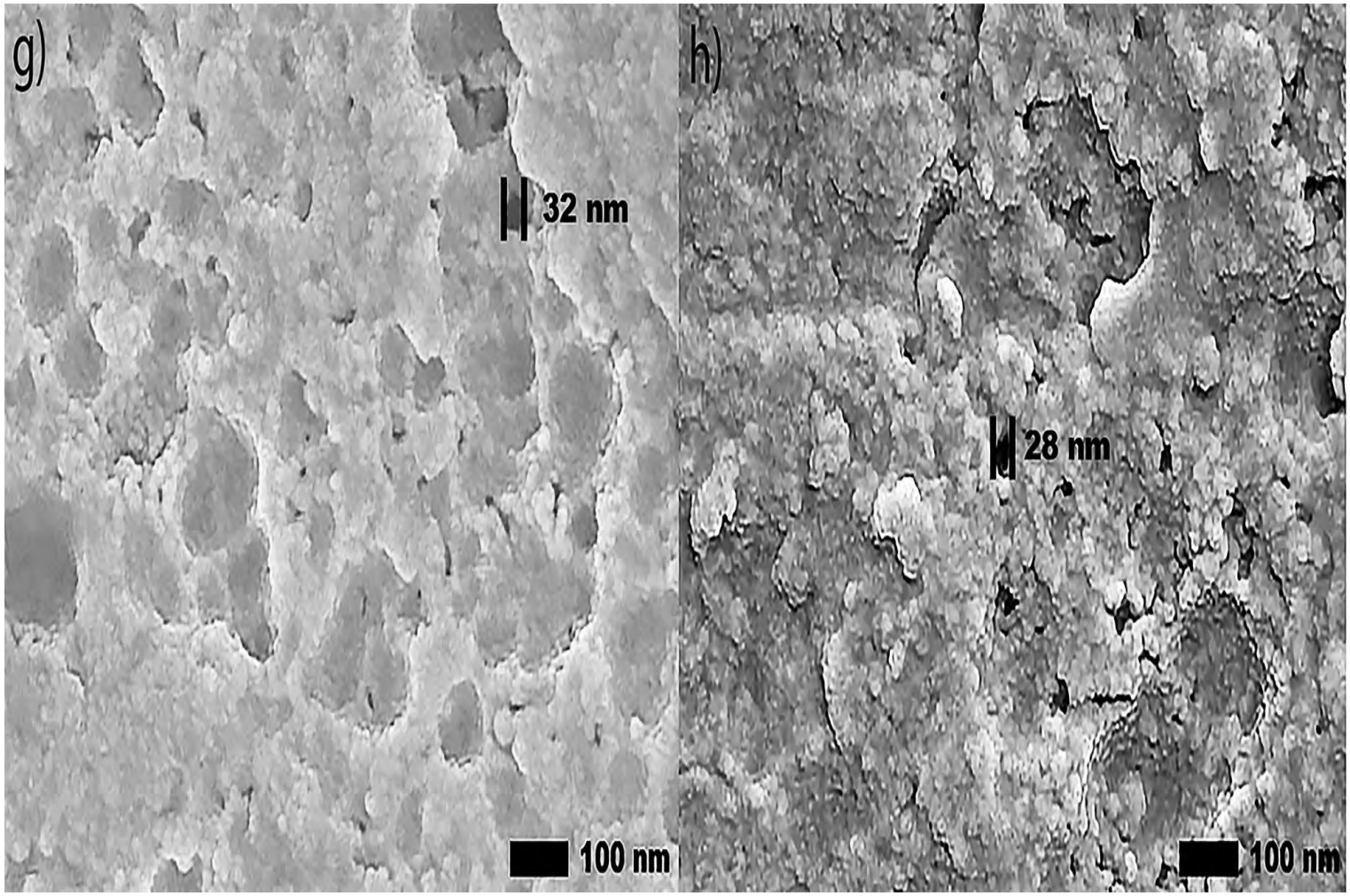

Figure 4.3(g-h) Secondary SEM images (100,000×) of the surface morphology reveal circular pores created in the anodization process, respectively, in the MS1 process. Left images show specimens anodized for 10 mins and right images show specimens anodized for 30 mins. Shown pore sizes were computed with ImageJ [130].

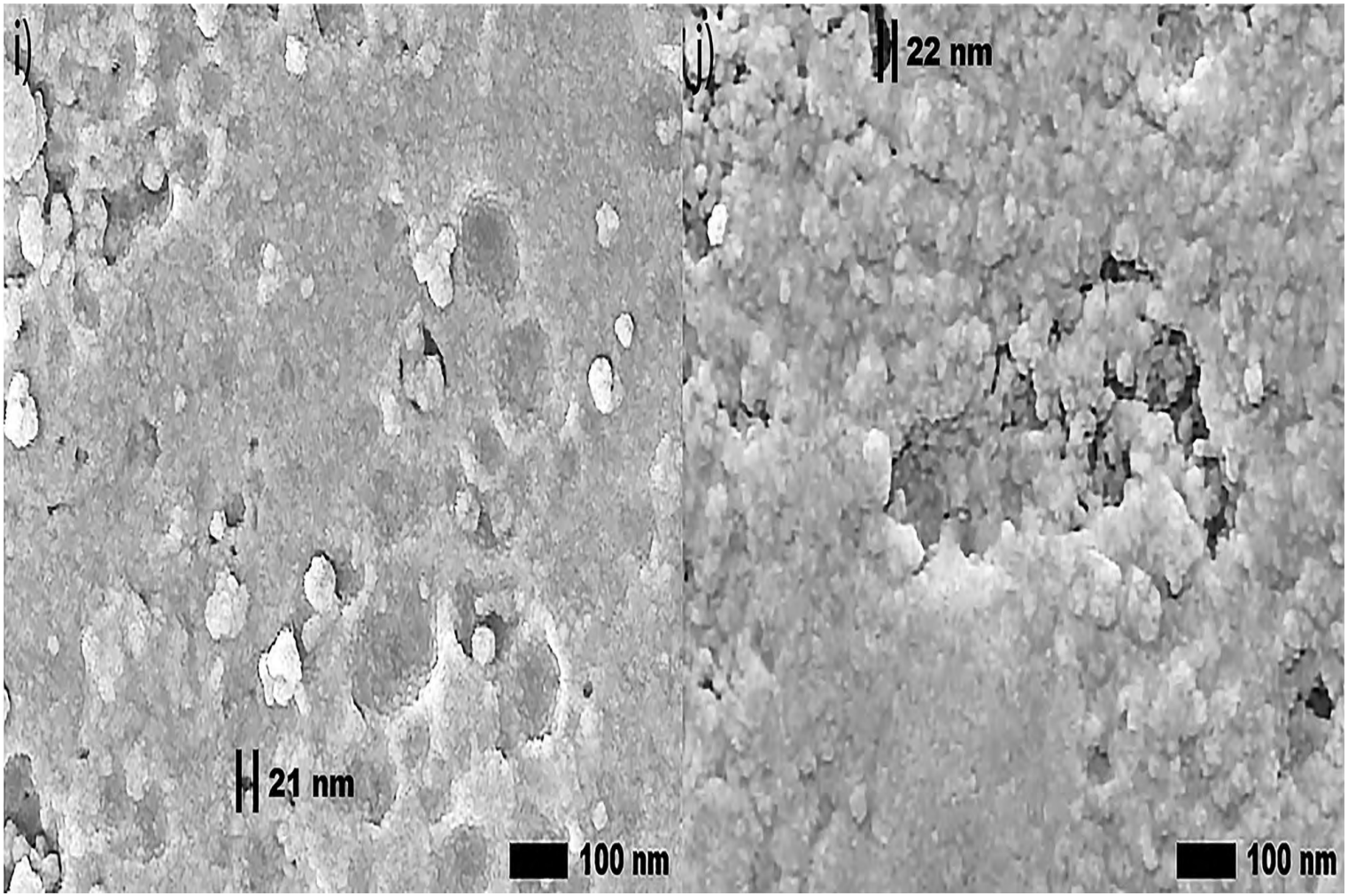

Figure 4.3(i-j) Secondary SEM images (100,000×) of the surface morphology reveal circular pores created in the anodization process, respectively, in the MS2 process. Left images show specimens anodized for 10 mins and right images show specimens anodized for 30 mins. Shown pore sizes were computed with ImageJ [130].

4.3.1.3 Microhardness of anodized specimens. **Table 4.4** lists the average microhardness values in Mpa. It is noticeable that the coating hardness increases with the coating thickness. Compared to standard process Base, the hardness of coatings formed in processes OS2, MS1, and MS2 increased by 6.6%, 8.7%, 12.6%, respectively. Process OS1 had an 11.1% reduction in hardness compared to the Base. Hardness measurements presented in **Table 4.4** indicate that the hardness of the coating is dependent on the coating thickness. The results of statistical analysis presented in **Table 4.4** demonstrate that a difference between the influence of anodizing processes in Group 1 and Group 2 on the microhardness is statistically significant as $FF > FF_{0.05}$ and $0.05 > PP_{0.05}$.

4.3.1.4 Anodic coating resistance to acid dissolution. The resistance to dissolution was characterized by immersing specimens in a chromic and phosphoric acid bath for 15 mins and then calculating the weight of anodic coating removed. Measurements are reported in **Table 4.4** in the following terms: weight loss per coating area, mg/dm^2, loss of total coating, %, and weight loss per micron, mg/μm. Anodic coatings were completely dissolved on all specimens anodized for 10 mins. Specimens anodized for 30 mins in Base, OS1 and OS2 processes lost more than 99.0% of its anodic coating while specimens anodized in MS1 and MS2 processes lost 95.2% and 96.2%, respectively. As BSE imaging in **Figure 4.**5 illustrate, a reduction of porosity and surface asperities also increased resistance to acid dissolution by reducing the available interstitial regions of a coating to be dissolved. Measurements presented in **Table 4.4** demonstrate that anodic coating resistance to acid dissolution increases with coating thickness. The results of statistical analysis presented in **Table 4.4** demonstrate that a difference between the influence of anodizing processes in Group 1 and Group 2 on the acid dissolution of coatings is statistically significant as $FF > FF_{0.05}$ and $0.05 > PP_{0.05}$.

4.3.1.5 Corrosion resistance of anodized specimens

4.3.1.5.1 Salt spray (fog) testing

Salt Spray (Fog) Testing was conducted on sealed specimens anodized for 10 mins and 30 mins. For specimens anodized for 10 mins, coatings produced by the Base, OS1 and MS2 processes formed 2 ± 1 pits per process. Coatings produced by the OS2 and MS1 processes, formed just one pit per process. For specimens anodized for 30 mins, no pits formed on coatings produced in the Base, OS1, OS2 and MS1 processes, while the coating produced from the MS2 process formed an average of 2 ± 1 pits. The presented results indicate that the coating corrosion resistance is mainly attributed to the ability of sealing the pores and improved with forming a thicker anodic coating.

4.3.1.5.2 Electrochemical impedance spectroscopy (EIS)

Plots in **Figure 4.4(a-f)** report the EIS response of unsealed specimens anodized for 30 mins. The overall EIS spectra appear to be minimally affected by the anodic coating morphology as all impedance moduli followed a similar cycloid curve with increasing frequency. In the EIS spectrum of anodic specimens, the low frequency region represents properties of the barrier layer and localized corrosion sites, while the high frequency range represents the behavior of the porous layer of the coating [133]. Plots in **Figure 4.4(c)** and **Figure 4.4(e)** for coatings formed in OS2 and MS2, respectively, exhibit a slightly elevated impedance moduli in the low frequency region below 1kHz. Bode plots in **Figure 4.4(f)** illustrate the EIS spectra of specimens anodized in Base, OS1, OS2, MS1 and MS2 processes. In **Figure 4.4(f)**, the impedance moduli decreased with increasing frequency for all processes. The phase angles rapidly depress at high frequencies, with the exception of MS2, that slightly elevates in the region 10 kHz-1 MHz and then reduces similarly to other anodizing processes.

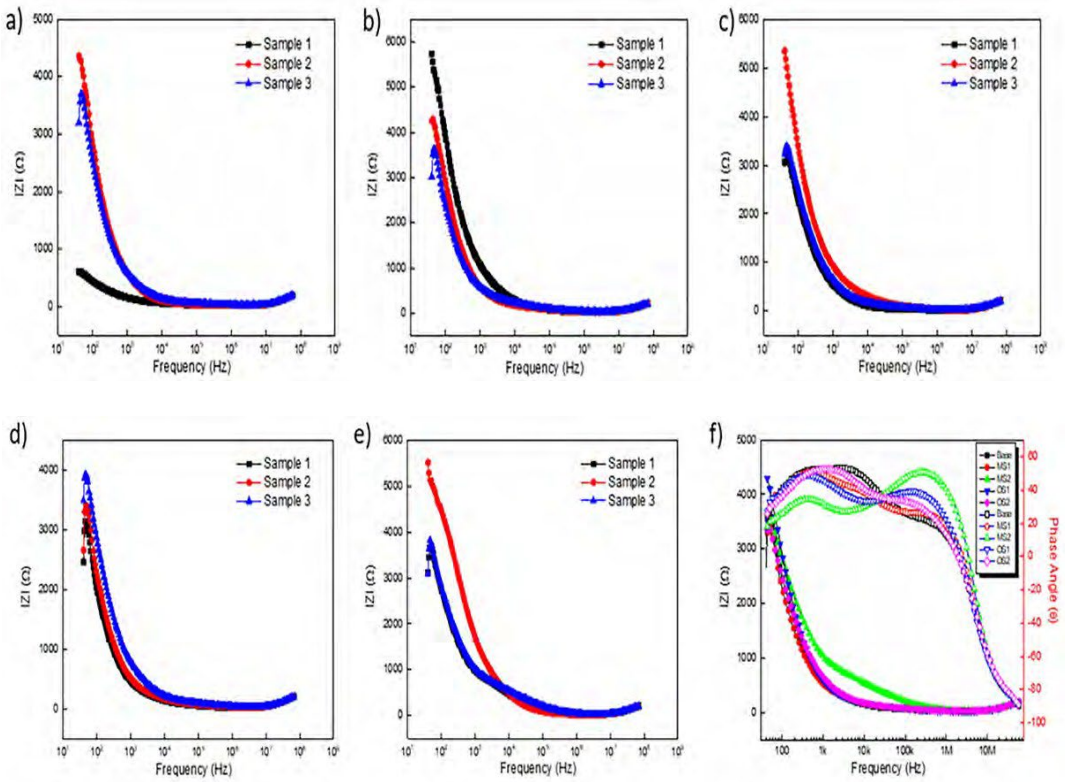

Figure 4.4(a-f) EIS spectra obtained for unsealed specimens anodized for 30 mins in processes (a) Base, (b) OS1, (c) OS2, (d) MS1, (e) MS2, and (f) Bode Plots.

4.3.1.6 SEM/EDS analysis. Secondary SEM images (100,000x) of anodic coatings posted in **Figure 4.3** show the surface of coatings anodized in Base, OS1, OS2, MS1 and MS2 processes over 10 and 30 mins. The results demonstrate that multistep ramping of applied current density substantially improved the coating morphology. In all specimens, coatings became more undulated and porous with distinct fragmentation patterns formed during the final stage of anodization. These undesired features are likely caused by increasing nonuniformity in the growth of a coating due to higher voltages used at this stage of the process. Coatings formed in the Base, OS1 and OS2 processes during 10 mins exhibited a porous morphology. This condition was greatly exacerbated during the final period of the 30-min processing. The MS1 and MS2 processes produced coatings

that were considerably smoother and less undulated (**Figure 4.3**). The presented results demonstrate that utilizing multistep ramping at the beginning of an anodization process promotes the formation of an anodic coating with a finer morphology and a lower porosity compared to processes without or with a single ramp. Higher potential applied at the beginning of the process inhibits anodic oxidation at certain locations, likely due to the presence of copper and other alloying elements in the coating. Copper contamination can promote uneven film growth and increased electrical resistance. The SE and BSE SEM images posted in **Figure 4.5(a-t)** provide a large-scale view of the surface of specimens anodized in Base, OS1, OS2, MS1, and MS2 processes for 10 and 30 mins.

The BSE imaging provides a contrasting aspect of the morphology to illustrate the presence of voids, defects, and porosity of the coating, while the SE imaging illustrates the specimen surface topography. Taken together, both types of imaging provide a detailed view of the coating morphology and surface anomalies. In **Figure 4.5(a-d)**, the coating produced by the Base process is populated with cracks, voids, and asperities across the entire surface. In **Figure 4.5(i-l)** coatings produced by the OS2 process exhibit similar defects, but to a lesser extent. Coatings formed in the OS1 process (**Figure 4.5(e-h)**) were intact after the ramping period, but eventually became more porous with a longer anodizing time.

Processes MS1 and MS2 produced a coating with fewer voids and imperfections as gradual increases in the applied current density allow for formation of more intact, void-free coatings (**Figure 4.5(m-t)**).

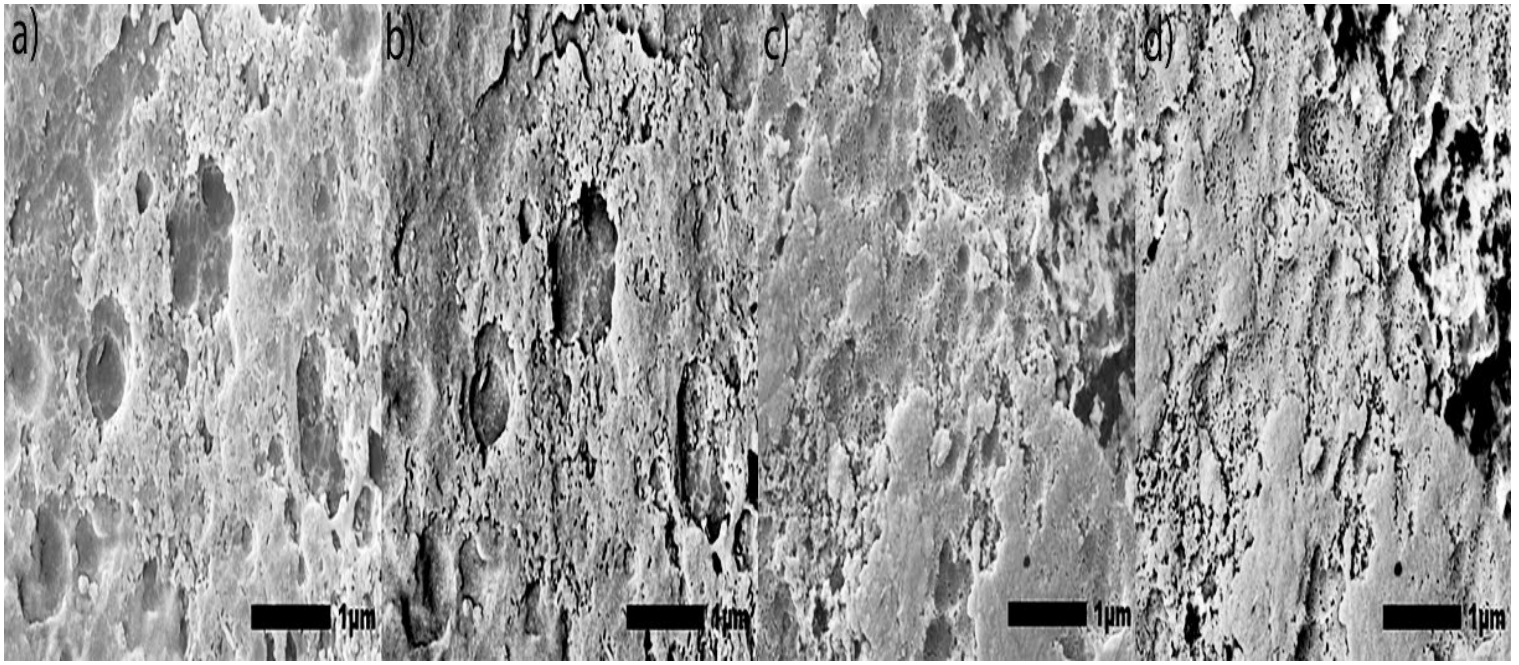

Figure 4.5(a-d) Large-scale SEM images (30,000x magnification) of the coating surface were obtained with the use of back-scattered electrons (BSE) imaging and secondary electrons (SE) imaging: 10 kV under LED for SE images and BED-C for BSE images was used, and the height of the specimen stage, WD, of 10 mm. Specimens anodized respectively in [Base]: a) 10 min SE, b) 10 min BSE, c) 30 min SE, d) 30 min BSE.

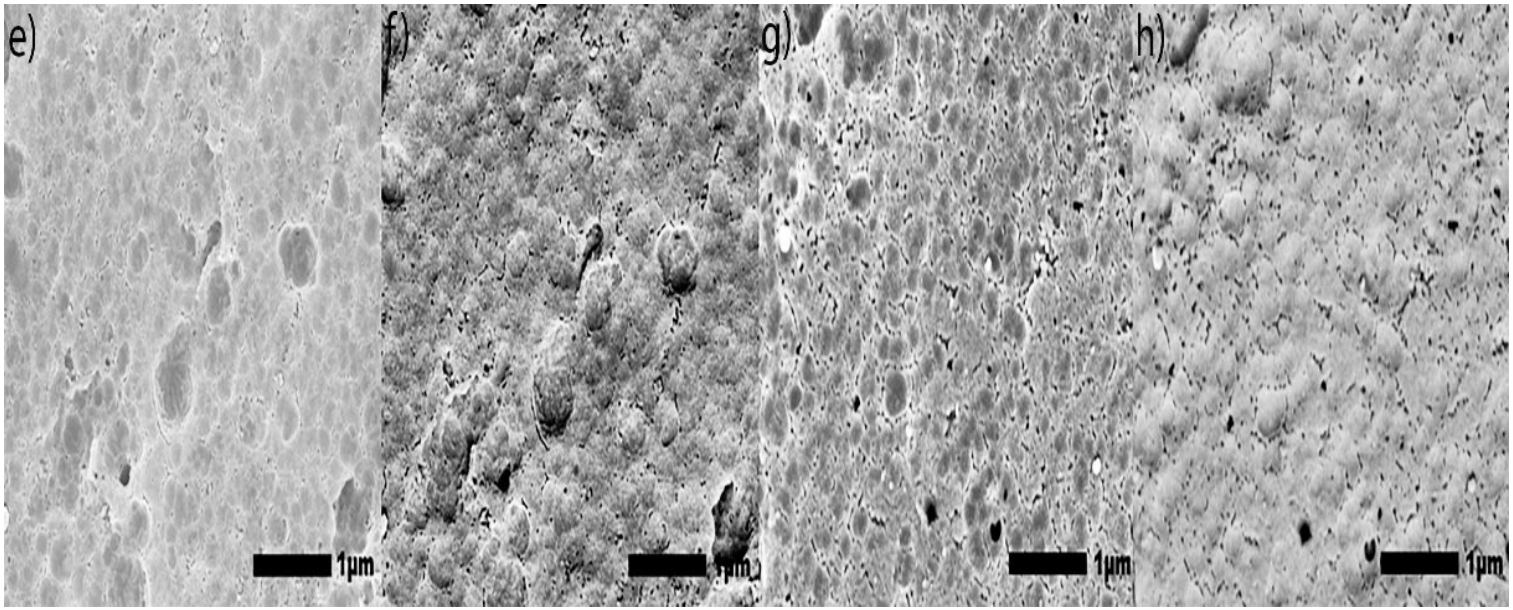

Figure 4.5(e-h) Large-scale SEM images (30,000x magnification) of the coating surface were obtained with the use of back-scattered electrons (BSE) imaging and secondary electrons (SE) imaging: 10 kV under LED for SE images and BED-C for BSE images was used, and the height of the specimen stage, WD, of 10 mm. Specimens anodized respectively in [OS1]: e) 10 min SE, f) 10 min BSE, g) 30 min SE, h) 30 min BSE.

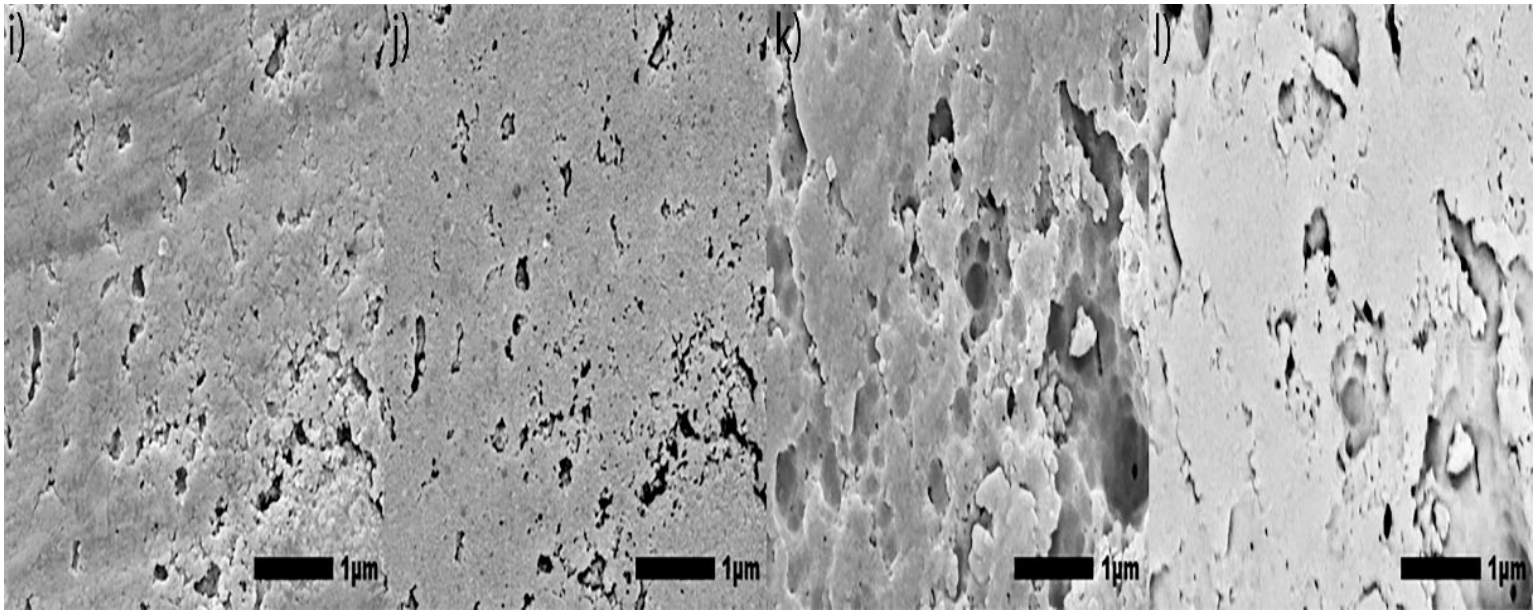

Figure 4.5(i-l) Large-scale SEM images (30,000x magnification) of the coating surface were obtained with the use of back-scattered electrons (BSE) imaging and secondary electrons (SE) imaging: 10 kV under LED for SE images and BED-C for BSE images was used, and the height of the specimen stage, WD, of 10 mm. Specimens anodized respectively in [OS2]: i) 10 min SE, j) 10 min BSE, k) 30 min SE, l) 30 min BSE.

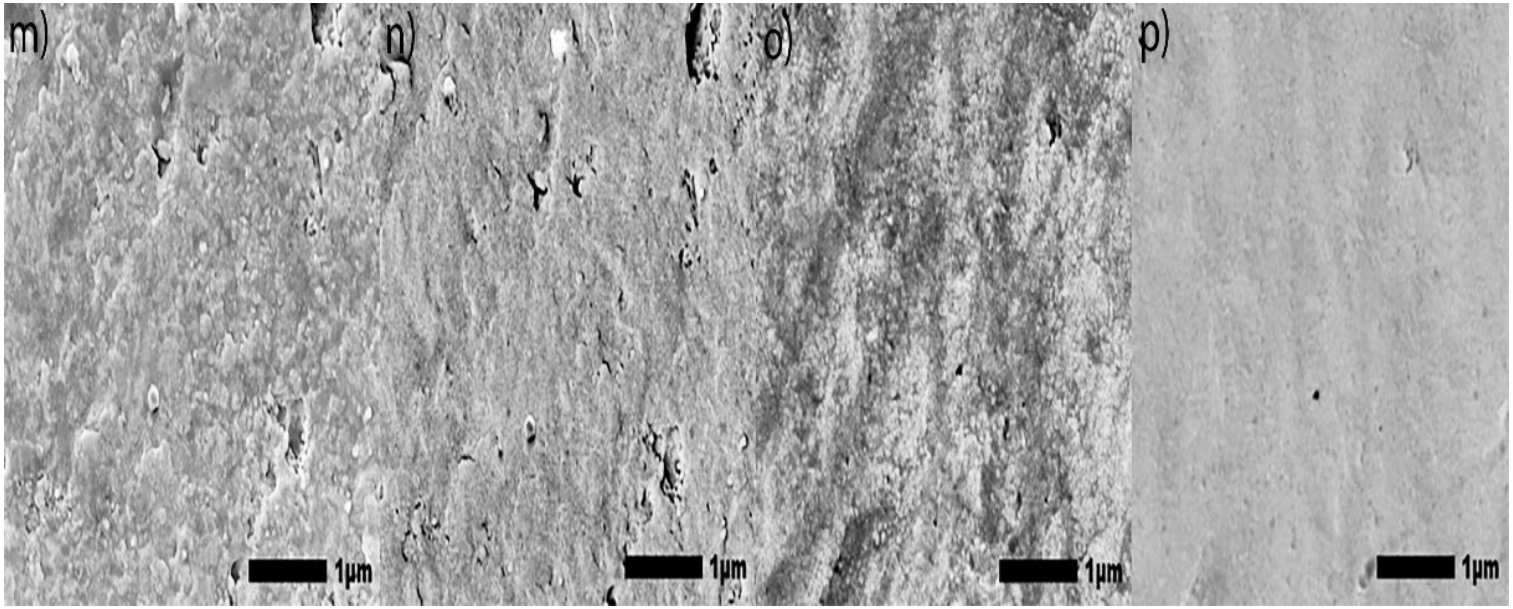

Figure 4.5(m-p) Large-scale SEM images (30,000x magnification) of the coating surface were obtained with the use of back-scattered electrons (BSE) imaging and secondary electrons (SE) imaging: 10 kV under LED for SE images and BED-C for BSE images was used, and the height of the specimen stage, WD, of 10 mm. Specimens anodized respectively in [MS1]: m) 10 min SE, n) 10 min BSE, o) 30 min SE, p) 30 min BSE.

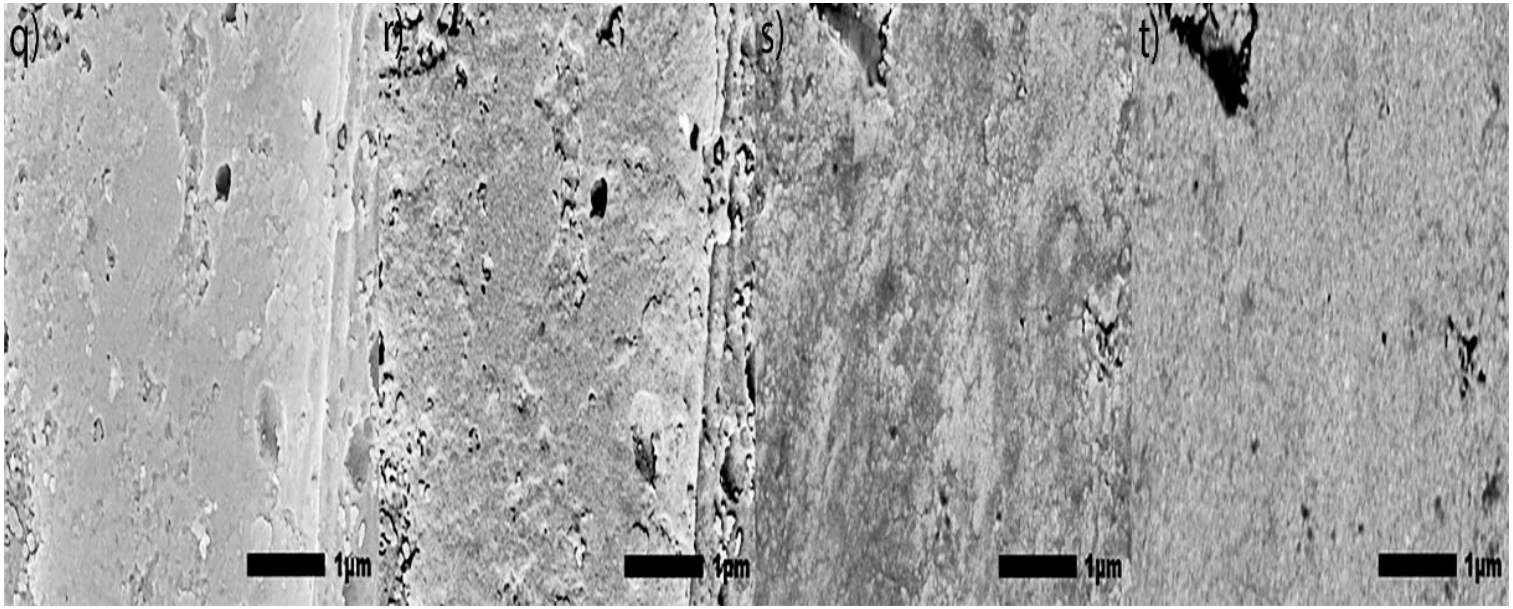

Figure 4.5(q-t) Large-scale SEM images (30,000x magnification) of the coating surface were obtained with the use of back-scattered electrons (BSE) imaging and secondary electrons (SE) imaging: 10 kV under LED for SE images and BED-C for BSE images was used, and the height of the specimen stage, WD, of 10 mm. Specimens anodized respectively in [MS2] q) 10 min SE, r) 10 min BSE, s) 30 min SE, t) 30 min BSE.

SEM images posted in **Figure 4.6** provide a large-scale view of the surface of specimens anodized in Base, OS1, OS2, MS1 and MS2 processes for 10 and 30 mins.

The Energy Dispersive X-Ray Spectroscopy (EDS) analysis was performed at 12 sampling sites in flat, non-pitted regions. In **Figure 4.6**, sites labeled 1 – 4 are representations of the 12 sites chosen. Two constraints impede the quantification of EDS measurements presented. First, the heights of the peaks for elements Cu, S, Mn, Mg, etc. (**Figure 4.6**) vary from site to site shown in these images due to the inhomogeneity of the coating. Next, the 10 kV beam was used for measurements as the depth of the 20 kV beam penetration was around 2-5 μm. It therefore requires the use of Lα characteristic X-ray (keV) for measuring concentrations of these elements that could render the error as high as 3 – 5 wt. % due to peak overlap [134]. For these reasons, reported concentrations of Cu, S, Mg and Mn can be used only as reference points.

Images of an untreated specimen acquired by SE and BSE imaging are posted in **Figure 4.7(a) and 7(b)**, respectively. The specimen was chemically cleaned with the same method as the other specimens, to provide detail on the surface prior to anodization. EDS measurements shown in **Figure 4.7(b)** were taken in locations with particles (1-4) and without particles (5-8). Results presented in **Table 4.1** show the composition of these regions. The SE image in **Figure 4.7(a)** and BSE image in **Figure 4.7(b)** demonstrate a difference in local surface compositions, as the lighter color shows particles with a lower content of aluminum and a higher content of O, Cu, Mg, Mn, and Fe compared to the surrounding aluminum rich regions (**Table 4.1**).

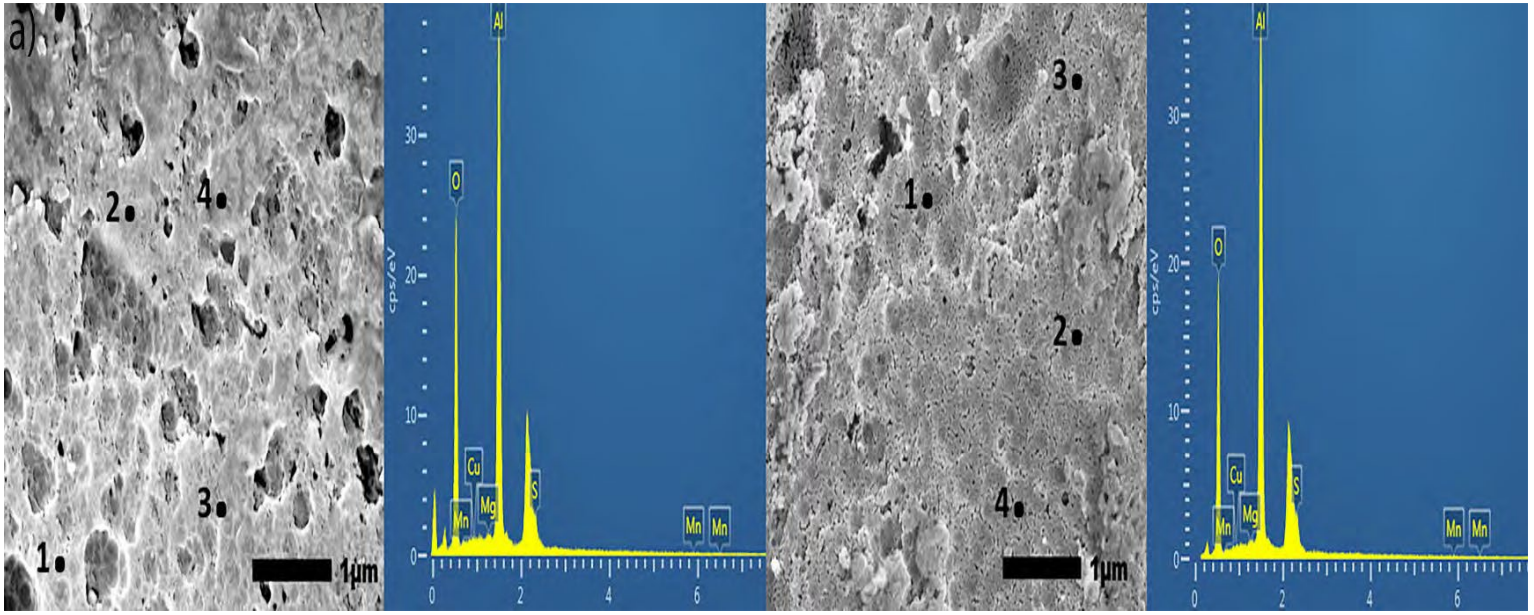

Figure 4.6a Secondary SEM images (30,000x) of specimens anodized in the Base process; for 10 mins, left image, and for 30 mins, right image. The EDS analysis was performed at 12 sampling sites in flat, non-pitted regions of the anodic coating. Sites labeled 1 – 4 are representations of the 12 sites chosen. The EDS spectrum shown on the adjacent image is data for site 1.

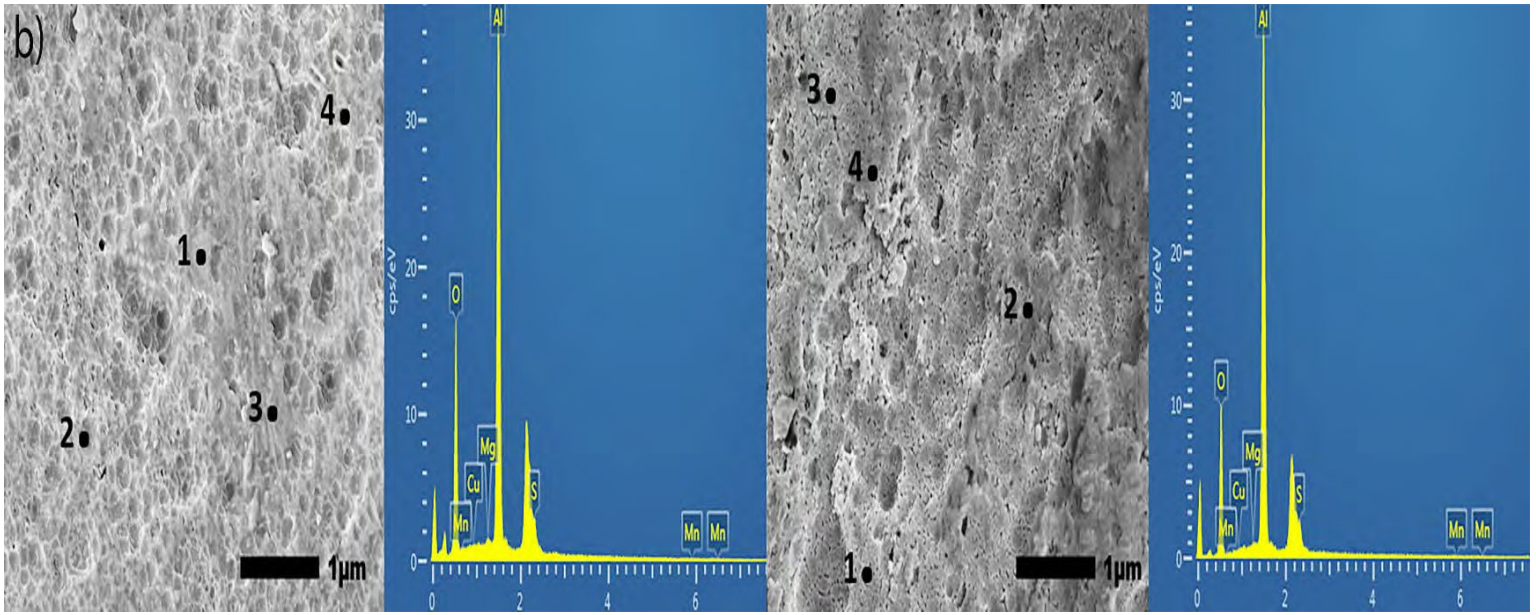

Figure 4.6b Secondary SEM images (30,000x) of specimens anodized in the OS1 process; for 10 mins, left image, and for 30 mins, right image. The EDS analysis was performed at 12 sampling sites in flat, non-pitted regions of the anodic coating. Sites labeled 1 – 4 are representations of the 12 sites chosen. The EDS spectrum shown on the adjacent image is data for site 1.

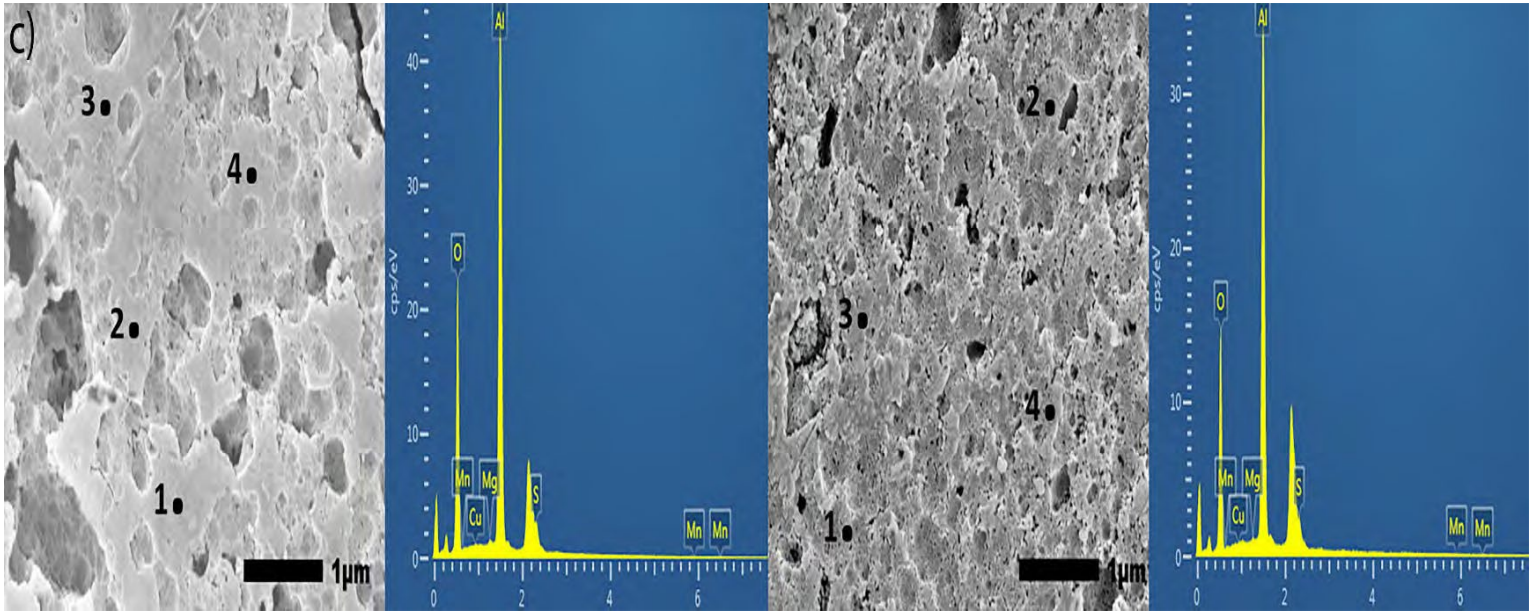

Figure 4.6c Secondary SEM images (30,000x) of specimens anodized in the OS2 process; for 10 mins, left image, and for 30 mins, right image. The EDS analysis was performed at 12 sampling sites in flat, non-pitted regions of the anodic coating. Sites labeled 1 – 4 are representations of the 12 sites chosen. The EDS spectrum shown on the adjacent image is data for site 1.

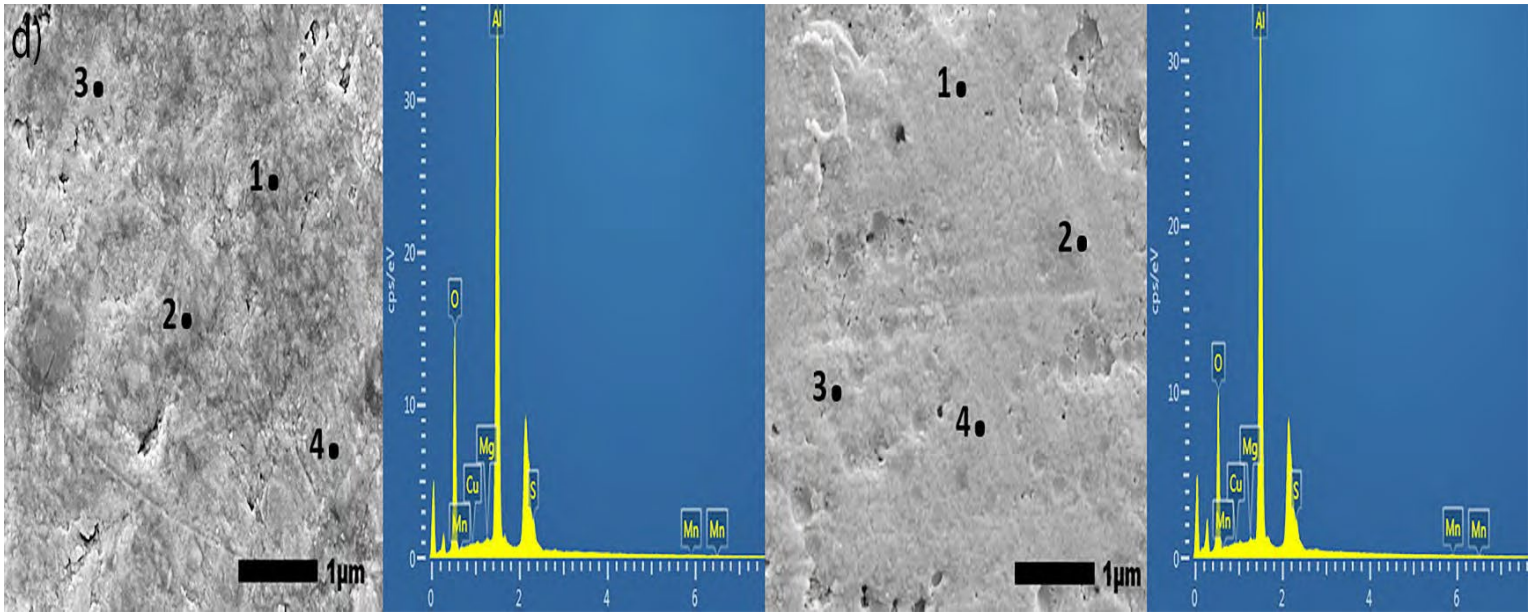

Figure 4.6d Secondary SEM images (30,000x) of specimens anodized in the MS1 process; for 10 mins, left image, and for 30 mins, right image. The EDS analysis was performed at 12 sampling sites in flat, non-pitted regions of the anodic coating. Sites labeled 1 – 4 are representations of the 12 sites chosen. The EDS spectrum shown on the adjacent image is data for site 1.

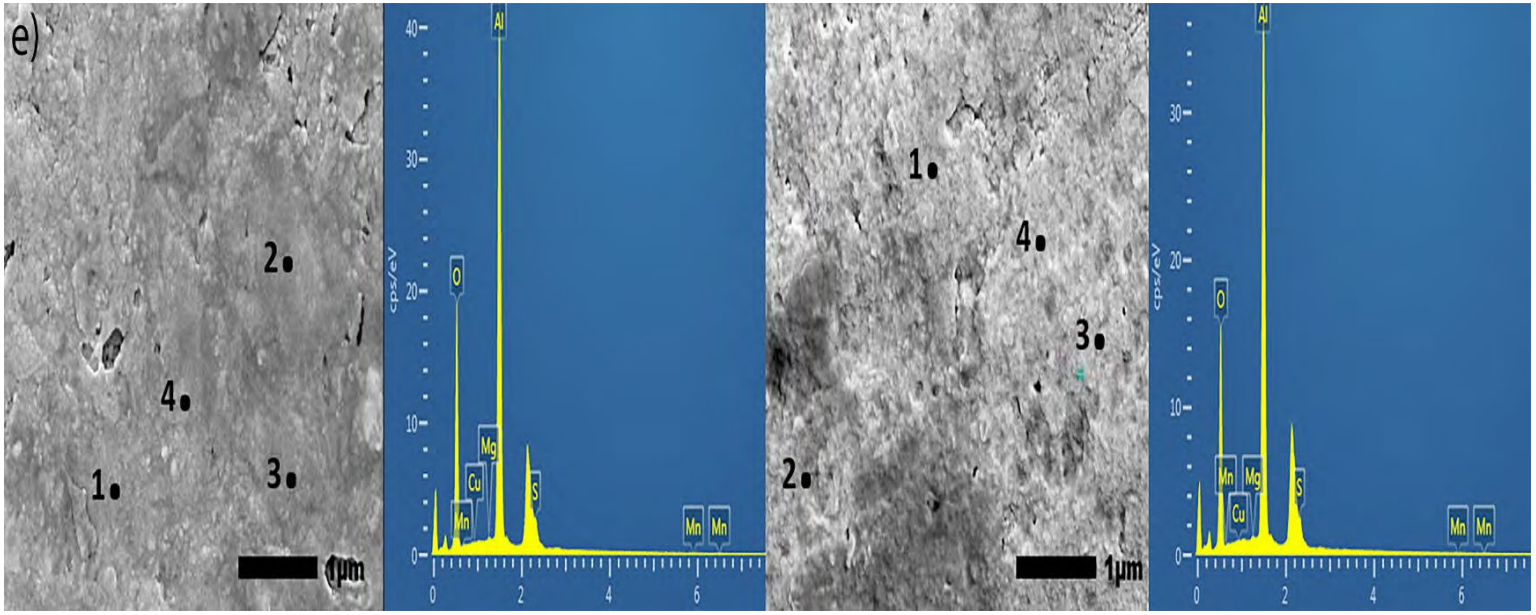

Figure 4.6e Secondary SEM images (30,000x) of specimens anodized in the MS2 process; for 10 mins, left image, and for 30 mins, right image. The EDS analysis was performed at 12 sampling sites in flat, non-pitted regions of the anodic coating. Sites labeled 1 – 4 are representations of the 12 sites chosen. The EDS spectrum shown on the adjacent image is data for site 1.

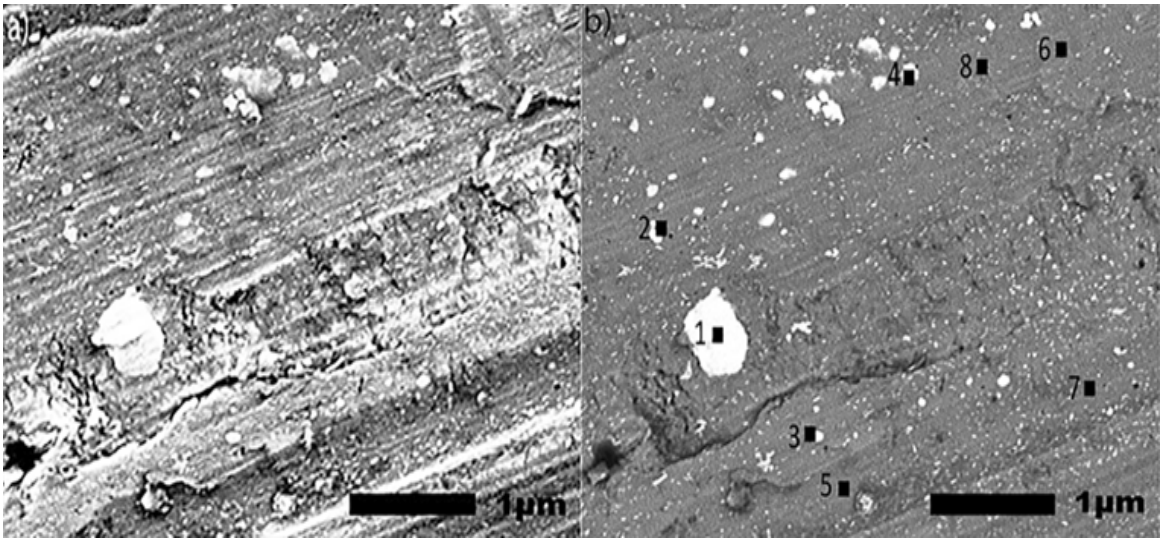

Figure 4.7(a-b). SEM images (30,000x) utilizing secondary electron (SE) imaging (a) and back scattered electrons (BSE) (b) of a non-anodized specimen. The EDS analysis was performed at eight locations (4 with particles and 4 without particles) to evaluate the surface composition of a non-anodized specimen.

Plots in **Figure 4.8** demonstrate the effect of anodizing processes Base, OS1, OS2, MS1, MS2 on the content of aluminum and oxygen in coatings formed over 10 mins and 30 mins.

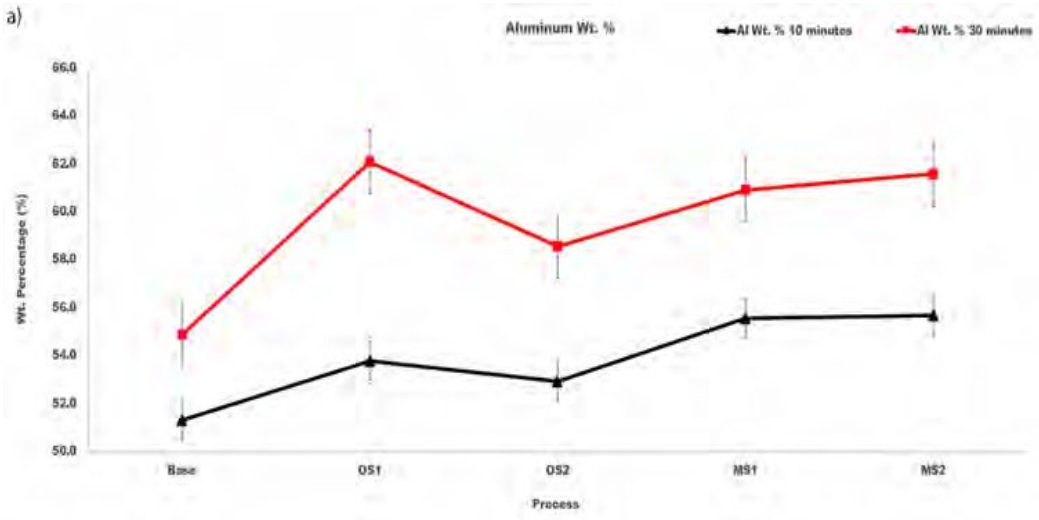

Figure 4.8a The amount, wt. % of aluminum, in the surface of coating morphology of specimens anodized in Base, OS1, OS2, MS1 and MS2 processes over 10 min (duration of ramping in stepwise processes) and the entire period of 30 min. Reported values were averaged over four sites displaced in images in **Figure 4.6** where the EDS analysis was performed.

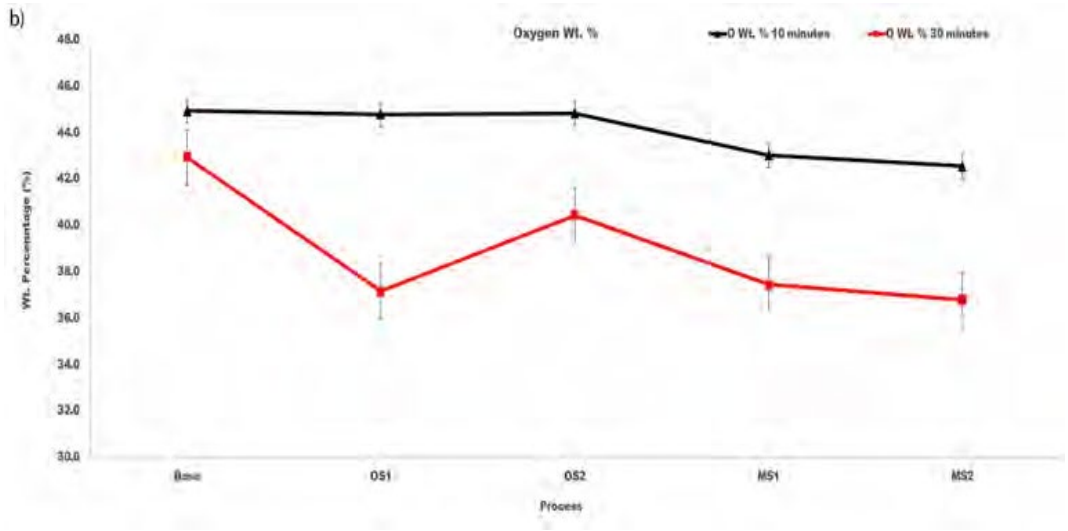

Figure 4.8b The amount, wt. % of oxygen, in the surface of coating morphology of specimens anodized in Base, OS1, OS2, MS1 and MS2 processes over 10 min (duration of ramping in stepwise processes) and the entire period of 30 min. Reported values were averaged over four sites displaced in images in **Figure 4.6** where the EDS analysis was performed.

For all processes, the coatings formed in the 30-min anodizing process had higher wt.% of aluminum and lower wt.% of oxygen when compared to the 10-min process. The atomic Al/O ratios in coatings formed by anodization for 10 mins and 30 mins are listed in **Table 4.5**. As can be seen in **Figure 4.8(a) and (b)** and **Table 4.5**, differences between the aluminum and oxygen contents in coatings created by different anodizing processes exceed variations of their concentrations within a coating built under the same anodizing conditions. Compared to Base process, stepwise processes MS1 and MS2 created coatings with the aluminum content larger by 4 - 7 wt.% and the oxygen content lower by 2 - 6 wt.%.

Table 4.5. The Atomic Al/O Ratios in Coatings Formed by Anodization Over 10 mins and 30 mins in Base, OS1, OS2, MS1 and MS2 Processes. Statistical Analysis of Data for Anodization in Group 1 (Base, OS1, OS2) and Group 2 (MS1, MS2) Processes Over 10 mins and 30 mins is Listed Below

Process	**Al/O, 10 mins**	**Al/O, 30 mins**
Base	0.69 ± 0.04	0.76 ± 0.05
OS1	0.73 ± 0.05	1.00 ± 0.08
OS2	0.71 ± 0.05	0.86 ± 0.05
MS1	0.77 ± 0.06	0.97 ± 0.06
MS2	0.79 ± 0.06	0.99 ± 0.06

Al/O Ratio – 10 mins					
Groups	Count	Average	$P_{0.05}$	F	$F_{0.05}$
Group 1	36	0.71 ± 0.02	2.3×10^{-5}	21.2	4
Group 2	24	0.77 ± 0.06			

Al/O Ratio – 30 mins					
Groups	Count	Average	$P_{0.05}$	F	$F_{0.05}$
Group 1	36	0.87 ± 0.12	2.0×10^{-4}	15.9	4
Group 2	24	0.98 ± 0.06			

The Al/O ratio increases with longer anodizing time and all values are greater than the Al/O stoichiometric ratio of 0.67 in the Al_2O_3 oxide. The results of statistical analysis presented in **Table 4.5** demonstrate that a difference between the influence of anodizing processes in Group 1 and Group 2 on the Al/O ratio is statistically significant as $FF > FF_{0.05}$ and $0.05 > PP_{0.05}$.

SEM images in **Figures 4.3 and 4.5**, illustrate that utilizing multistep ramping of current density at the beginning of anodization promotes the formation of coating compositions higher in aluminum and lower in oxygen (higher Al/O ratios, **Table 4.5**). The EDS maps presented in **Figure 4.9** were acquired in two EDS runs. They illustrate the distribution of elements over the surface of specimens anodized in processes Base, OS1, OS2, MS1, and MS2 as well as over the surface of an untreated specimen. The EDS mapping image of an untreated specimen (**Figure 4.9(a)**) shows the presence of Fe and Si, mainly in two large particles. The dark particle has a higher concentration of Si and O and is likely a SiO_2 particle, whereas the light particle has

a higher concentration of Cu and Fe and is likely an AlCuFe particle [17]. However, Fe and Si were not observed on the surface of anodized specimens. The presence of sulfur seen in images posted in **Figure 4.9** is likely caused by the absorption of SO_4^{2-} ions penetrating into the anodic coating from the electrolyte. The EDS maps in **Figure 4.9** clearly demonstrate that concentrations of alloying elements in anodic coatings are very small, however, there are slight differences in the distribution of trace elements on the surface of coatings formed by different anodizing processes.

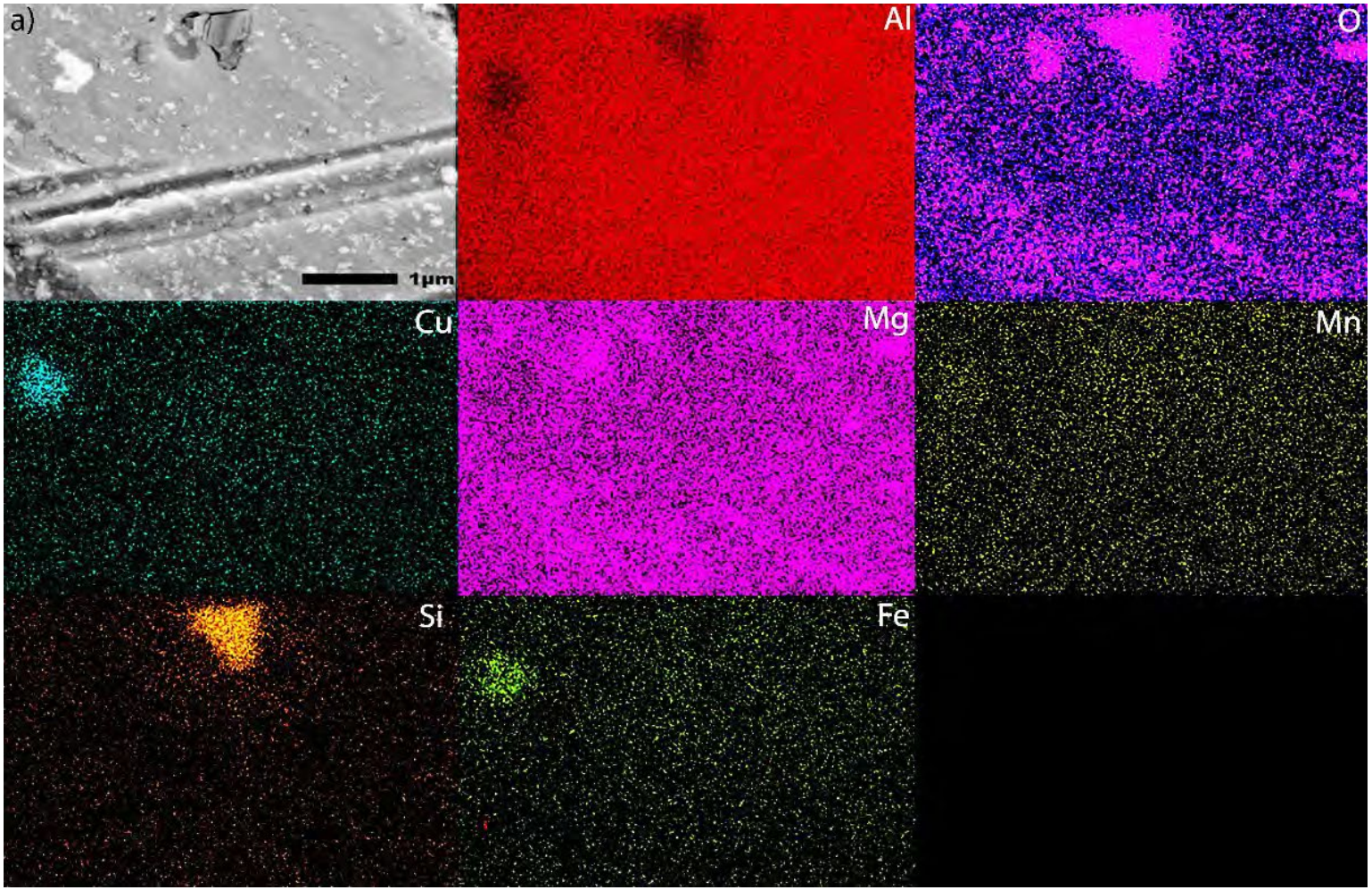

Figure 4.9a SEM images at 30,000x and EDS mapping images of the surface of (a) an untreated specimen. Images were obtained using 20 kV under LED. The acquisition time was about 45 mins to acquire 200 counts/pixel. Colors representing elements are as follows: Aluminum (red), oxygen (purple), copper (teal), magnesium (pink), manganese (yellow), silicon (orange), iron (lime) and sulfur (green).

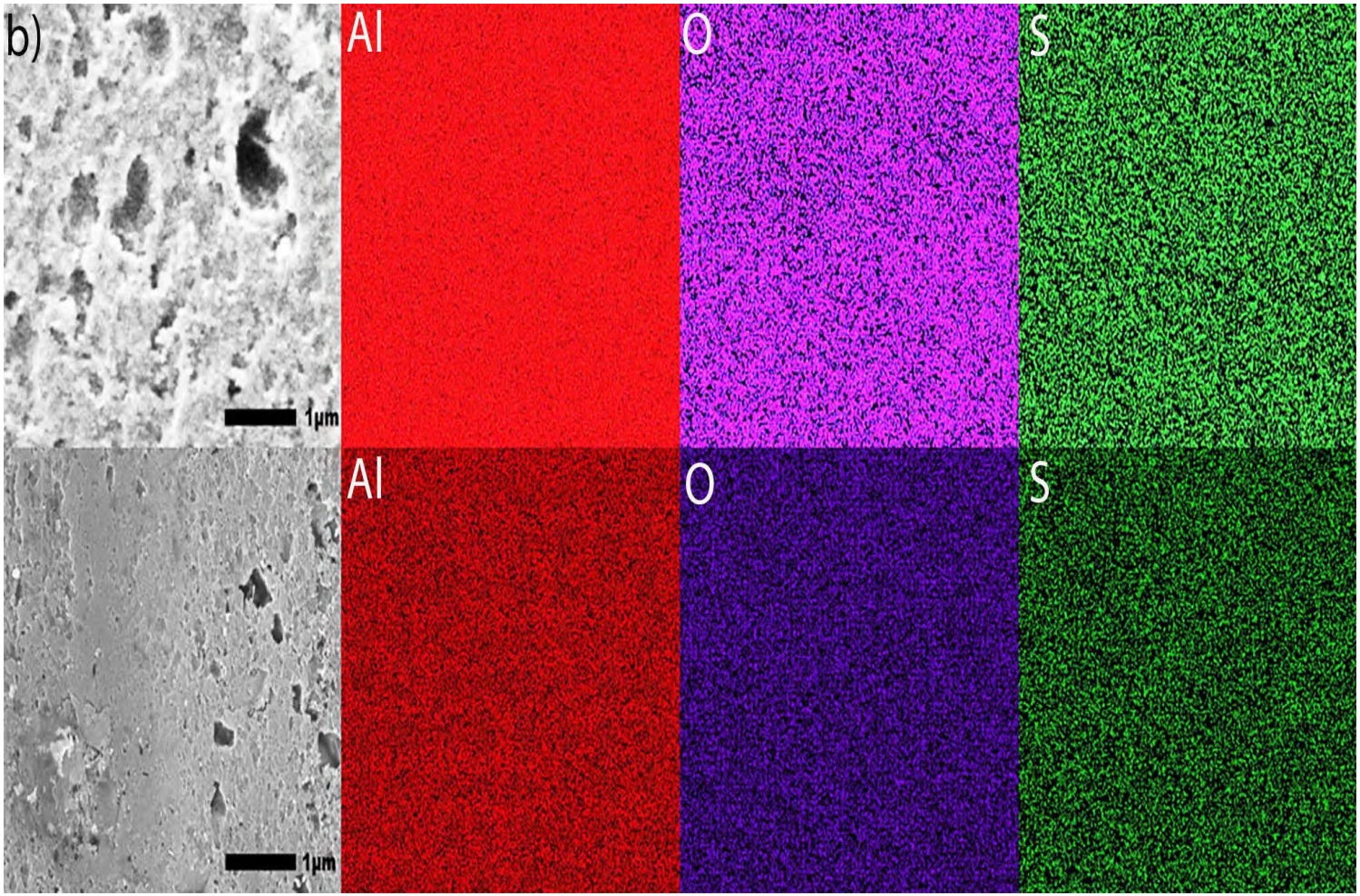

Figure 4.9b SEM images at 30,000x and EDS mapping images of the surface of a specimen anodized for 30 mins in process Base. Images were obtained using 20 kV under LED. The acquisition time was about 45 mins to acquire 200 counts/pixel (top row) and 325 counts/pixel (bottom row). Colors representing elements are as follows: Aluminum (red), oxygen (purple), and sulfur (green).

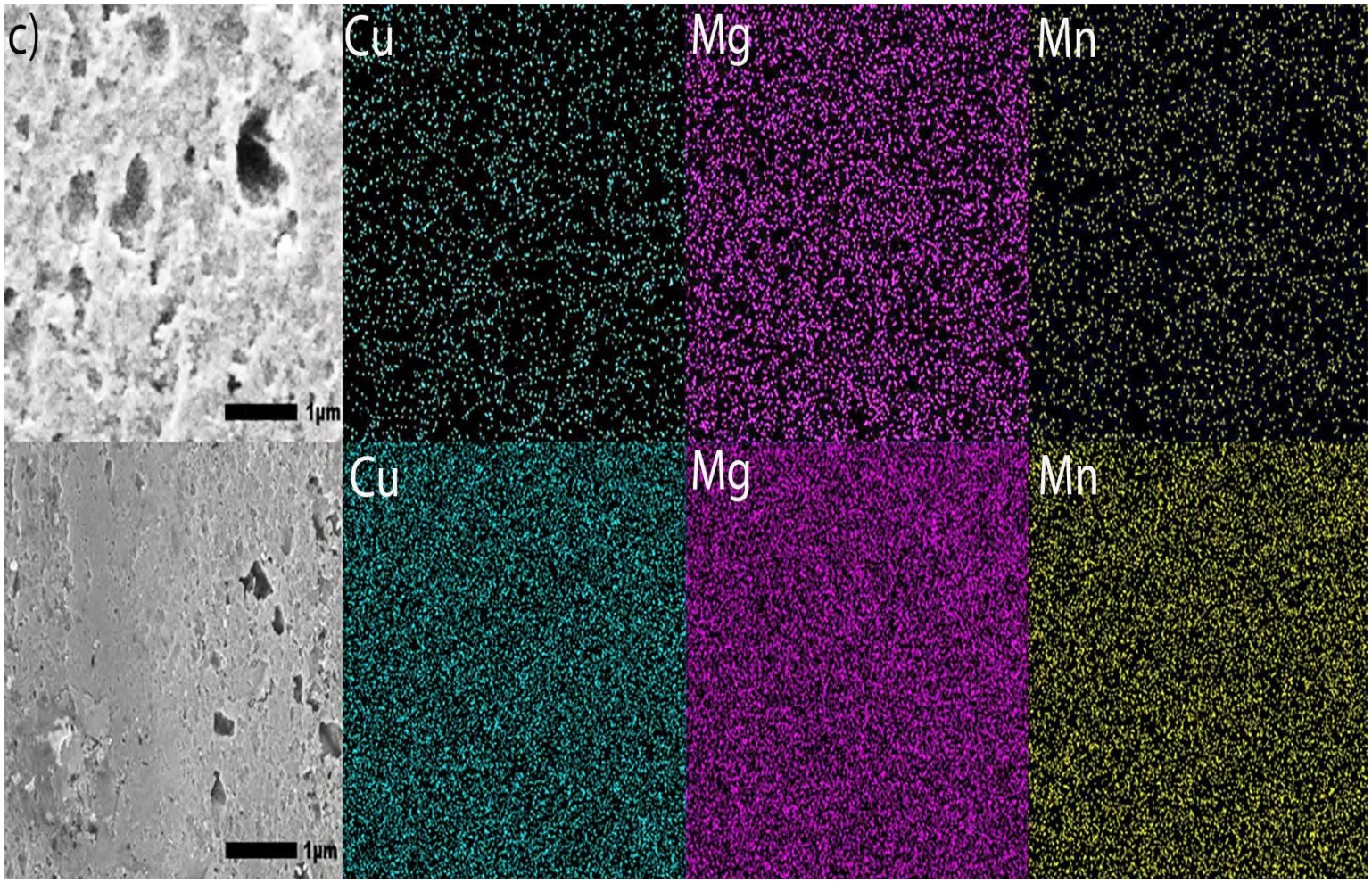

Figure 4.9c SEM images at 30,000x and EDS mapping images of the surface of a specimen anodized for 30 mins in process Base. Images were obtained using 20 kV under LED. The acquisition time was about 45 mins to acquire 200 counts/pixel (top row) and 325 counts/pixel (bottom row). Colors representing elements are as follows: Copper (teal), magnesium (pink), and manganese (yellow).

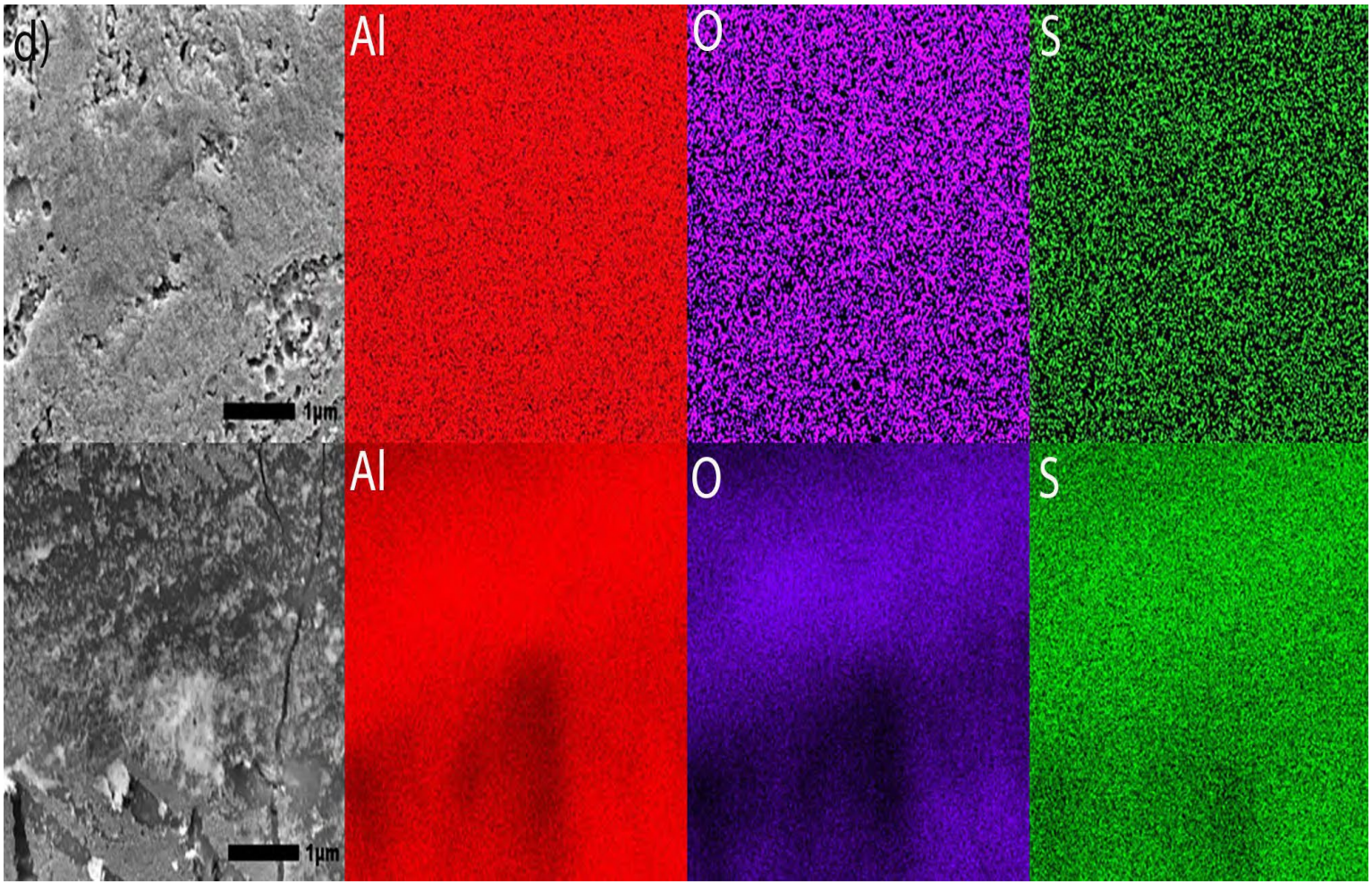

Figure 4.9d SEM images at 30,000x and EDS mapping images of the surface of a specimen anodized for 30 mins in process OS1. Images were obtained using 20 kV under LED. The acquisition time was about 45 mins to acquire 200 counts/pixel (top row) and 325 counts/pixel (bottom row). Colors representing elements are as follows: Aluminum (red), oxygen (purple), and sulfur (green).

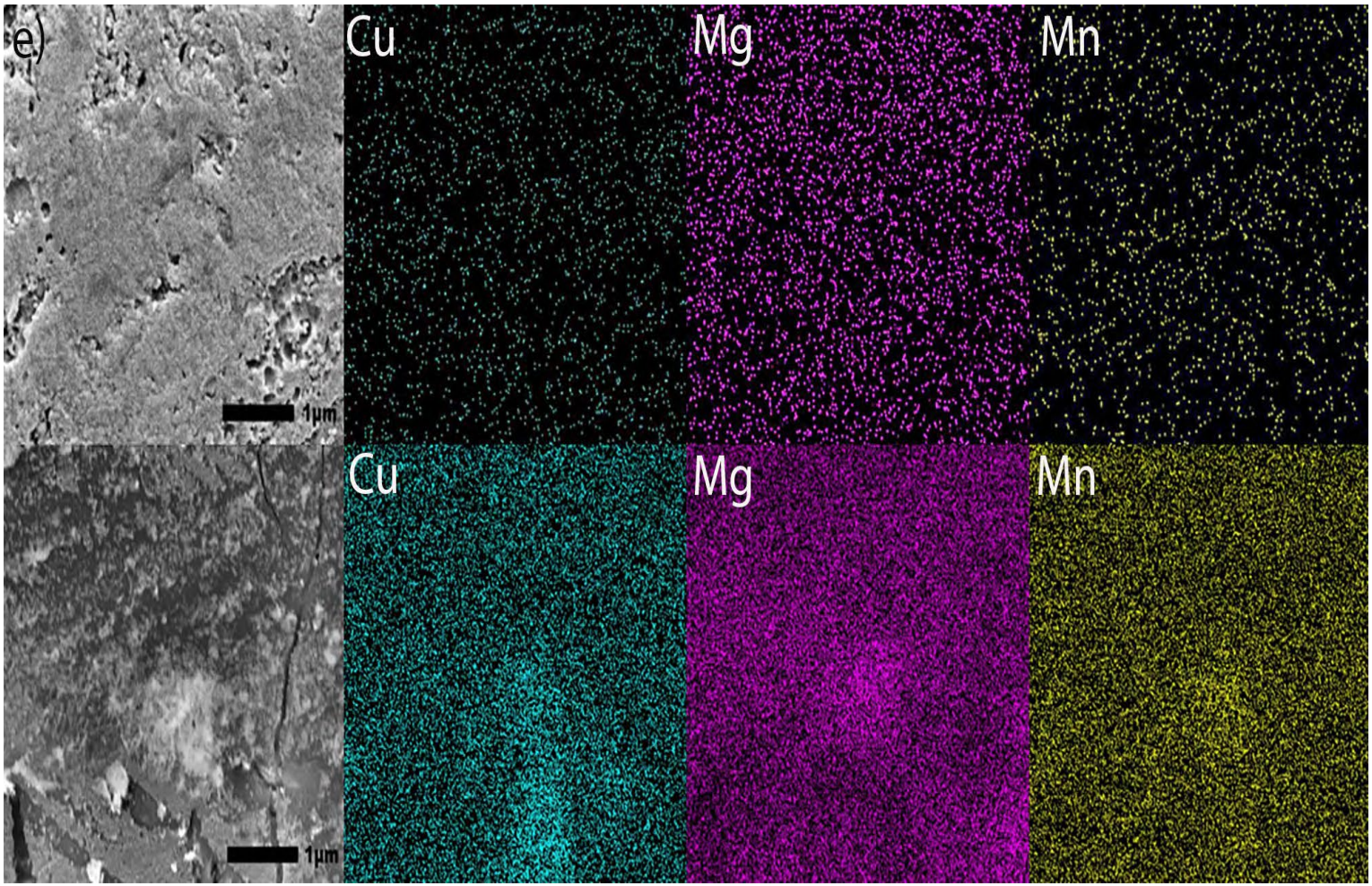

Figure 4.9e SEM images at 30,000x and EDS mapping images of the surface of a specimen anodized for 30 mins in process OS1. Images were obtained using 20 kV under LED. The acquisition time was about 45 mins to acquire 200 counts/pixel (top row) and 325 counts/pixel (bottom row). Colors representing elements are as follows: Copper (teal), magnesium (pink), and manganese (yellow).

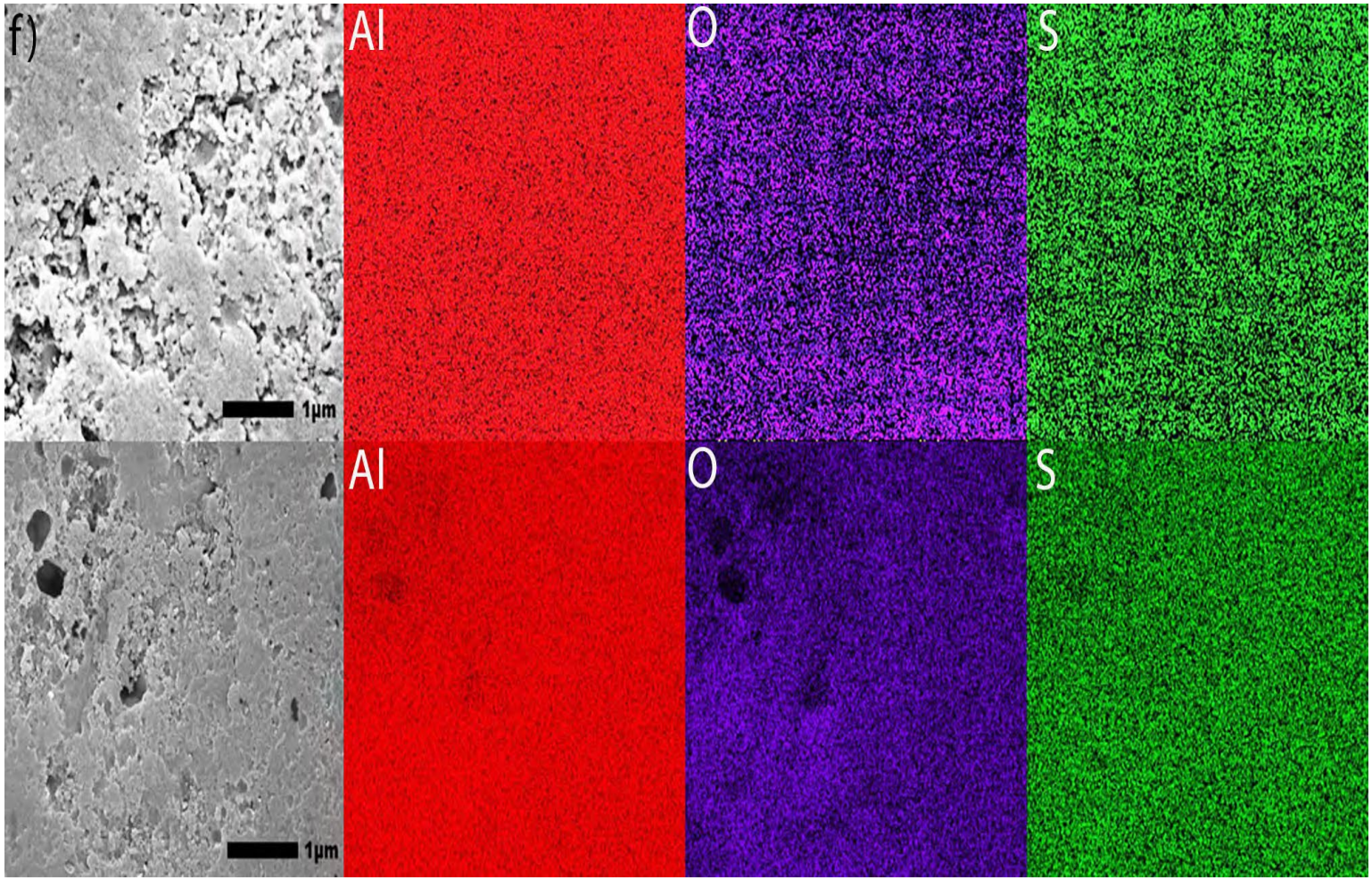

Figure 4.9f SEM images at 30,000x and EDS mapping images of the surface of a specimen anodized for 30 mins in process OS2. Images were obtained using 20 kV under LED. The acquisition time was about 45 mins to acquire 200 counts/pixel (top row) and 325 counts/pixel (bottom row). Colors representing elements are as follows: Aluminum (red), oxygen (purple), and sulfur (green).

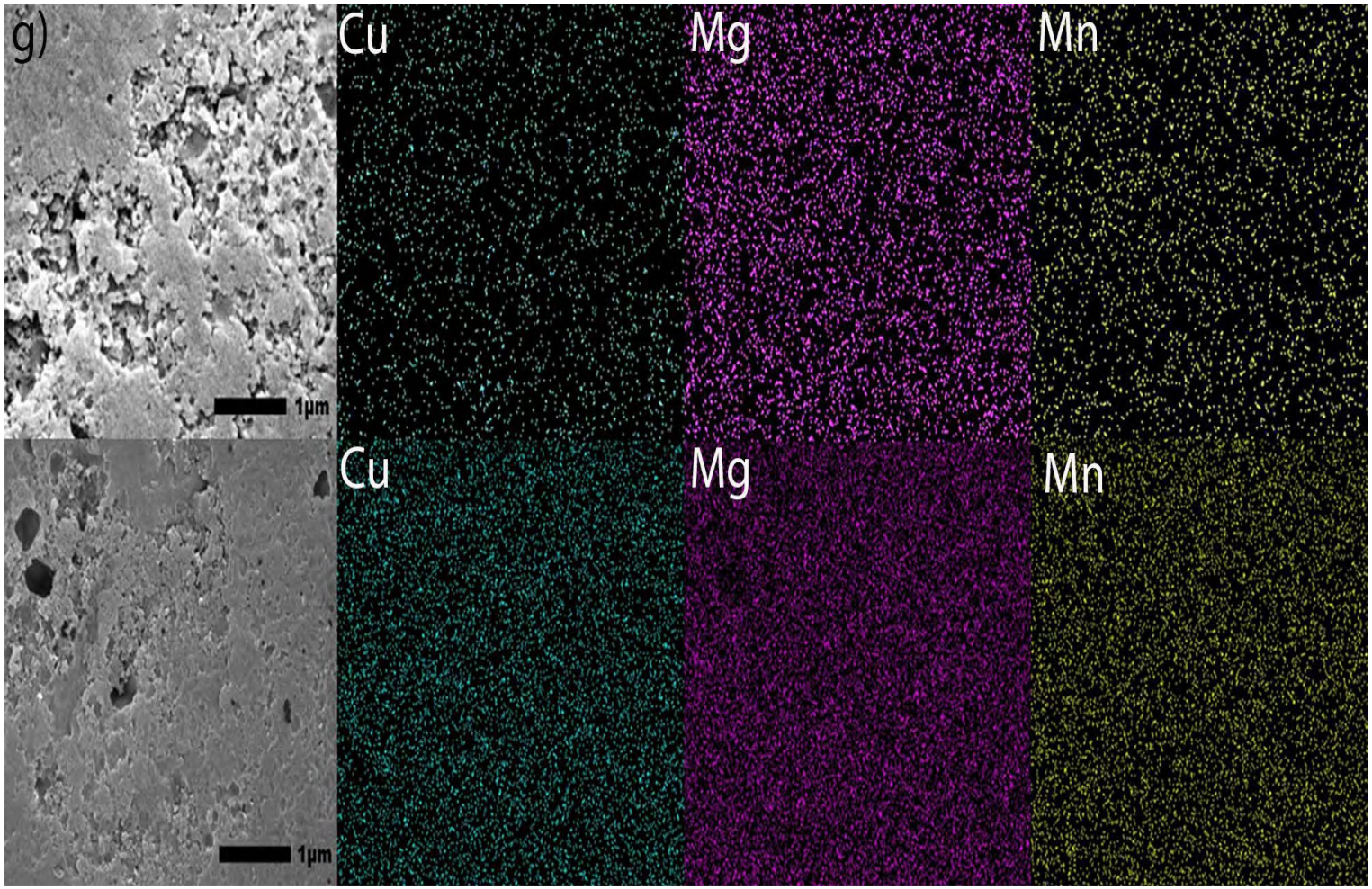

Figure 4.9g SEM images at 30,000x and EDS mapping images of the surface of a specimen anodized for 30 mins in process OS2. Images were obtained using 20 kV under LED. The acquisition time was about 45 mins to acquire 200 counts/pixel (top row) and 325 counts/pixel (bottom row). Colors representing elements are as follows: Copper (teal), magnesium (pink), and manganese (yellow).

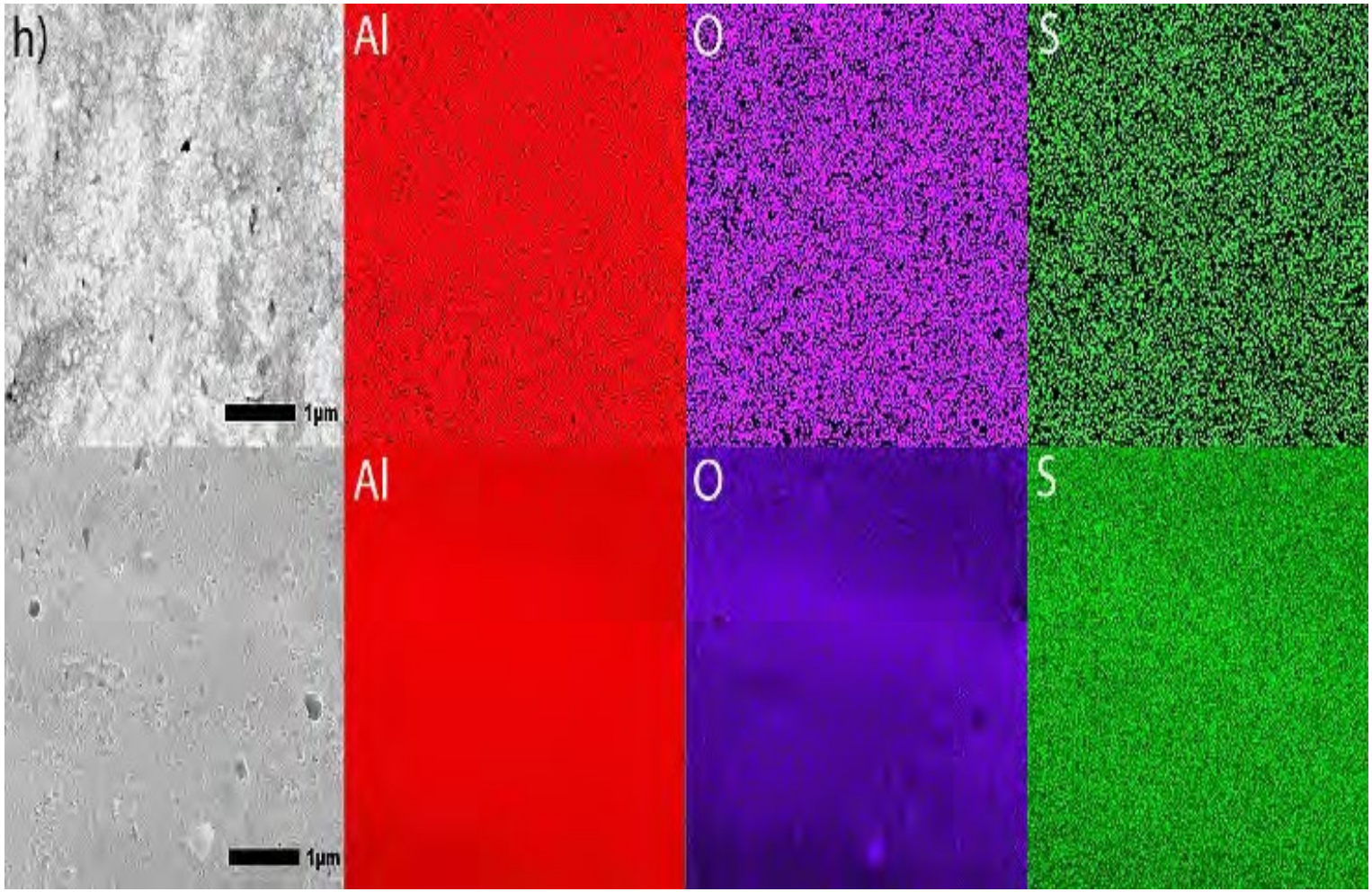

Figure 4.9h SEM images at 30,000x and EDS mapping images of the surface of a specimen anodized for 30 mins in process MS1. Images were obtained using 20 kV under LED. The acquisition time was about 45 mins to acquire 200 counts/pixel (top row) and 325 counts/pixel (bottom row). Colors representing elements are as follows: Aluminum (red), oxygen (purple), and sulfur (green).

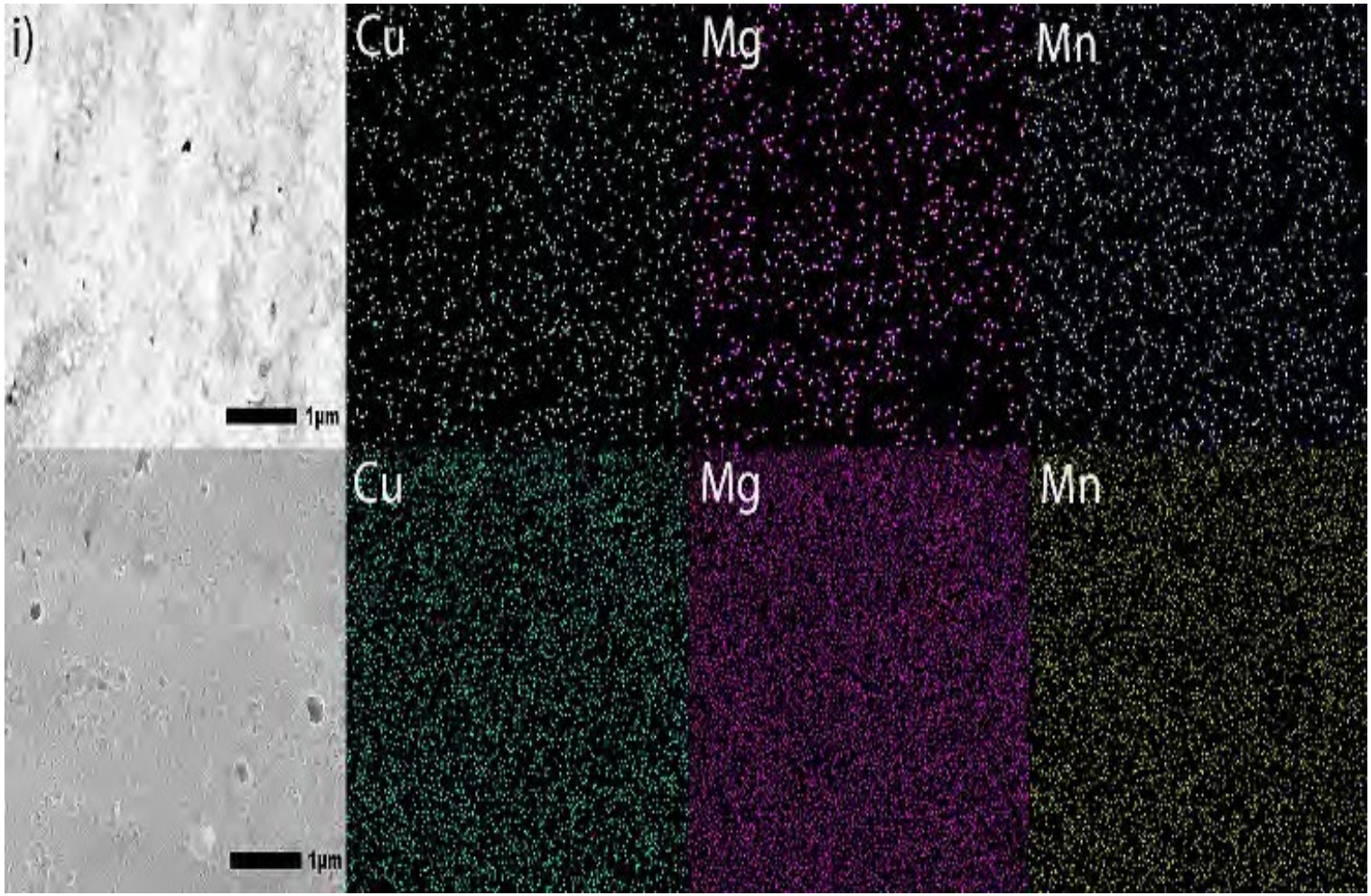

Figure 4.9i SEM images at 30,000x and EDS mapping images of the surface of a specimen anodized for 30 mins in process MS1. Images were obtained using 20 kV under LED. The acquisition time was about 45 mins to acquire 200 counts/pixel (top row) and 325 counts/pixel (bottom row). Colors representing elements are as follows: Copper (teal), magnesium (pink), and manganese (yellow).

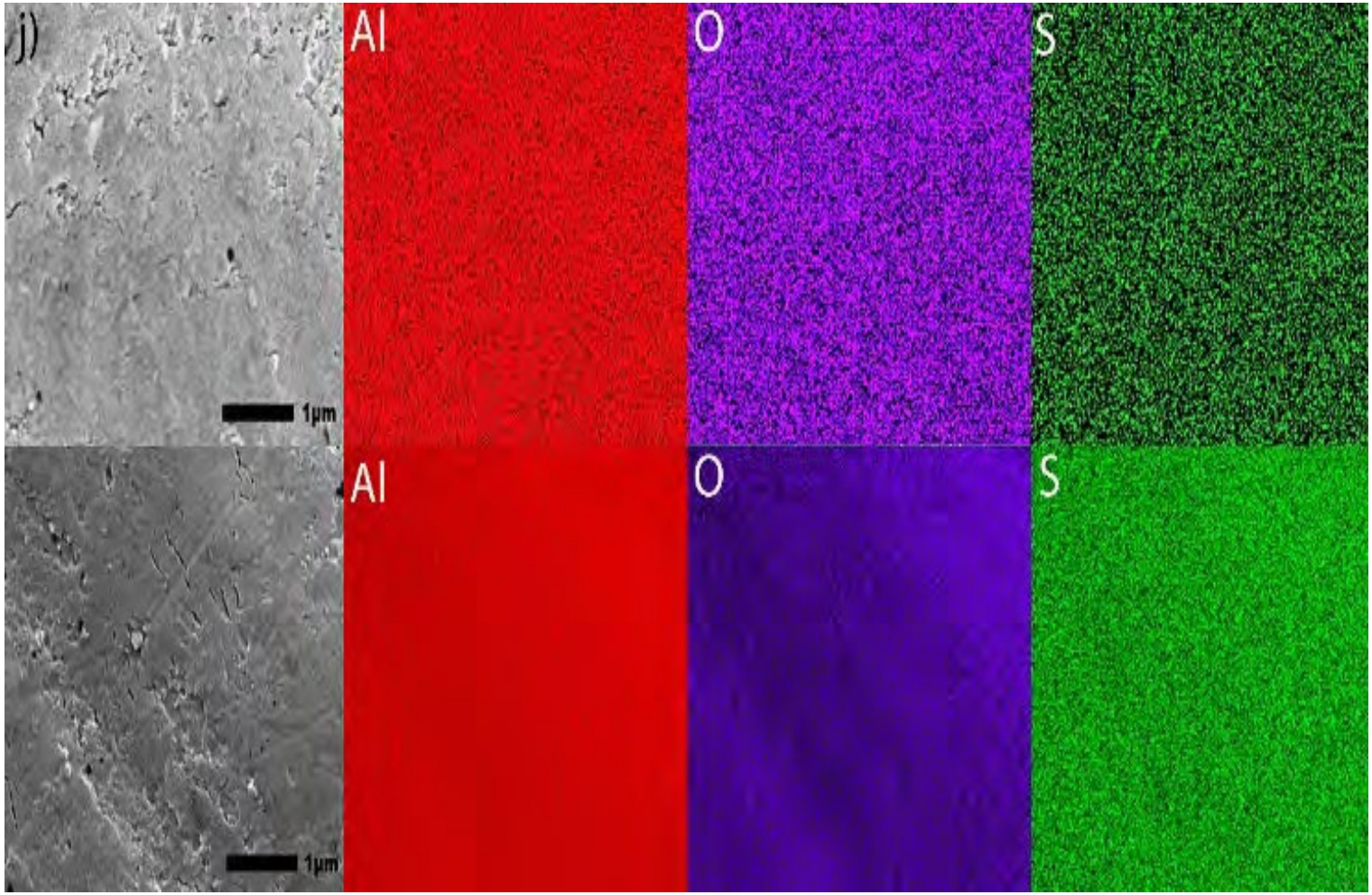

Figure 4.9j SEM images at 30,000x and EDS mapping images of the surface of a specimen anodized for 30 mins in process MS2. Images were obtained using 20 kV under LED. The acquisition time was about 45 mins to acquire 200 counts/pixel (top row) and 325 counts/pixel (bottom row). Colors representing elements are as follows: Aluminum (red), oxygen (purple), and sulfur (green).

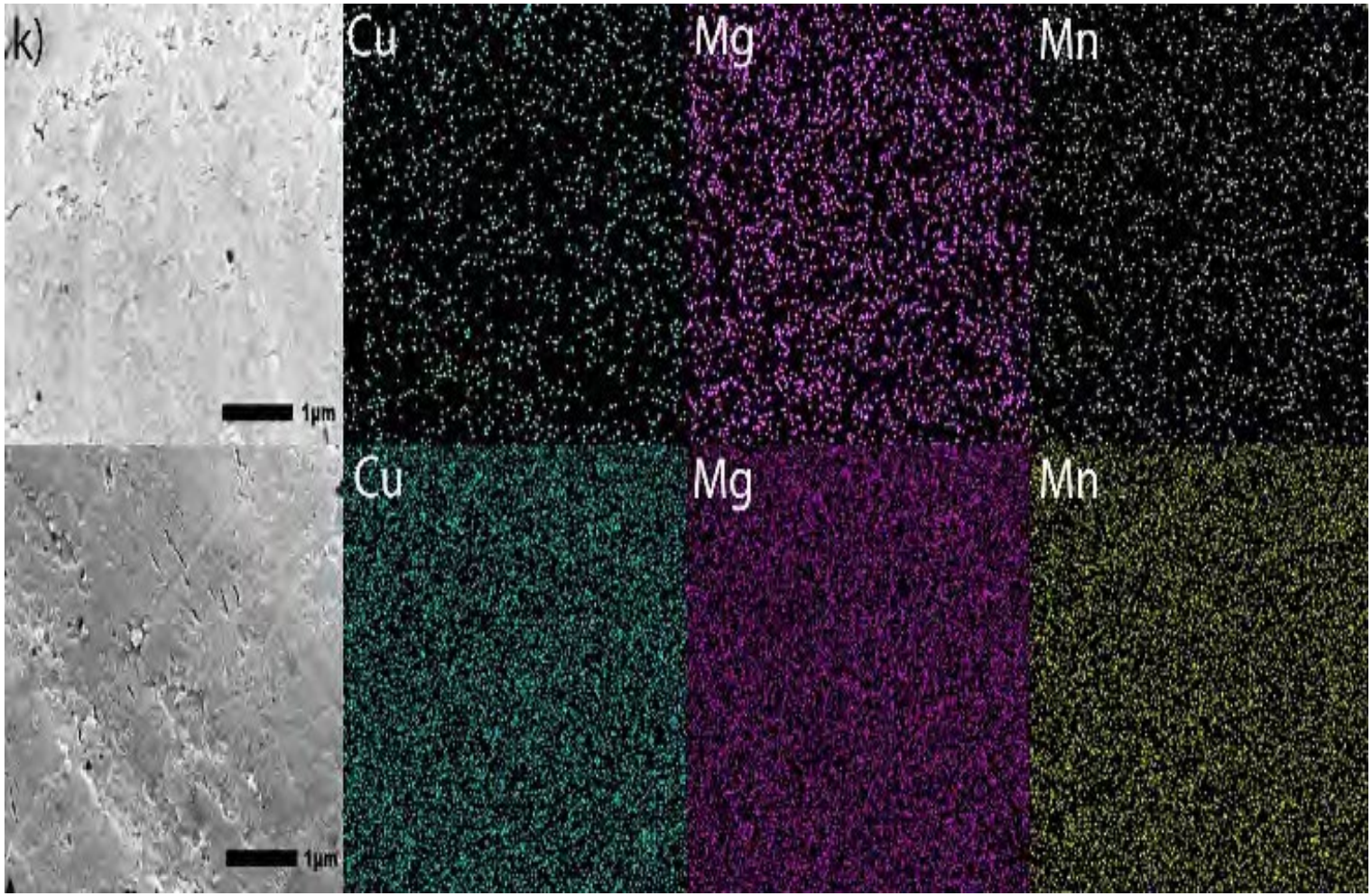

Figure 4.9k SEM images at 30,000x and EDS mapping images of the surface of a specimen anodized for 30 mins in process MS2. Images were obtained using 20 kV under LED. The acquisition time was about 45 mins to acquire 200 counts/pixel (top row) and 325 counts/pixel (bottom row). Colors representing elements are as follows: Copper (teal), magnesium (pink), and manganese (yellow).

Table 4.6 lists the values of the pore diameters, interpore distance and pore density computed from SEM images (100,000x) in **Figure 4.3** with the use of software ImageJ [130].

Pore size measurements are illustrated in **Figure 4.3(a-j)**. Pore density was calculated using Equation (4.7) [94]:

$$N = \frac{2 \times 10^{6}}{\sqrt{3}(D_{int}^{2})} \tag{4.7}$$

where N is the number of pores per unit area in μm^2 and D_{int} is the interpore distance in nm. The average pore diameter increase was 49.9%, with the largest increase 64.4% found in the MS2 process. Pores formed at the beginning of anodization have little or no beveling at the pore wall to the adjacent region. The growth of a pore diameter could be attributed to a higher rate of dissolution around a pore during later stages of processing. The observed dependence of the interpore distance and pore density on the applied initial voltage is consistent with Equation (4.8) [95] for the porosity of anodic aluminum oxides formed in sulfuric acid electrolyte:

$$DD_{iiiiii} = 12.1 + 1.99 \cdot U \qquad \text{for} \qquad 3 \leq U \leq 18 \tag{4.8}$$

where U is the applied voltage in V. The results of statistical analysis presented in **Table 4.6** demonstrate that a difference between data on the diameter of pores formed during 30 mins, interpore distance and pore density in coatings formed in Group 1 and Group 2 processes is statistically significant as $FF > FF_{0.05}$ and $0.05 > PP_{0.05}$. A difference in measurements of pore diameters in coatings formed in Group 1 and Group 2 processes during 10 mins is not statistically significant. However, a difference between the measurements of pore diameters in all coatings formed during 10 mins and 30 mins of anodization is statistically significant as $FF > FF_{0.05}$ and $0.05 > PP_{0.05}$.

Table 4.6. Pore Diameter (nm), Interpore Separation (nm) and Pore Density ($1/\mu m^2$) in Coatings Formed by Anodization Over 10 mins and 30 mins in Base, OS1, OS2, MS1 and MS2 Processes. Values were Computed from High-magnification SEM images (100,000×). Posted in **Figure 4.3,** computations were conducted with software ImageJ [59Statistical Analysis of Data Between Processes in Group 1 (Base, OS1, OS2) and Group 2 (M21, MS2) for Pore Diameter (10 & 30 mins), Interpore Separation and Pore Density is Listed Below. Statistical Analysis of Data Between Processes in 10 mins and 30 Mins for the Pore Diameter is also Listed Below

Process	**Pore Diameter, nm, 10 mins**	**Pore Diameter, nm, 30 mins**	**Interpore Separation, nm, 30 mins**	**Pore Density, $1/\mu m^2$, 30 mins**
Base	18.3 ± 4.8	33.4 ± 9.2	43.34 ± 0.57	615.2 ± 16.2
OS1	16.5 ± 4.1	26.7 ± 6.7	23.64 ± 0.70	2067.9 ± 120.4
OS2	18.4 ± 6.4	29.3 ± 7.2	39.16 ± 0.34	753.1 ± 12.05
MS1	17.7 ± 5.3	24.9 ± 6.1	22.85 ± 0.85	2214.7 ± 161.6
MS2	17.9 ± 4.8	34.9 ± 5.6	23.05 ± 0.98	2176.6 ± 179.3

Pore Diameter – 10 mins					
Groups	Count	Average	$P_{0.05}$	F	$F_{0.05}$
Group 1	217	18.2 ± 10.5	8.6×10^{-1}	0.03	3.9
Group 2	160	17.7 ± 9.0			

Pore Diameter – 30 mins					
Groups	Count	Average	$P_{0.05}$	F	$F_{0.05}$
Group 1	192	28.0 ± 9.6	1.0×10^{-2}	6.2	3.9
Group 2	120	32.1 ± 8.5			

Pore Diameter – 10 mins vs 30 mins					
Groups	Count	Average	$P_{0.05}$	F	$F_{0.05}$
10 mins	390	17.9 ± 8.9	3.6×10^{-12}	50.1	3.9
30 mins	312	29.6 ± 9.5			

Interpore Distance					
Groups	Count	Average	$P_{0.05}$	F	$F_{0.05}$
Group 1	9	35.4 ± 9.0	5.0×10^{-3}	11.1	4.7
Group 2	6	22.9 ± 1.0			

Pore Density					
Groups	Count	Average	$P_{0.05}$	F	$F_{0.05}$
Group 1	9	1146 ± 700	3.0×10^{-3}	12.8	4.7
Group 2	6	2203 ± 188			

4.3.1.7 XRD Patterns of anodized specimens. XRD of anodic coatings formed in Base, OS1, OS2, MS1 and MS2 processes over 10 mins and 30 mins are shown in **Figure 4.10**. Measurements were conducted at an incident angle of 2° using a grazing technique. For comparison, XRD of untreated specimens are also shown in **Figure 4.10**. According to the instrument peak profiles, eight peaks in XRD patterns corresponded to the aluminum face-centered-cubic (fcc) crystal structure. However, shifts and changes in the intensity of diffraction peaks of aluminum oxides were observed in diffraction patterns collected on specimens anodized for 10 mins (**Figure 4.10(a)**) and 30 mins (**Figure 4.10(b)**). It indicates that amorphous aluminum oxides were formed in the anodizing process.

Compared to the untreated specimen, anodization changed the position, width, and intensities of peaks in diffraction patterns. Lattice constants of the fcc structure of anodized specimens are reported in **Figure 4.11(a)** and was computed for both types of XRD measurements from Equation (4.9) [96]:

$$d_{hkl} = \frac{a}{\sqrt{(h^2+kk^2+ ll^2)}} \tag{4.9}$$

where d_{hkl} is the distance between the adjacent lattice planes in the fcc structure for the peak Bragg angle in nm, a is the lattice constant/parameter in nm, and $\boldsymbol{h}kkkk$ are the Miller indices for the lattice planes. Results of these calculations presented in **Figure 4.11(a)** were averaged over all fcc peaks in the diffraction pattern and then averaged over three specimens.

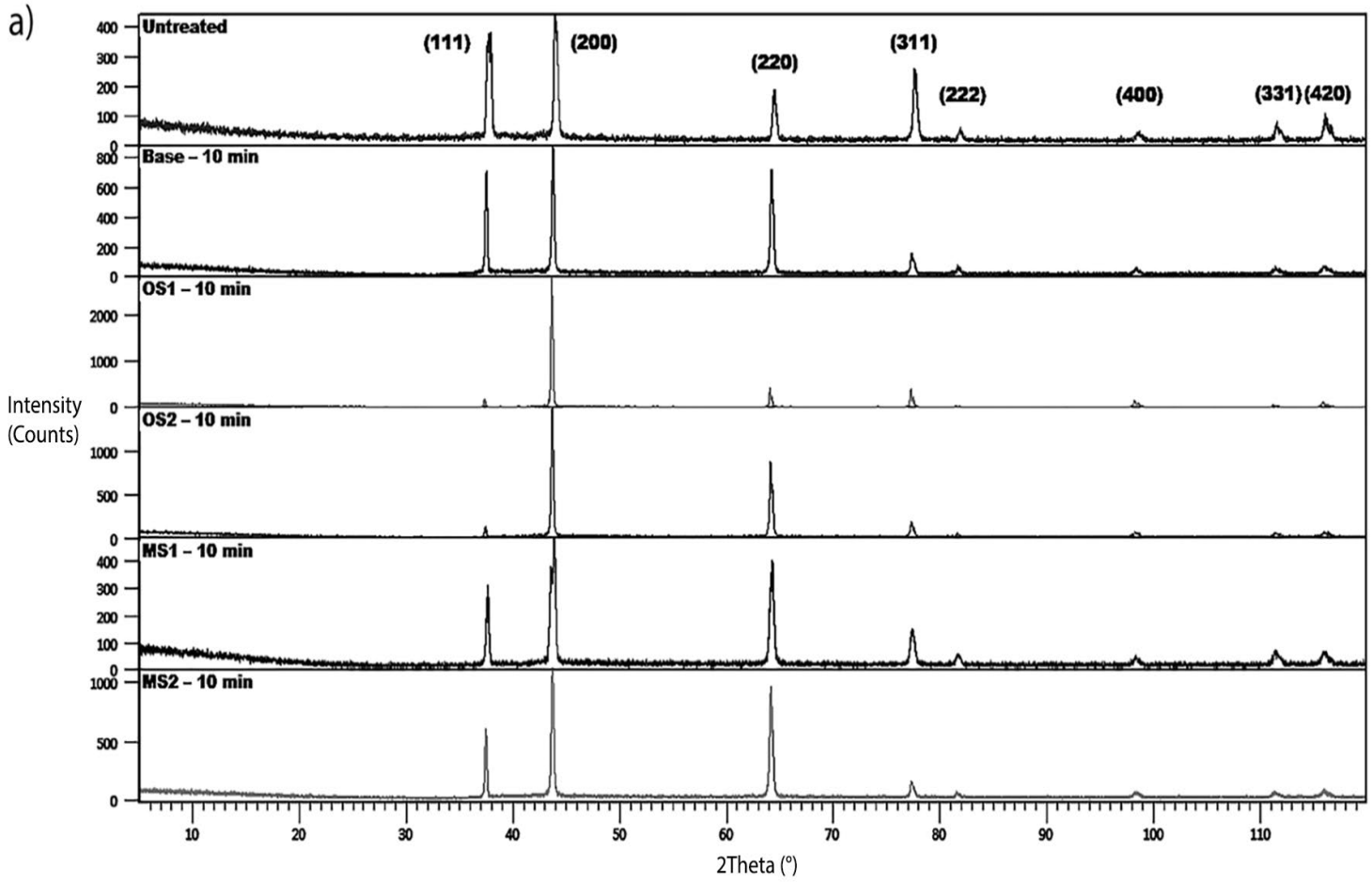

Figure 4.10a XRD of the untreated specimen alloy and specimens anodized in Base, OS1, OS2, MS1, MS2 process for 10 min (ramping period of stepwise processes). Measurements collected at an incident angle of 2^0 using a grazing technique.

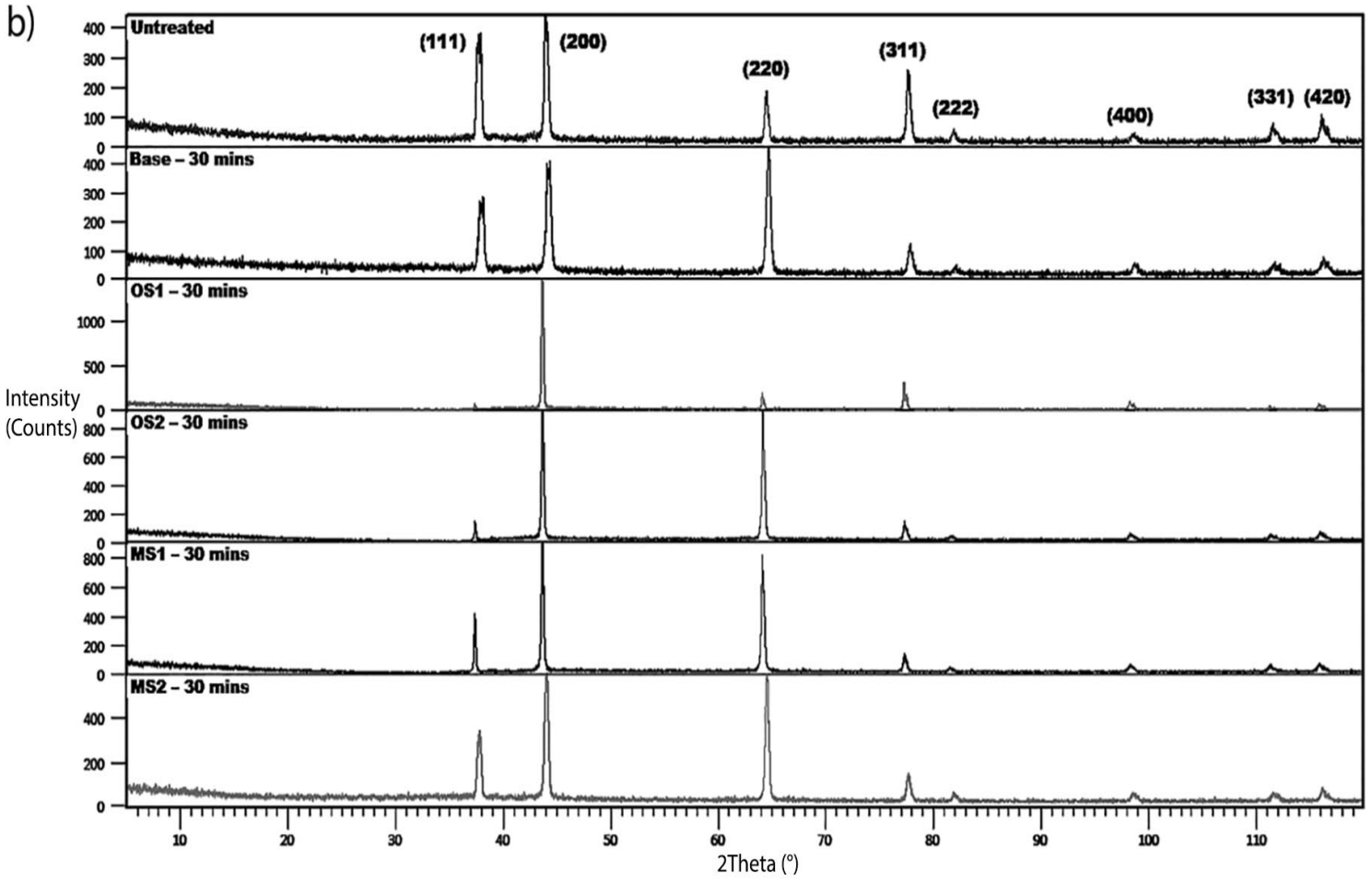

Figure 4.10b XRD of the untreated specimen alloy and specimens anodized in Base, OS1, OS2, MS1, MS2 process for 30 min. Measurements collected at an incident angle of 2^0 using a grazing technique.

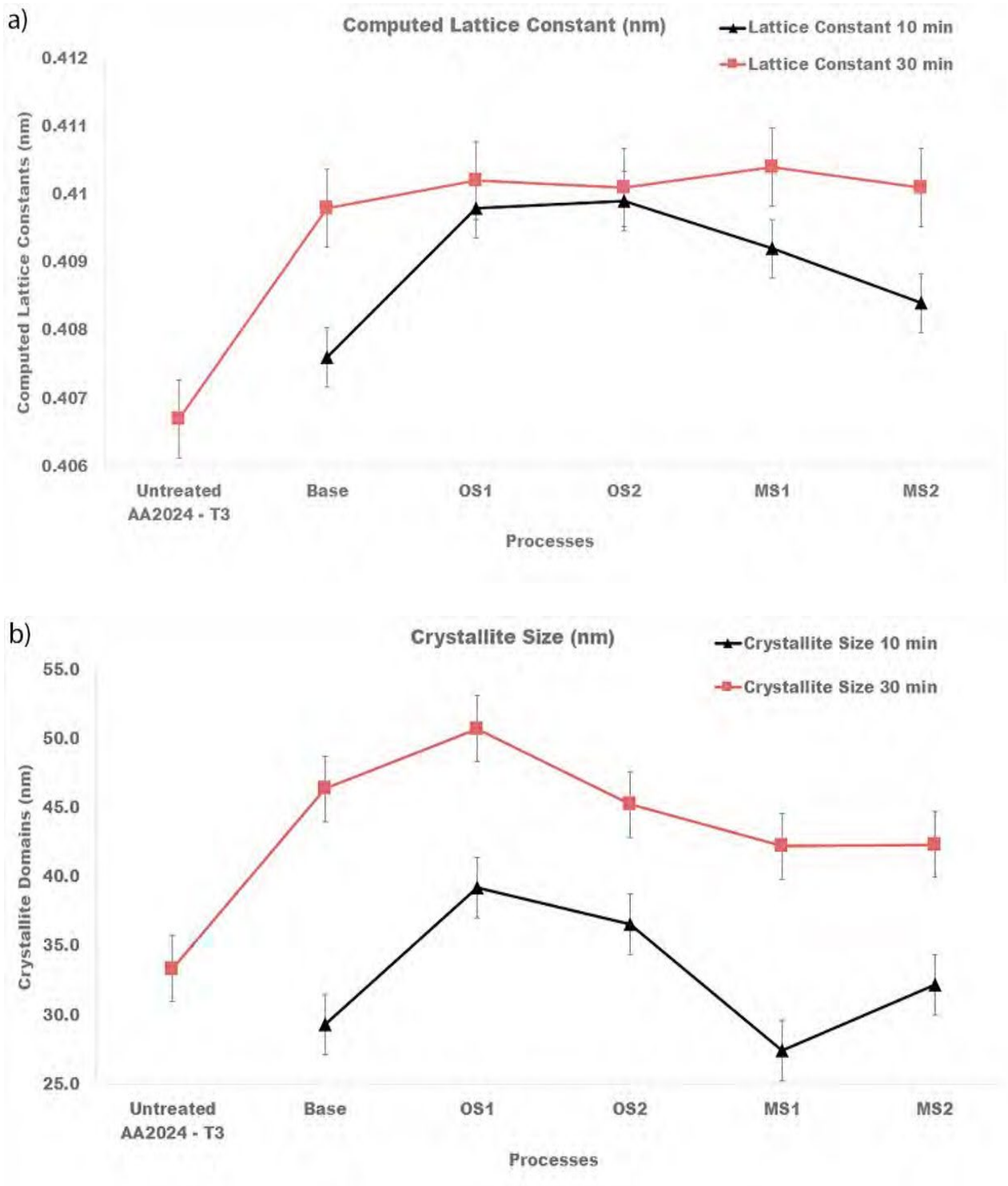

Figure 4.11(a-b) Computed (a) lattice constants of the FCC structure of crystallites and (b) sizes of crystalline domains for specimens anodized in Base, OS1, OS2, MS1, MS2 process for 10 min (ramping period of stepwise processes), and for 30 min. Reported values were averaged over all peaks identified in the diffraction pattern and then averaged over three specimens.

Plots in **Figure 11(a)** show that anodization increased the lattice constants of crystallites and that they are larger for the entire process. The Scherrer equation, Equation. (4.10) [96], was taken to compute the size of coherently scattering crystalline domains from the peak width:

$$LL = \frac{KKKK}{\beta\beta_{hkkll}cccccc(\theta\theta_{hkkll})} \tag{4.10}$$

Where L is the mean size of the crystalline domains in nm, $KK = 0.9$ is the shape factor, λ=0.15406 nm is the wavelength of the CuKα radiation, $\theta\theta_{hkkll}$ is the peak Bragg angle in radians, $\beta\beta_{hkkll}$ is the corrected value of the width at half-maximum (FWHM) of the peak in radians, and hkl are the Miller indices of the crystallographic planes. The measured broadening, Equation (4.11) [96], of a peak was corrected by the data on the instrumental peak broadening as:

$$\beta\beta_{hkkll} = \left(\beta\beta^2_{mm,hkkll} - \beta\beta^2_{iiiiiii,hkkll}\right)^{1/2} \tag{4.11}$$

where $\beta_{m,hkl}$ (rad) is the measured FWHM, and $\beta_{inst,hkl}$ (rad) is the instrumental FWHM measured using the NIST standard [118]. Results of these calculations shown in **Figure 4.11(b)** were averaged over all peaks identified in the diffraction pattern and then averaged over three specimens. As can be seen from **Figure 4.11(b)**, the size of crystalline domains increased with longer anodization time.

4.3.2 Process efficiency

Table 4.7 reports the values of an applied voltage needed to maintain the designed current density in processes Base, OS1, OS2, MS1 and MS2. Differences between the charge transferred per step

and the overall charge transferred listed in **Tables 4.2** and ~~**Table** **4.7**~~ are lying within several percentages as the accuracy of maintaining the constant anodizing current was about 1%. The values of the applied voltage needed to initiate anodization was lower in processes OS1, MS1 and MS2 (**Table 4.7**).

Table 4.7. Data on the Applied Anodizing Current, Initial and Final Voltage, and Measurements of Charge for Each Step of Base, OS1, OS2, MS1 and MS2 processes. The Presented Values were Averaged over Three Runs

Process	Mins	Amperage, A	Charge, C	Initial Voltage, V	Final Voltage, V
Base	30	17	29800.0 ± 2332.2	15.7 ± 0.5	16.0 ± 0.2
OS1	10	3	1710.0 ± 98.1	5.8 ± 0.2	9.0 ± 0.3
	20	17	19755.0 ± 347.6	15.8 ± 0.2	16.3 ± 0.6
OS2	10	11	6005.0 ± 97.9	13.6 ± 0.4	14.6 ± 0.1
	20	17	18852.0 ± 282.4	15.5 ± 0.2	17.3 ± 0.2
MS1	2	3	333.0 ± 27.3	5.4 ± 0.2	7.4 ± 0.5
	2	4	444.0 ± 25.7	8.6 ± 0.2	8.9 ± 0.6
	2	5	563.0 ± 16.2	9.2 ± 0.2	9.5 ± 0.3
	2	5	598.0 ± 36.8	9.8 ± 0.1	10.2 ± 0.1
	2	6	716.0 ± 94.2	10.5 ± 0.2	10.8 ± 0.1
	20	17	20165.0 ± 266.9	14.1 ± 0.1	15.9 ± 0.1
MS2	2	3	339.0 ± 16.8	5.5 ± 0.5	7.5 ± 0.7
	2	6	705.0 ± 22.9	9.3 ± 0.5	10 ± 0.6
	2	9	998 .0 ± 63.5	11.2 ± 0.4	11.5 ± 0.4
	2	12	1410.0 ± 84.2	13.0 ± 0.7	13.2 ± 0.6
	2	15	1715.0 ± 114.2	13.5 ± 0.7	14.1 ± 0.7
	20	17	19965.0 ± 201.3	14.4 ± 0.4	16.0 ± 0.4

Figure 4.12 illustrates the coating growth rates, μm/min, computed for 10 and 30 mins of anodization for Base, OS1, OS2, MS1 and MS2 processes. The presented results demonstrate that utilizing multistep ramping of current density at the beginning of anodization allow for a higher growth rate over the 10-30 min period of anodization as well as for the overall growth rate. In particular, the overall growth rates in multistep processes MS1 and MS2 were greater than that of

single step ramping processes and greater than that of Base process by 11.3% and 14.5%, respectively. **Table 4.8** presents data on the charge transferred per unit thickness of an anodic coating, C/µm, that was computed for different time intervals as well as over the entire 30 min period of anodization for processes Base, OS1, OS2, MS1 and MS2.

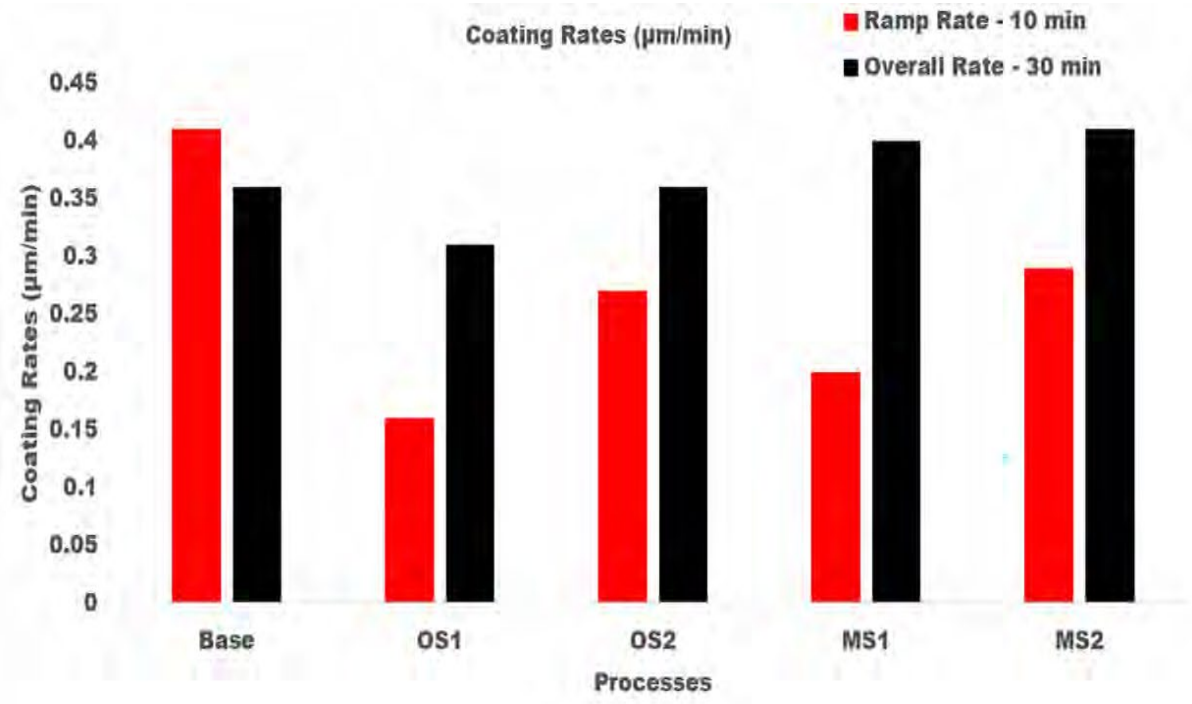

Figure 4.12 Coating growth rates, µm/min, in processes Base, OS1, OS2, MS1, and MS2. Anodizing times were 10 mins and 30 mins. Overall growth rates are shown on the right, black column. Multistep processes, MS1 and MS2, provide the highest overall growth rates.

Table 4.8. Charge Transferred per Unit Thickness of an Anodic Coating, C/μm. The Samples were Taken at 2-minute Intervals up to and Including 10 Minutes, and at the End of the Process, 30 Minutes for Processes Base, OS1, OS2, MS1 and MS2. Statistical Analysis of Data Between Processes in Group 1 (Base, OS1, OS2) and Group 2 (M21, MS2) for the Overall Process is Listed Below

Charge per Unit Thickness (C/μm)							
Process Time, Min	**0 to 2**	**2 to 4**	**4 to 6**	**6 to 8**	**8 to 10**	**10 to 30**	**Overall**
Base	2040.0	5100.0	3400.0	2040.0	1854.5	3000.0	2733.9
OS1	855.0	1140.0	855.0	1710.0	1140.0	2565.6	2308.1
OS2	1501.3	3002.5	1501.3	6005.0	2402.0	2356.5	2323.1
MS1	1110.7	888.6	804.3	2993.5	2386.7	1977.0	1870.5
MS2	1695.0	783.3	2495.0	2014.3	2450.0	2058.2	1994.6
Groups	Count	Average	$P_{0.05}$	F	$F_{0.05}$		
Group 1	9	2455 ± 227	1.0×10^{-4}	30.3	4.7		
Group 2	6	1920 ± 74					

Results presented in **Table 4.8** show that all stepwise processes reduced the overall values of the charge transferred per unit thickness. In particular, it was reduced by 37.5% and 31.3%, respectively, for multistep processes MS1 and MS2. The results of statistical analysis presented in **Table 4.8** demonstrate that a difference between the influence of anodizing processes in Group 1 and Group 2 on the charge per unit thickness is statistically significant as $F > F_{0.05}$ and $0.05 > P_{0.05}$.

Table 4.9 presents anodic coating efficiency, average voltage used, and work required to transfer an electric charge during anodization for processes Base, OS1, OS2, MS1 and MS2. Work was computed using the measurements of voltage presented in **Table 4.7** and anodic process efficiency, η_{ox}, was computed using Equation (4.5).

Results reported in **Table 4.9** demonstrate that stepwise processes reduce the work and applied voltage needed to build an anodic coating and thereby raise the anodization efficiency. Compared to Base, processes MS1 and MS2 are more efficient by 19.7% and 28.2%, respectively.

The results of statistical analysis presented in **Table 4.9** demonstrate that a difference between the influence of anodizing processes in Group 1 and Group 2 on the anodic coating efficiency and average voltage are statistically significant as $FF > FF_{0.05}$ and $0.05 > PP_{0.05}$. However, a difference in data on the work between processes in Groups 1 and 2 is not statistically significant.

Table 4.9. Coating Efficiency, η_{ox}, of Anodization, Average Voltage, V, and Work, kJ, Calculated for Base, OS1, OS2, MS1, and MS2 Processes. Statistical Analysis of Data Between Processes in Group 1 (Base, OS1, OS2) and Group 2 (M21, MS2) for the Overall Process is Listed Below

Process	**Coating Efficiency, (ηox)**	**Average Voltage, V**	**Work (kJ)**
Base	0.201 ± 0.006	15.9 ± 0.2	14334 ± 152
OS1	0.233 ± 0.005	13.2 ± 0.2	10475 ± 219
OS2	0.211 ± 0.001	15.6 ± 0.1	12926 ± 127
MS1	0.245 ± 0.011	13.0 ± 0.1	10862 ± 85
MS2	0.267 ± 0.003	13.7 ± 0.4	12039 ± 299

Efficiency					
Groups	Count	Average	$P_{0.05}$	F	$F_{0.05}$
Group 1	9	0.215 ± 0.015	1.7×10^{-5}	26.8	4.7
Group 2	6	0.256 ± 0.015			

Average Voltage					
Groups	Count	Average	$P_{0.05}$	F	$F_{0.05}$
Group 1	9	14.9 ± 1.3	2.0×10^{-2}	6.5	4.7
Group 2	6	13.3 ± 0.7			

Work					
Groups	Count	Average	$P_{0.05}$	F	$F_{0.05}$
Group 1	9	12578 ± 1700	1.5×10^{-1C}	2.3	4.7
Group 2	6	11450 ± 796			

4.4 Conclusions

The presented results demonstrated that starting anodization at a low voltage and then slowly ramping current density increased the growth rate, structure, and service properties of an anodic coating on AA2024 – T3 alloy. Five anodizing processes in a sulfuric acid bath were studied: a conventional Base process with a constant applied current density and ramping processes, OS1, OS2, MS1, MS2, applying different magnitudes of current density in either one or five steps. Increasing the number of ramping steps with an incremental rise in current density in processes MS1 and MS2 lowered the oxygen infusion into the coating (Al/O ratio), raised the coating growth rate, reduced the coating porosity, and enhanced the coating abrasion resistance and hardness. Overall, processes MS1 and MS2 were 11.3% and 14.5% faster at producing 1 μm of coating per minute compared to the Base process and formed almost the same thickness in 33% less time. Both multistep ramp processes, MS1 and MS2, produced a thicker coating compared to single-step ramp processes. Multistep processes MS1 and MS2 were, respectively, 19.7% and 28.2% more efficient in building an anodic coating compared to the Base process.

In our previous work [104] we demonstrated that it was possible to improve the properties of anodized AA7075 – T6 by gradually increasing the current density during the ramp stage. That result taken together with the presented data on anodization of AA2024 – T3 show that benefits of multistep anodization processes are not sensitive to the alloy composition. We therefore expect that the use of multistep anodization with a gradual increase in an applied current density would allow for the development of more efficient anodization processes for other aluminum alloys.

CHAPTER 5

CONCLUSIONS

Anodization processes of aerospace aluminum alloys with a focus on alloys 7075 – T6 and 2024 – T3 have been discussed and explored. The most promising methods of anodization leading to enhanced coating performance and morphology were reviewed in the literature. The method of varying state variables of the anodization process, in particular current density, A/m^2, and potential, V, were also discussed. The understanding of this variable manipulation and respective outcomes were fundamental to enhance the anodization process and to make the process more reliable to process these difficult alloys.

Further discussion revealed the industry wide issue in processing wrought aluminum alloys in particular 7075 – T6 and 2024 – T3. These are both choice alloys for aerospace and automotive industries, however, they anodize poorly and exhibit vast differences in electrochemical behavior from one another. The aerospace industry has very strict guidelines on how to process these alloys, which limits the selection of temperatures ranges, electrolyte types and preprocessing methods as used in academia. This is becoming a pressing issue as technological advances in our aircrafts and shuttle allow for exploration into more stressful environments, space, deep sea, etc., the need for reliable processes of these alloys is imminent.

Both alloys behave very differently in the anodizing process, and this difference begins at the very first second current is applied as nonaluminum ions in the bulk alloy migrate to the forming anodic film causing processing issues. AA7075-T6 uses zinc as its major alloying element and AA2024-T3 uses copper as its major alloying element. This is significant as these elements cause two types of issues to anodizing aluminum. First, these elements create surface capacitance

near bulk aluminum in the alloy and second, these elements migrate to different locations during anodizing, causing very different but catastrophic defects in the process and/or in the service life. Zinc piles at the interface between forming anodic oxide and bulk 7075-T6 causing delamination, stress cracking and adhesion issues. Copper will migrate throughout the entire coating, interface and surface of AA2024-T3. Copper is problematic as it leads to large reductions in coating rates and increases in electrical resistance due to oxygen gas presence. This ultimately leads to heat and the development of porous coatings. As both alloys behave differently and produce very different defects, it was imperative to explore multistepped anodization on both alloys to understand how manipulating electrical parameters enhances or reduces process efficiency and performance characteristics of anodic film.

By using multiple steps, 4x or more, within the ramping portion of the process, higher current densities can be used at the end of the process without the risk of burning and other coating deformations. Studies have shown that higher potential values and current densities have been used to increase pore diameter and interpore spacing [10,69], and lower amounts of potential can mitigate burning and powdery films [70,71]. Manipulation of potential and current density by varying is used in some applications like creating nanopores and carbon nanotubes or coating for abrasion resistance. Studies on varying current densities throughout the process and specifically at the onset of the process are limited. Some studies vary voltage throughout the entire process or anodize in specialty additives which are not allowable in the aerospace industry. Therefore, utilizing the practice of varying current density, an allowable adjustable parameter in Type II anodizing, for anodizing wrought aluminum alloys has a purpose to enhance the efficiency and performance while reducing the reject rate during processing. Two studies were performed to review and analyze the effects of multistep anodization on two difficult alloys to anodize, AA7075-T6 and AA2024-T3.

The first study, **Multistep Anodization of 7075-T6 Aluminum Alloy,** was to understand the impact of varying current density on the morphology and surface characteristics of anodic films on AA7075-T6. Four regimes were chosen, each with increasing variations during the ramp phase of the process. Processes that utilized less voltage at the onset allowed heat to dissipate more readily, thereby suppressing the formation of burns and rejects. Conventional processing had much slower rates of coating formation despite higher voltage potential and resulted in burned anodic film, which is a result of overheating. An interesting finding was processes that had more steps in the ramp had lower levels of oxygen in the films. This is related to the amount of nonaluminum ions in the film. SEM images illustrated the abundance of cracks and voids in the coating on films produced by the conventional processes, whereas multistepped processes provide intact and smooth films.

Using results from the previous study, regimes of low voltage stepped ramps and normal voltage stepped ramps were chosen to process AA2024-T3 in a new study, **Effect of Current Density Ramping on the Growth Rate and Structure of AA2024-T3**. A focus on the ramp portion of the process and the ramping influence on the overall process was analyzed. Ramping allows for faster rates of coating at the same current density and less voltage later in the process when compared to conventional processing. Coating rates were faster in multistepped processing and overall performance characteristics were improved. The most undulated and porous films were produced by conventional processes and had far more presence of nonaluminum ions when compared to coatings produced by multistepped processes, as their coatings were smooth and had no porosity.

Data shows that processes that incorporating multiple, incremental steps of current density provide coatings that perform better in terms of hardness and wear resistance and more efficient in terms of the amount of potential needed to form anodic coating. This was seen in both alloys,

AA2024-T3 and AA7075-T6. Processes with more steps during the ramps (7075 - R3, R4), (2024 - MS1, MS2), had significantly less zinc (7075) and copper (2024), which ultimately reduced the amount of oxygen in the coating. Processes that utilized multistepped ramps, increase the growth rate substantially and utilized far less charge than conventional processes, which makes multistepped processes more energy efficient.

Visually, the coatings of both studies were similar, with the multi-stepped ramping processes exhibiting a more compact and nonporous coating. The base line processes R1 and Base both suffered from large amounts of dissolution and oxygen infusion into the coatings. There was a slight difference in pore diameter, with AA7075-T6 exhibiting a larger pore size comparative to the initiation voltage, however the same trend of increasing and decreasing pore diameter comparative to voltage holds true. Oxygen infusion into the anodic coating was present in both studies, regardless of the process, although there was a significant difference in the amount present after each process and this is strongly tied to the main nonaluminum alloy wt. % present in the coating. Processes with more steps during the ramps (7075 - R3, R4), (2024 - MS1, MS2), had significantly less zinc (7075) and copper (2024), which ultimately reduced the amount of oxygen in the coating.

Characterization testing results regarding corrosion resistance and abrasion resistance were performed on both alloys. Specimens from all processes in both studies passed the ASTM B117 specified test, which simulates a salt fog environment. Processes from the AA 7075 study performed slightly better, in which no panels exhibited multiple pits. Increased abrasion resistance is correlated with lower final voltage in both studies. However, films produced on AA2024-T3 lost significantly more material than coatings on AA7075. On average films produced by AA2024 lost 87.7 % more weight than films produced by AA7075. The margin is even larger on stepped

processes, where the stepped processes from AA2024 processes lost 96.7% more weight than the AA7075.

Anodic efficiency and coating rates are the biggest differences between the two alloys. This is apparent in the voltage required to achieve a certain current density and the current density needed to achieve comparable film thickness. AA2024-T3 needed on average 28.3% more voltage to initiate the process when compared at the same current density used to process AA7075-T6. The average current density required to produce 1 micron of coating in 30 minutes was 38% more in AA2024 than in AA7075 with values of 14 A/m^2 and 9.5 A/m^2, respectively. Noticeably, the coatings formed on AA7075 form much faster and at lower voltages, 22.4%, than coatings formed on AA2024. The presence of copper is a major contributing factor to this. When copper is present on the surface or in the anodic oxide, it robs current from the reaction and produces large amounts of oxygen. Both phenomena reduce coating efficiency and require larger amounts of voltage to drive the reaction. Process R1 from the 7075-T6 study incurred similar coating rate reduction due to the presence of Zinc and other intermetallics. In AA2024 – T3, copper becomes involved on the surface of the coating, and in 7075 – T6, zinc is underneath at the interface, where zinc then dramatically reduces the primary oxidation reaction and increases resistance [11].

It would be recommended that applications needing higher wear resistance and thicker coatings for dielectric properties, use AA7075-T6. However, the mechanism of failure of AA7075-T6 (zinc piling at interface), poses issues of delamination and film crazing in the field, so applications that are subjected to thermal cycling may want to use AA2024-T3.

The work aimed at refining and developing new processes for anodizing difficult alloys is expected to continue on these alloys and on other wrought aluminum alloys. It has been shown that the alloys do have different electrochemical behaviors, and further attention must be given when processing. The focus on how to further manipulate the current density to get a desired application

should also be explored. It is expected to eventually have processes that are “designer processes” in which certain methods will be dedicated for hardness or wear resistance only.

APPENDIX A

ELECTROLYTE CONCENTRATION PROCEDURE

This Appendix outlines a procedure used to measure the concentration of the sulfuric acid electrolyte.

Reagents Required:
- 1.0 N Sodium Hydroxide
- Methyl Orange Indicator
- Phenolphthalein Indicator
- Deionized water

Equipment Required:
- 250 ml Erlenmeyer flask
- 5 ml pipette
- 50 ml pipette
- 50 ml burette
- Magnetic stirrer

Procedure:

Free Sulfuric Acid, Aluminum Analysis:

1. Pipette 5 ml of the solution into a 250 ml beaker and dilute with 50 ml distilled water.
2. Add two (2) drops methyl orange indicator
3. Titrate slowly with 1.0N NaOH to an orange endpoint.
4. Record mls 1.0N NaOH as "A"
5. Add eight (8) small drops phenolphthalein indicator
6. Continue titrating slowly with 1.0N NaOH to a pink endpoint
7. Record mls 1.0N NaOH as "B"

Calculation:

Sulfuric Acid concentration (g/l) = A x 9.8

Dissolved Aluminum (g/l) = (B – A) x 1.8

REFERENCES

[1] Sheasby, P.G., Pinner, R. The Surface Treatment and Finishing of Aluminum and Its Alloys. 6th Edition, Materials Park, Ohio, The American Society of Metals International, 2001.

[2] Mohammadi, I., Ahmadi, S., Afshar, A. Effect of pulse current parameters on the mechanical and corrosion properties of anodized nanoporous aluminum coatings. Mat. Chem. Phys. **2016** 183 490–498.

[3] Aluminum Alloys: Yield Strength and Tensile Strength. https://amesweb.info/Materials/Aluminum-Yield-Tensile-Strength.aspx. (Accessed on May 05, 2022)

[4] Ghali, E. Corrosion Resistance of Aluminum and Magnesium Alloys: Understanding, Performance, and Testing. Hoboken, New Jersey, John Wiley & Sons, 2010.

[5] Song-mei, L., Hong-rui, Z., Jian-hua, L. Corrosion behavior of aluminum alloy 2024-T3 by 8-hydroxy- quinoline and its derivative in 3.5% chloride solution. Trans. Nonferrous Met. **2007** 17(2) 318−325.

[6] Venugopal, A., Panda, R., Manwatkar, S., Sreekumar, K., Krishna, L.R., Sundararajan, G. Effect of micro arc oxidation treatment on localized corrosion behaviour of AA7075 aluminum alloy in 3.5% NaCl solution. Trans. Nonferrous Met. **2012** 22 700−710.

[7] Son, I.J., Nakano, H., Oue, S., Kobayashi. S., Fukushima, H., Horita, Z. Effect of equal-channel angular pressing on pitting corrosion resistance of anodized aluminum-copper alloy. Trans. Nonferrous Met. **2009** 19 904−908.

[8] García-Rubioa, M., Ocon, P., Climent-Font, A., Smith, R.W., Curioni, M., Thompson, G.E., Skeldon, P., Lavía, A., García, I. Influence of molybdate species on the tartaric acid/sulphuric acid anodic films grown on AA2024 T3 aero- space alloy, Corros. Sci. **2009** 51 2034-2042.

[9] Peng, Y. Magneto-optical characteristics of magnetic nanowire arrays in anodic aluminum oxide templates. Appl. Phys. Lett. **2003** 83 362-364.

[10] Belwalkar, A., Grasing, E., Van Geertruyden, W., Huang, Z., & Misiolek, W. Effect of processing parameters on pore structure and thickness of anodic aluminum oxide (AAO) tubular membranes. J. Mem. Sci. **2008** 319 192–198.

[11] Runge, J. The Metallurgy of Anodizing Aluminum. Gewerbestrasse, Switzerland. Springer International Publishing, 2018.

[12] Kavas, B. Mechanical properties and frictional behavior of nanoporous anodic aluminum oxide (published doctoral thesis). **2011** Istanbul Technical University, Istanbul, Turkey.

[13] Kniep, R., Lamparter, P., Steeb, S. Structure of anodic oxide coatings on aluminum. Adv. Mater. **1989** 1 229-231.

[14] Runge, J.M. Formation of porous anodic oxide finishes – A new approach and theory. Proceedings Aluminium **2000.**

[15] Zhang, F., Levine, L., Allen, A., Campbell, C., Creuziger, A., Kazantseva, N., Ilavsky, J. In situ structural characterization of ageing kinetics in aluminum alloy 2024 across angstrom-to-micrometer length scales. Acta Mater. **2016** 111 385–398.

[16] Wang, S., Starink, M. Precipitates and intermetallic phases in precipitation hardening Al-Cu-Mg-(Li) based alloys. Int. Mater. Rev. **2005** 50 193-215.

[17] Bononi, M., Giovanardi, R., Bozza, A., Mattioli, P. Pulsed current effect on hard anodizing process of 2024-T3 aluminium alloy. Surf. Coat. Technol. **2016** 289 110–117.

[18] Bozza, A., Giovanardi, R., Manfredini, T., Mattiolo, P. Pulsed current effect on hard anodizing process of 7075-T6 aluminum alloy. Surf. Coat. Technol. **2015** 270 139–813 144.

[19] Rometsch, P. A., Zhang, Y., Knight, S. Heat treatment of 7xxx series aluminum alloys—some recent developments. Trans. Nonferrous Met. **2014** 24 2003-2017.

[20] The American Society of Metals Handbook Volume 2: Properties and Selection: Nonferrous Alloys and Special- Purpose Materials. Novelty, Ohio, The American Society of Metals International, 1990.

[21] Dursun, T., Soutis, C. Recent developments in advanced aircraft aluminum alloys. Mater. Des. **2014** 56 862–871.

[22] Precipitation Hardening of Aluminum Alloys. https://www.totalmateria.com/page.aspx?ID=CheckArticle&site=ktn&NM=235. (Accessed May 05, 2022).

[23] Veys-Renaux, D., Chahboun, N., Rocca, E. Anodizing of multiphase aluminum alloys in sulfuric acid: in-situ electrochemical behavior and oxide properties. Electrochim. Acta. **2016** 211 1056-1065.

[24] Liao, C.M., Wei, R.P. Galvanic coupling of model alloys to aluminum – a foundation for understanding particle-induced pitting in aluminum alloys. Electrochim. Acta **1999** 45 881-888.

[25] Alloy 2024 Sheet and Plate. http://www.howardprecision.com/wp-content/uploads/2017/08/alloy2024techsheet1.pdf. (Accessed on May 05, 2022).

[26] Yu, L., Jata, K. V. Review and study of physics driven pitting corrosion modeling in 2024-T3 aluminum alloys. **2015** 9437 94372E–94372E–8.

[27] Schneider, O., Ilevbare, G.O., Scully, J.R. In situ confocal laser scanning microscopy of AA 2024-T3 corrosion metrology I. Localized corrosion of particles. J. Electrochem. Soc. **2004** 151 B465.

[28] Wei, R. P., Liao, C.-M., Gao, M. A transmission electron microscopy study of constituent-particle-induced corrosion in 7075-T6 and 2024-T3 aluminum alloys. Metall. Mater. Trans. A. **1998** 29 1153–1160.

[29] Lecture 21: Types of Interfaces: coherent, semi-coherent, and incoherent. https://my.eng.utah.edu/~lzang/images/lecture-21.pdf. (Accessed on May 05, 2022).

[30] Umamheshwer Rao, A.C., Vasu, V., Govindaraju, K., Sai Srinadh, K.V. Stress corrosion cracking behavior of 7xxx alloys: A literature review. Trans. Nonferrous Met. **2016** 26 1447-1471.

[31] S.J. Ployhar, et al., ITER components cooling: Satisfying the distinct needs of systems and components, Fusion Eng. Des. **2014**

[32] Huang, Y.-S., Shih, T.-S., Chou, J.-H. Electrochemical behavior of anodized AA7075-T73 alloys as affected by the matrix structure. Appl. Surf. Sci. **2013** 283 249–257.

[33] Shahzad, M., Chaussumier, M., Chieragatti, R., Mabru, C., Rezai-Aria, F. Surface characterization and influence of anodizing process on fatigue life of Al 7050 alloy. Mater. Des. **2011** 32 3328–3335.

[34] Dostal, P., Kumbar, V., Cerny, M., Sabaliauskas, A. Accelerated corrosion and fatigue monitoring of aluminum alloy EN AW 7075. Technologjos Mokslai, **2015** 112-118.

[35] Hihara, L.H., Latanision, R.M. Corrosion of metal matrix composites. Int. Mater. Rev. **1994** 39 245-264.

[36] Birbilis, N., Buchheit, R.G. Characteristics of intermetallic phases in aluminum alloys an experimental survey and discussion. J. Electrochem. Soc. **2005** 152 B140-B151.

[37] Buchheit, R.G., Montes, L.P., Martinez, M.A., Michael J., Hlava, P.F. The electrochemical characteristics of bulk synthesized Al_2CuMg. J. Electrochem. Soc. **1999** 146 4424-4428.

[38] Chen, G.S., Gao, M., Wei, R.P. Microconstituent-induced pitting corrosion in aluminum alloy 2024-T3. Corrosion. **1996** 52 8-15.

[39] Scully, J.R., Knight, T.O., Buchheit, R.G., Peebles, D.E. Electrochemical characteristics of the Al2Cu, Al3Ta and Al3Zr intermetallic phases and their relevancy to the localized corrosion of Al alloys. Corros. Sci. **1993** 35 185–195.

[40] Ilevbare, G.O., Schneider, O., Kelly, R.G., Scully, J.R. In situ confocal laser scanning microscopy of AA 2024-T3 corrosion metrology. J. Electrochem. Soc. **2004** 151 B453.

[41] Scully, J.R., Peebles, D.E., Romig, A.D., Frear, D.R., Hills, C.R. Metallurgical factors influencing the corrosion of aluminum, Al-Cu, and Al-Si alloy thin films in dilute hydrofluoric solution. Metall. Trans. A. **1990** 23 1365.

[42] De Miera, M.S., Curioni, M., Skeldon, P., Thompson, G.E. Modelling the anodizing behavior of aluminum alloys in sulfuric acid through alloy analogues. Corros. Sci. **2008** 50 3410–3415.

[43] Buchheit, R.G., Grant, R.P., Hlava, P.F., Mckenzie B., Zender, G.L. Local dissolution phenomena associated with s phase (Al_2CuMg) particles in aluminum alloy 2024-T3. J. Electrochem. Soc. **1997** 144 2621-2628.

[44] Szklarska-Smialowska, Z. Pitting corrosion of aluminum. Corros. Sci. **1999** 41 1743–1767.

[45] Guillaumin, V., Mankowski, G. Localized corrosion of 2024 T351 aluminum alloy in chloride media. Corros. Sci. **1998** 41 421–438.

[46] Donatus, U., Thompson, G.E. Corrosion pathways in aluminum alloys. Trans. Nonferrous Met. **2017** 27 55-62.

[47] Vargel, C. Corrosion of Aluminum. Amsterdam, Netherlands, Elsevier, 2004.

[48] Girisha, H.N., Sharma, K.V. Effect of magnesium on strength and microstructure of aluminum, copper, magnesium alloys. Inter. J. Sci. Eng. Res. **2012** 3 2.

[49] Nafsin, N., Rashed, H.M.M.A. Effects of copper and magnesium on microstructure and hardness of Al-Cu-Mg alloys. Inter. J. Sci. Adv. Techno. **2013** 2.

[50] Son, K.A., Missert, N., Barbour, J.C. Growth and oxidation of thin film Al_2Cu. J. Electrochem. Soc. **2001** 148 B260-B263.

[51] Singh Verma, A., Sumankant, N. Mohan Suri, Y. Corrosion behavior of aluminum base particulate metal matrix composites: a review. Mater. Today Proc. **2015** 2 2840-2851.

[52] Belov, N. A., Avksent'eva, N. N. Quantitative analysis of the Al-Cu-Mg-Mn-Si phase diagram as applied to commercial aluminum alloys of series 2xxx. Metal Sci. Heat Treat. **2013** 55 358-363.

[53] Shabestari, S., Ghoncheh, M., Momeni, H. Evaluation of formation of intermetallic compounds in Al2024 alloy using thermal analysis technique. Thermochim. Acta **2014** 589 174-182.

[54] Saenz de Miera, M., Curioni, M., Skeldon, P., Thompson, G.E. Preferential anodic oxidation of second-phase constituents during anodizing of AA2024-T3 and AA7075-T6 alloys. Surf. Interface Anal. **2010** 42 241–246.

[55] Kaufman., J.G. Corrosion of Aluminum and Aluminum Alloys. Materials Park, Ohio, The American Society of Metals International, 2005.

[56] Runge, J.M., Hossain, T. Interfacial phenomena in 7000 series alloys and their impact on the anodic oxide. Mater. Today Proc. **2015** 2 10 5055–5062.

[57] Martinez-Viademonte, M., Abrahami, S.T., Hack, T., Burchardt, M., Terryn, H. A review on anodizing of aerospace aluminum alloys for corrosion protection. Coat. **2020** 10 1–.

[58] Shannon, R.D. Revised effective ionic radii and systematic studies of interatomic distances in halides and chalcogenides. Acta Cryst **1976** A32 751–767.

[59] Iglesias-Rubianes, L., Garcia-Vergara, S.J, Skeldon, P., Thompson, G.E., Ferguson, J., Beneke, M. Cyclic oxidation process during anodizing of Al–Cu alloys. Electrochim. Acta. **2007** 52 7148–7157.

[60] Zhou, X., Thompson, G.E., Habazaki, H., Shimizu, K., Skeldon, P., Wood, G.C. Copper enrichment in Al–Cu alloys due to electropolishing and anodic oxidation. Thin Solid Films. **1997** 293 327–332.

[61] Pakes, A., Thompson, G.E., Skeldon, P., Morgan, P.C. Development of porous anodic films on 2014-T4 aluminium alloy in tetraborate electrolyte. Corros. Sci. **2003** 45 1275–1287.

[62] Curioni, M. Saenz de Miera, M. Skeldon, P. Thompson, G.E. Ferguson, J. Macroscopic and local filming behavior of AA2024 T3 aluminum alloy during anodizing in sulfuric acid electrolyte. J. Electrochem. Soc. **2008** 155 C387–C395

[63] Brace, A.W. The Technology of Anodizing Aluminum. Modena, Italy, Interall S.r.l. 2000.

[64] Davis, J.R. Introduction to Aluminum and Aluminum Alloys. Materials Park, Ohio, The American Society of Metals International, 1998.

[65] ASM Handbook Committee. Properties of Wrought Aluminum and Aluminum Alloys. Materials Park, Ohio, The American Society of Metals International, 1990.

[66] Approved Process Sources. http://active.boeing.com/doingbiz/d14426/index.cfm (Accessed on May 05, 2022).

[67] Kallenborn, K J, Emmons, J R. Thin-film sulfuric acid anodizing as a replacement for chromic acid anodizing. United States.

[68] Cotell, C.M., Sprague, J.A., Smidt Jr., F.A. The American Society of Metals Handbook, Volume 5: Surface Engineering. Materials Park, Ohio, The American Society of Metals International, 1994.

[69] O'Sullivan, J.P., Wood, G.C. The morphology and mechanism of formation of porous anodic films on aluminum. Proc. R. Soc. Lond. B Biol. Sci. Math. Phys. Sci. **1970** 317 511–543.

[70] Guezmil, M., Bensalah, W., Khalladi, A., Elleuch, K., Depetris-Wery, M., Ayedi, H. Friction coefficient and microhardness of anodized aluminum alloys under different elaboration conditions. Trans. Nonferrous Met. **2015** *25* 6 1950–1960.

[71] Ning-ning, H., Shi-rong, G., Liang, F. Tribological properties of nano-porous anodic aluminium oxide template. Journal of Central South University of Technology. **2011** 18 1004−1008.

[72] Basics of Aerospace Materials: Aluminum and Composites. https://www.machinedesign.com/materials/basics-aerospace-materials-aluminum-and-composites. (Access May 05, 2022).

[73] Davis, J.R. Alloying: Understanding the basics. Materials Park, Ohio, The American Society of Metals International, 2001.

[74] Mohseni, E., Zalnezhad, E., Sarhan, A. A. D., Bushroa, A. R. A Study on surface modification of Al7075-T6 alloy against fretting fatigue phenomenon. Adv Mater Sci Eng. **2014** 1–17.

[75] Chung, C.K., Chang, W.T., Liao, M.W., Chang, H.C. Effect of pulse voltage and aluminum purity on the characteristics of anodic aluminum oxide using hybrid pulse anodization at room temperature. Thin Solid Films. **2011** 519 15 4754-4758.

[76] Cooke, W.E. Factors affecting loss of brightness and image clarity during anodizing of bright trim aluminum alloys in sulfuric acid electrolyte. Plating **1962** 49 1157–1165.

[77] Roshani, M., Sabour Rouhaghdam, A., Aliofkhazraei, M., Heydari Astaraee, A. Optimization of mechanical properties for pulsed anodizing of aluminum. Surf. Coat. Technol. **2017** 310 17–.

[78] Zhu, X.F., Li, D.D., Song, Y., Xiao, Y.H. The study of oxygen bubbles of anodic alumina based on high purity aluminum. Mater. Lett. **2005** 59 3160–3163.

[79] Habazaki, H., Konno, H., Shimizu, K., Nagata, S., Skeldon, P., Thompson, G.E. Incorporation of transition metal ions and oxygen generation during anodizing of aluminium alloys. Corros. Sci. **2004** 46 2041–2053.

[80] Schaedel, F. The leading-edge guide to top quality anodizing using the complete spectrum approach with a universal type I-II-III (123) mixed electrolyte. Prod. Finish. **2012** 76 9 1-13.

[81] Michaf, P., Vagaskâ, A., Gombâr, M., Hošovský A., Kmec, J.Monitoring of influence of significant parameters during anodizing of aluminum, IEEE 12th International Symposium on Applied Machine Intelligence and Informatics (SAMI), Herl'any, (2014) 49-54.

[82] Chung, C.K., Liao, M.W., Chang, H.C., Lee, C.T. Effects of temperature and voltage mode on nanoporous anodic aluminum oxide films by one-step anodization. Thin Solid Films **2011** 520 5 1554–1558.

[83] Ding, Z. Mechanistic study of thin film sulfuric acid anodizing rate difference between Al2024 T3 and Al6061 T6. Surf. Coat. Tecnol. **2019** 357 280-288.

[84] Bouchama, L., Azzouz, N., Bukmouche, N., Chopart, J.P., Daltin, A.L., Bouznit, Y. Enhancing aluminum corrosion resistance by two-step anodizing process. Surf. Coat. Technol. **2013** 235.

[85] Fine, M.E. Precipitation hardening of aluminum alloys. Metall. Trans. A. **1975** 6 625–630.

[86] Diggle, J.W., Downie, T.C., Goulding, C.W. Anodic oxide films on aluminum. Chem. Rev. **1969** 69 3 365–405.

[87] Shih, H.H., Tzou, S.L. Study of anodic oxidation of aluminum in mixed acid using a pulsed current. Surf. Coat. Technol. **2000** 124 278–285.

[88] Zhao, X., Wei, G., Meng, X., Zhang, A. High performance alumina films prepared by direct current plus pulse anodization. Surf. Eng. **2014** 30 455–459.

[89] Fratila-Apachitei, L.E., Duszczyk, J., Katgerman, L. A1–Si–(Cu) anodic oxide layers formed in H2SO4 at low temperature using different current waveforms. Surf. Coat. Technol. **2003** 165 232–240.

[90] Wu, W., Yuan, J.S., Kang, S.H., Oates, A.S. Electromigration subjected to Joule heating under pulsed DC stress. Solid State Electron. **2001** 45 2051–2056.

[91] ImageJ, Image Processing and Analysis. https://imagej.nih.gov/ij/. (Accessed 30 May 2021).

[92] Walpole, R.E., Myers, R.H., Myers, S.L., Ye, K.E. Probability and Statistics for Engineers and Scientists. 9th Ed, London, UK, Pearson, 2022.

[93] Curioni, M., Skeldon, P., Thompson, G.E., Ferguson, J. Graded anodic film morphologies for sustainable exploitation of aluminum alloys. Adv. Mater. Res. **2008** 38 48–55.

[94] Zaidi, S., Butt, M., Bashir, F. A comparative study of the anodic alumina film thickness measured via SEM and evaluated using Faraday's Law. Mater. Res. Express **2019** 6 4 46404.

[95] Lee, W., Park, S. Porous anodic aluminum oxide: anodization and templated synthesis of functional nanostructures. Chem. **2014** 114 15 7487–7556,

[96] Suranarayana, C. M.G. Norton, X-ray Diffraction: A Practical Approach. New York, New York, Springer, 1998.

[97] Ostovan, F., Amanollah, S., Toozandehjani, M., Shafiei, E. Fabrication of Al5083 surface hybrid nanocomposite reinforced by CNTs and Al2O3 nanoparticles using friction stir processing. J. Compos. Mater **2020** 54 1107–1117.

[98] Ostovan, F., Azimifar, I., Toozandehjani, M., Shafiei, E., Shamshirsaz, M. Synthesis of ex-situ Al5083 reinforced with mechanically-alloyed CNTs and Fe2O3 nanoparticles using friction stir processing. J. Appl. Res. Technol. **2021** 14 1670–1681.

[99] Serdechnova M, Karpushenkov SA, Karpushenkava LS. The influence of PSA pre-anodization of AA2024 on PEO coating formation: composition, microstructure, corrosion, and wear behaviors. Materials **2018** 11 2428.

[100] Lu, J., Wei, G., Yu, Y., Guo, C., Jiang, L. Aluminum alloy AA2024 anodized from the mixed acid system with enhanced mechanical properties. Surf. Interface **2018** 13 46–50.

[101] Jani, A., Losic, D., Voelcker, N.H. Nanoporous anodic aluminum oxide: advances in surface engineering and emerging application. Prog. Mater. Sci **2018** 58 636–704.

[102] Meng, X.F., Wei, G., Zhao, X., Ge, H. Study on anodic oxidation of 2024 aluminum alloys in sulfuric-citric acid. Mater. Sci. Forum **2014** 788 236–242.

[103] Chen, Y., Gao, N., Sha, G., Ringer, S. P., Starink, M. J. Microstructural evolution, strengthening and thermal stability of an ultrafine-grained Al–Cu–Mg alloy. Acta Mater **2016** 109 202–212.

[104] Totaro, P., Khusid, B. Multistep anodization of 7075 – T6 aluminum alloy. Surf. Coat. Technol **2021** 421 127407.

[105] Vignoli, M., Dick, A., Knörnschild, P., Dick, L.F. The effect of different carboxylic acids on the sulfuric acid anodizing of AA2024. Surf. Coat. Technol **2020** 383 125283–.

[106] Elaish, R., Curioni, M., Gowers, K., Kasuga, A., Habazaki, H., Hashimoto, T., Skeldon, P. Effect of fluorozirconic acid on anodizing of aluminium and AA 2024-T3 alloy in sulphuric and tartaric-sulphuric acids. Surf. Coat. Technol **2018** 342 233-243.

[107] Schneider, M., Liebmann, T., Langklotz, U., Michaelis, A. Microelectrochemical investigation of anodic oxide formation on the aluminum alloy AA2024. Electrochim. Acta **2017** 249 198–205.

[108] Ma, S., Luo, P., Zhou, H., Fu, C., Kuang, Y. Preparation of anodic films on 2024 aluminum alloy in boric acid-containing mixed electrolyte. Trans. Nonferrous Met **2008** 18 825–830.

[109] Li, Y., Zhang, Y., Li, S., Zhao, P. Influence of adipic acid on anodic film formation and corrosion resistance of 2024 aluminum alloy. Trans. Nonferrous Met **2016** 26 492–500.

[110] Elabar, D., La Monica, G., Santamaria, M., Di Quarto, F., Skeldon, P., Thompson, G. Anodizing of aluminium and AA 2024-T3 alloy in chromic acid: Effects of sulphate on film growth. Surf. Coat. Technol **2017** 309 480–489.

[111] Liu, S., Thompson G.E., Skeldon, P. Vanadate post-treatments of anodised aluminium and AA 2024 T3 alloy for corrosion protection. Trans. IMF **2018** 96 137-144,

[112] Choi, Y.C., Hyeon, J.Y., Bu, S.D., Bae, T.S. Effects of anodizing voltages and corresponding current densities on self-ordering process of nanopores in porous anodic aluminas anodized in oxalic and sulfuric acids. J. Korean Phys. Soc **2009** 55 835–840.

[113] Ono, S., Masuko, N. Evaluation of pore diameter of anodic porous films formed on Aluminum. Surf. Coat. Technol **2003** 169-170 139–142.

[114] Choudhary, R.K., Mishra, P., Kain, V., Singh, K., Kumar, S., Chakravartty, J. Scratch behavior of aluminum anodized in oxalic acid: effect of anodizing potential. Surf. Coat. Technol **2015** 283, 135–147.

[115] van Put, M.A., Abrahami, S.T., Elisseeva, O., de Kok, J.M.M., Mol, J.M.C., Terryn, H. Potentiodynamic anodizing of aluminum alloys in Cr (VI)-free electrolytes. Surf. Interface Anal **2016** 48 946–952.

[116] Torrescano-Alvarez, J., Curioni, M., Zhou, X., Skeldon, P. Effect of anodizing conditions on the cell morphology of anodic films on AA2024-T3 alloy. Surf. Interface Anal **2019** 51 12 1135–1143.

[117] Habazaki, H., Shimizu, K., Skeldon, P., Thompson, G., Wood, G., Zhou, X. Effects of alloying elements in anodizing of aluminum. Trans. Inst Met. Finish **1997** 75 1 18-23.

[118] ASTM Committee B08 on Metallic and Inorganic Coatings. “Standard Test Method for Seal Quality of Anodic Coatings on Aluminum by Acid Dissolution,” ASTM B680-80. In Annual Book of ASTM Standards, vol. 02.05. ASTM International, West Conshohocken, Pa, USA, 2019. Available online: https://doi.org/10.1520/B0680-80R14. (Accessed on 30 April 2022).

[119] ASTM Committee G01 on Corrosion of Metals. “Standard Test Method for Operating Salt Spray (Fog) Apparatus,” ASTM B117- 19. In Annual Book of ASTM Standards, vol. 03.02. ASTM International, West Conshohocken, PA, USA, 2019. Available online: https://www.astm.org/g0085-19.html (Accessed on 30 April 2022).

[120] Voevodin, N.N., Balbyshev, V., Donley, M. Investigation of corrosion protection performance of sol–gel coatings on AA2024-T3. Prog. Org. Coat. **2005** 52 28–33.

[121] García-Rubio, P., Curioni, M., Thompson, G., Skeldon, P., Lavía, A., García, I. Degradation of the corrosion resistance of anodic oxide films through immersion in the anodising electrolyte. Corros. Sci **2010** 52 2219–2227.

[122] Priet, B., Odemer, G., Blanc, C., Giffard, K., Arurault, L. Effect of new sealing treatments on corrosion fatigue lifetime of anodized 2024 aluminium alloy. Surf. Coat. Technol. **2016** 307 206–219.

[123] López, V., González, J.A., Otero, E., Escudero, E., Morcillo, M. Atmospheric corrosion of bare and anodised aluminium in a wide range of environmental conditions. Part II: electrochemical responses. Surf. Coat. Technol **2002** 153 235–244.

[124] Hitzig, J., Jüttner, K., Lorenz, W.J., Paatsch, W. AC-impedance measurements on porous aluminium oxide films. Corros. Sci. **1984** 24 945–952.

[125] Hitzig, J., Jüttner, K., Lorenz, W.J., Paatsch, W. AC-impedance measurements on Corroded porous aluminum oxide films. J. Electrochem. Soc **1986** 133 887,

[126] González, J.A., López, V., Bautista, A., Otero, E., Nóvoa, X.R. Characterization of porous aluminium oxide films from a.c. impedance measurements. J. Appl. Electrochem. **1992** 29 229–238.

[127] Boisier, G., Pébère, N., Druez, C., Villatte, M., Suel, S. FESEM and EIS study of sealed AA2024 T3 anodized in sulfuric acid electrolytes: influence of tartaric acid. J. Electrochem. Soc. **2008** 155 C521.

[128] Boisier, G., Lamure, A., Pébère, N., Portail, N., Villatte, M. Corrosion protection of AA2024 sealed anodic layers using the hydrophobic properties of carboxylic acids. Surf. Coat. Technol **2009** 203 3420–3426.

[129] Goldstein, J.I. Newbury, D.E., Michael, J.R., Ritchie, N.W.M., Scott, J.H.J., Joy, D.C. Scanning Electron Microscopy and X-Ray Microanalysis. New York, New York, Springer, 2018.

[130] ImageJ, Image Processing and Analysis. https://imagej.nih.gov/ij/. (Accessed 15 March 2022).

[131] Keller, F., Hunter, M.S., Robinson, D.L. Structural features of oxide coatings on aluminum. J. Electrochem. Soc **1953** 100 411 – 419.

[132] National Institute of Standards & Technology Certificate of Analysis Standard Reference Material® 1976c Instrument Response Standard for X-Ray Powder Diffraction. https://www-s.nist.gov/srmors/certificates/1976c.pdf (Accessed on May 05, 2022).

[133] Usman, B.J., Scenini, F., Curioni, M. The effect of exposure conditions on performance evaluation of post-treated anodic oxides on an aerospace aluminium alloy: comparison between salt spray and immersion testing. Surf. Coat. Technol **2020** 399 126157.

[134] Newbury, D., Ritchie, N.W. Electron-excited x-ray microanalysis by energy dispersive spectrometry at 50: analytical accuracy, precision, trace sensitivity, and quantitative compositional mapping. Microsc. and Microanal **2019** 25 5 1075–1105.